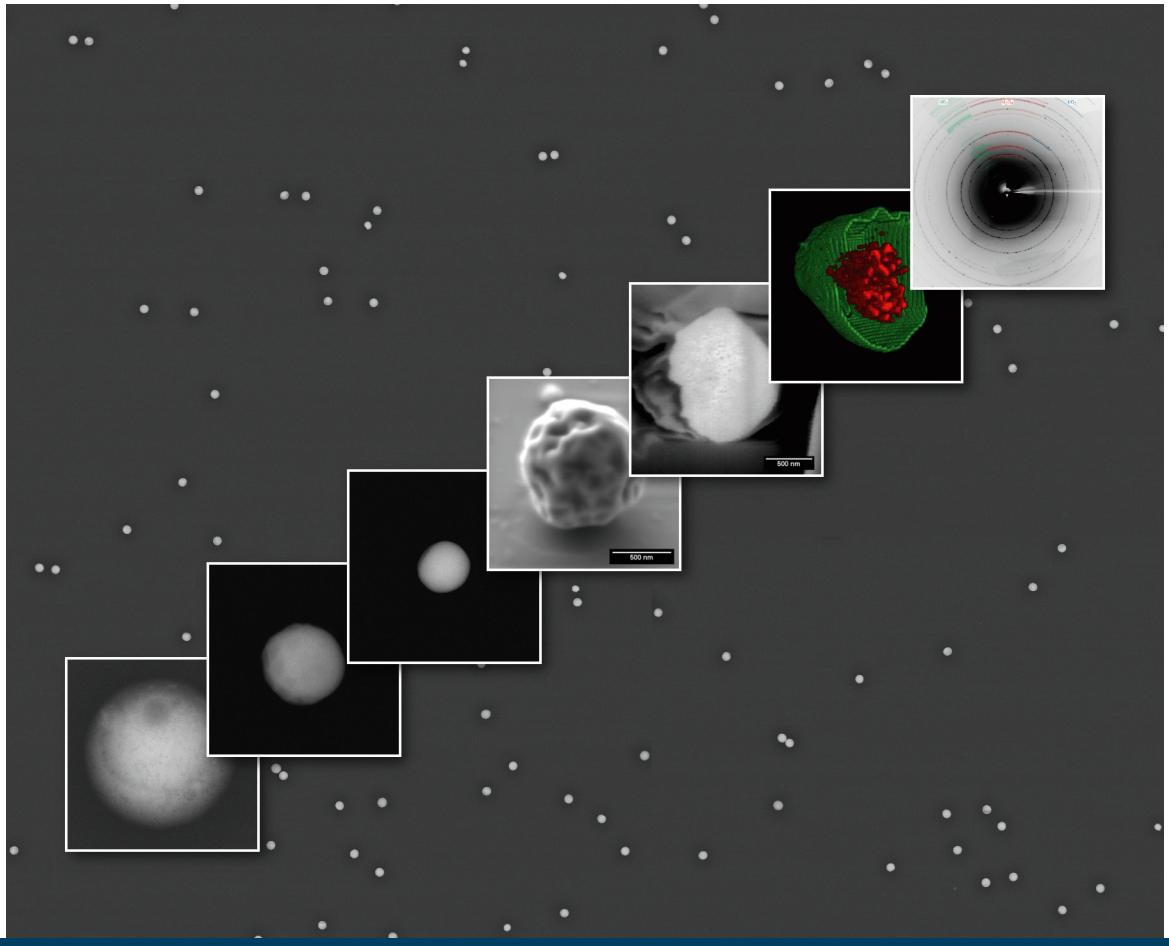

Synthesis and Stability Assessment of Uranium Microparticles: Providing Reference Materials for Nuclear Verification Purposes

Ronald Middendorp

Energie & Umwelt / Energy & Environment
Band / Volume 424
ISBN 978-3-95806-330-3

Mitglied der Helmholtz-Gemeinschaft

JÜLICH
Forschungszentrum

Schriften des Forschungszentrums Jülich
Reihe Energie & Umwelt / Energy & Environment Band / Volume 424

Forschungszentrum Jülich GmbH
Institute of Energy and Climate Research
Nuclear Waste Management and Reactor Safety (IEK-6)

Synthesis and Stability Assessment of Uranium Microparticles: Providing Reference Materials for Nuclear Verification Purposes

Ronald Middendorp

Schriften des Forschungszentrums Jülich
Reihe Energie & Umwelt / Energy & Environment Band / Volume 424

ISSN 1866-1793 ISBN 978-3-95806-330-3

Bibliografische Information der Deutschen Nationalbibliothek.
Die Deutsche Nationalbibliothek verzeichnet diese Publikation in der
Deutschen Nationalbibliografie; detaillierte Bibliografische Daten
sind im Internet über http://dnb.d-nb.de abrufbar.

Herausgeber und Vertrieb:	Forschungszentrum Jülich GmbH Zentralbibliothek, Verlag 52425 Jülich Tel.: +49 2461 61-5368 Fax: +49 2461 61-6103 zb-publikation@fz-juelich.de www.fz-juelich.de/zb
Umschlaggestaltung:	Grafische Medien, Forschungszentrum Jülich GmbH
Druck:	Grafische Medien, Forschungszentrum Jülich GmbH
Copyright:	Forschungszentrum Jülich 2018

Schriften des Forschungszentrums Jülich
Reihe Energie & Umwelt / Energy & Environment, Band / Volume 424

D 82 (Diss., RWTH Aachen University, 2018)

ISSN 1866-1793
ISBN 978-3-95806-330-3

Vollständig frei verfügbar über das Publikationsportal des Forschungszentrums Jülich (JuSER)
unter www.fz-juelich.de/zb/openaccess.

Abstract

To verify the commitment of States signatory to the Treaty on the Non-Proliferation of Nuclear Weapons (NPT), the International Atomic Energy Agency (IAEA) conducts inspections in nuclear facilities. During such inspections, environmental swipe samples are collected to verify the absence of undeclared activities. The collected samples are shipped to dedicated laboratories in the IAEA Network of Analytical Laboratories (NWAL), where individual microparticles containing fissile material collected on such swipe samples are investigated with high accuracy to determine the isotopic composition.

Due to the improved capabilities to detect and analyze individual microparticles, especially since the introduction of large-geometry secondary ion mass spectrometers (LG-SIMS), there is a great need for dedicated particulate samples which can be used for various quality control purposes. Within this work, a method was established to produce micrometer-sized particles with a monodisperse particle size distribution. The particles consist of a known amount of uranium oxide with a known uranium isotopic composition, and are intended to be certified as certified reference material (CRM).

In order to produce such microparticles, a spray-pyrolysis synthesis method based on the generation of a monodisperse aerosol using a vibrating orifice aerosol generator (VOAG) was used. The method is based on the generation of an aerosol from a solution with a known uranium isotopic composition, after which the generated droplets are heated. During heating, the solvent evaporates leading to the precipitation of the dissolved uranium into spherical shaped particles. The precipitated particles are thermally decomposed leading to the formation of uranium oxide particles.

To investigate the particle formation and subsequent thermal decomposition, aerosols were produced from uranyl chloride, uranyl acetate and uranyl nitrate precursor solutions. The generated droplets from the different precursors were heated up to 600 °C, after which the produced particles were investigated by combined scanning electron microscopy (SEM) and energy dispersive X-ray spectroscopic (EDX) studies, which provided insight into the particle formation process. Particles produced from uranyl chloride provided detailed information on the various particle formation and decomposition stages, although the final particles had highly irregular particle shapes and clear voids were observed. Particles produced from both uranyl acetate and uranyl nitrate resulted in spherical shapes with monodisperse particle size distributions, although the morphology of the produced particles was found to be strongly influenced by various factors during particle formation, such as the temperature and anion to cation ratio of the precursor solution.

To characterize the produced particles, the obtained particles were investigated by μ-X-ray diffraction (μ-XRD), μ-X-ray Absorption Near Edge Structure (μ-XANES), and μ-Raman spectroscopy. Particles produced from uranyl acetate were shown to consist of the orthorhombic triuranium octoxide (U_3O_8) phase, as was expected based on literature data of milligram ("bulk") amounts of material. Particles produced from uranyl nitrate, which were expected to consist of uranium trioxide were, however, also found to consist of triuranium octoxide, even after thermal treatment at 400 °C. The lower temperature at which the phase transformation from uranium trioxide into triuranium octoxide occurred is likely

caused by the very low amount of material and relative high surface area. Particles produced from uranyl nitrate, uranyl acetate and uranyl chloride were investigated by μ-Raman spectroscopy, were all investigated particles resulted in comparable spectra, indicating all particles consist of the same chemical phase.

Particles consisting of a mixture of uranium and cerium were produced and characterized, as a first step towards the production of mixed uranium/thorium and uranium/plutonium microparticles. Both μ-XRD and μ-Raman studies showed that a phase transformation occurs, leading to the formation of a cubic phase, which hints towards the formation of a uranium/cerium solid solution. The solid solution would lead to highly homogeneous particles and demonstrates the suitability of the method to produce composite particles.

To make the produced particles practically usable as source material for the preparation of a reference material, the transfer of produced particles into particle suspensions offers various advantages. To assess the stability of the produced microparticles within such suspensions, the particles were stored in ethanol where no visual alteration of the particle morphology was observed in electron microscopy studies during a timeframe of 432 days. Quantitative studies also did not reveal any significant dissolution after 228 days. Although no uranium isotopic exchange was measured between particles stored in ethanol, studies using milligram amounts of material showed that the uranium isotope exchange between solid triuranium octoxide and uranium-saturated water occurs via the formation of a uranyl hydroxide surface layer. The exchange reaction was found to follow first-order kinetics with a reaction rate of $142(24)\,\mathrm{nmol\,g^{-1}\,m^{-2}\,h^{-1}}$ and an activation energy of $34.7(29)\,\mathrm{kJ\,mol^{-1}}$ was determined. Similar studies performed in ethanol did not show any isotope exchange, which confirmed that the uranium isotopic composition of the produced microparticles remain stable while stored in ethanol, for up to a few hundred days.

The application of particles produced with the established setup as a source material to produce particle reference materials was demonstrated for several sets of samples. The uranium isotopic composition of the produced particles was measured by LG-SIMS, which showed that no alteration of the isotopic composition occurred during production and the particles are suitable to be used for regular quality control measurements. A large number of particle samples were prepared which are intended to be certified as CRM in accordance to ISO 17034:2016 and to be used for an interlaboratory comparison exercise.

Zusammenfassung

Zur Verifikation der Verpflichtungen der Unterzeichnerstaaten des Kernwaffen-Sperrvertrags führt die Internationale Atom-Energie Organisation (IAEO) in kerntechnischen Anlagen Inspektionen durch. Im Zuge dieser Inspektionen werden Umwelt-Wischproben gesammelt, welche Indikationen auf undeklarierte, geheime Aktivitäten liefern. Die gesammelten Proben werden an akkreditierte Laboratorien des Labornetzwerks der IAEO (Network of Analytical Laboratories) geliefert, in denen einzelne Spaltstoffhaltige Mikropartikel, welche auf Wischproben gesammelt wurden, mit hoher Genauigkeit untersucht werden, um die Isotopenzusammensetzung zu bestimmen.

Aufgrund der verbesserten Einsatzmöglichkeiten, einzelne Mikropartikel zu detektieren und zu analysieren, vor allem seit Einführung des „Large-Geometry“ Sekundär-Ionen Massenspektrometers (LG-SIMS), gibt es einen hohen Bedarf an maßgeschneiderten Partikel-Referenzproben welche für verschiedene Maßnahmen der Qualitätsüberwachung benötigt werden. Im Rahmen dieser Arbeit wurde eine Methode etabliert, mikrometergroße monodisperse Partikel herzustellen. Die Partikel bestehen aus einer vorher bestimmbaren Menge an Uranoxid und einer vorbestimmten Isotopenzusammensetzung und sind als Ausgangsmaterial für ein zertifiziertes Referenzmaterial vorgesehen (ZRM).

Um diese Mikropartikel herzustellen wurde die Methode der Spray-Pyrolyse eines monodispersen Aerosols verwendet. Hierbei wurde zur Herstellung des Aerosols ein vibrierender Schwingblenden-Aerosolgenerator verwendet, wobei diese Methode darauf beruht, dass eine uranhaltige Ausgangslösung mit bekannter Isotopenzusammensetzung der Uranisotope verwendet wird. Das Aerosol unterliegt einer thermischen Behandlung, im Zuge derer das Lösungsmittel verdampft, was zur Ausfällung des aufgelösten Urans und zur Bildung sphärischer Partikel führt. Weiter werden die Partikel durch die thermische Behandlung in ein Uranoxid Partikel umgewandelt.

Um ein eingehenderes Verständnis der Partikelformation und der nachfolgenden thermischen Umwandlung zu erlangen, wurden drei Synthesewege mittels Uranylchlorid-, Uranylacetat- und Uranylnitrat-Lösungen untersucht. Die generierten Aerosol-Tröpfchen wurden bei verschiedenen Temperaturen bis maximal 600 °C behandelt und die hieraus hergestellten Partikel mittels Raster-Elektronenmikroskopie (REM) und energie-dispersiver Röntgenspektrometrie (EDS) untersucht. Hieraus ergeben sich Einblicke in den Partikel-Bildungsprozess. Für die aus Uranylchlorid hergestellten Partikel ließen sich detaillierte Informationen über die verschiedene Partikelformations- und Umwandlungsvorgänge gewinnen, wenngleich die endgültigen Partikel unregelmäßig geformt und teilweise hohl waren. Partikel, die aus Uranylacetat und Uranylnitrat hergestellt wurden, wiesen eine sphärische Form mit einer monodispersen Größenverteilung auf. Hierbei zeigte es sich doch, dass die Partikelmorphologie stark von verschiedenen Faktoren, wie der Temperatur der thermischen Behandlung und dem Anion/Kation Verhältnis in der Ausgangslösung, beeinflusst wurde.

Zur weiteren Charakterisierung der hergestellten Partikel wurden diese mittels eines an einem Synchrotron erzeugten Mikrofokus-Röntgenstrahls per Röntgenbeugung (μ-XRD) und Röntgen-Nahkanten-Absorptions-Spektroskopie (μ-XANES) bzw. mittels Raman-Spektroskopie untersucht. Es konnte somit

gezeigt werden, dass die aus Uranylacetat hergestellten Partikel aus einer orthorhombischen triuranoctoxid (U_3O_8) Phase bestehen. Dies steht in Übereinstimmung mit den experimentellen Daten in der Literatur, welche aus Untersuchungen von Milligramm Mengen an Material gewonnen wurden. Bei den aus Uranylnitrat hergestellten Partikeln, wurde ebenfalls eine U_3O_8 Struktur festgestellt, selbst bei Temperaturen von 400 °C. Dieses unerwartete Ergebnis deutet auf eine Phasenumwandlung von UO_3 zu U_3O_8 hin. Diese Phasenumwandlung findet im Vergleich zu den in der Literatur beschrieben thermische Behandlungen am Pulvern bei geringen Temperaturen statt. Dieser Effekt ist sehr wahrscheinlich auf die relativ große spezifische Oberfläche der Mikropartikeln zurück zu führen. Aus Uranylnitrat, Uranylacetat und Uranylchlorid erzeugte Partikel wurden mittels μ-Raman Spektroskopie untersucht, wobei sich in allen drei Fällen die Spektren stark ähneln, was darauf hinweist, dass sie aus derselben Phase bestehen.

Zusätzlich wurden aus einer Uran/Cer-Gemisch bestehende Partikel hergestellt und charakterisiert. Dies stellt einen ersten Schritt zur Produktion von Mikropartikeln dar, die aus einem Uran/Thorium oder einem Uran/Plutonium-Gemisch bestehen, welche als Referenzmaterial eingesetzt werden könnten. Sowohl μ-XRD als auch μ-Raman Untersuchungen zeigten, dass ein ein Phasenübergang unter Bildung einer kubischen Phase stattfindet, was auf die Ausbildung eines Uran/Cer Mischkristalls hinweist. Dies wäre gleichbedeutend mit einer hochgradig homogenen Verteilung der Elemente im Partikel. Somit konnte demonstriert werden, dass die Methode zur Herstellung kompositer Partikel geeignet ist.

Für die praktische Anwendbarkeit der produzierten Partikel zur Herstellung von Präparaten eines Referenzmaterials bietet der Transfer der Partikel in eine Suspension mehrere Vorteile. Um die Stabilität der Partikel in Suspensionen zu untersuchen, wurden diese in Ethanol gebracht, wobei selbst nach 432 Tagen mittels Elektronenmikroskopie keine sichtbare Veränderung der Partikelmorphologie gegenüber dem Ursprungszustand festgestellt werden konnte. In quantitativen Studien konnte über einen Zeitraum von 228 Tagen keine signifikante Auflösung der Partikel gemessen werden. Zudem wurde auch kein Isotopenaustaucheffekt zwischen Partikeln festgestellt, die in Ethanol gespeichert worden waren. Im Gegensatz dazu zeigten Studien, dass der Isotopenaustaucheffekt bei Experimenten mit Milligramm-Mengen von U_3O_8 in gesättigter wässriger Lösung höchstwahrscheinlich über die Bildung einer Uranylhydroxid-Oberflächenschicht stattfindet. Die Austauchreaktion folgt einer Reaktionskinetik erster Ordnung mit einer bestimmten Reaktionsrate von $142(24)\,\mathrm{nmol\,g^{-1}\,m^{-2}\,h^{-1}}$ und einer bestimmten Aktivierungsenergie von $34.70(29)\,\mathrm{kJ\,mol^{-1}}$. Ähnliche Studien mit Ethanol bestätigten die Abwesenheit einer Isotopenaustauschreaktion und folglich die Stabilität von Paritkeln in Ethanol über einen Zeitraum von bis zu einigen hundert Tagen.

Die Anwendbarkeit der Präparationsmethode mittels Suspensionen und Partikeln, welche mit der etablierten Produktionsmethode hergestellt wurden, wurde für verschiedene Präparatarten demonstriert. Zudem wurde die Isotopenzusammensetzung mit LG-SIMS gemessen, in der verifiziert werden konnte, dass sich diese im Lauf der Partikelproduktion und der Präparation nicht verändert. Somit wurden diese Verfahren als für die Herstellung von Referenzmaterialien als geeignet angesehen. Eine große Menge an Partikel-Präparaten wurde hergestellt welche in Kooperation mit einem nach ISO 17034:2016 akkreditierten Labor zertifiziert werden sollen und für einen Ringversuch zum Einsatz kommen sollen.

Acknowledgements

During the last few years I have received great help from numerous persons. Most of all, I would like to thank Martin Dürr for his daily help with the project and all the incredible ideas he offered.

Many of the measurements were performed with help or by others; from FZJ/IEK-6, I would like to express my gratitude to Martina Klinkenberg (SEM/EDX/FIB), Murat Güngör (SEM/EDX), Fabian Sadowski (Q-ICP-MS), Dimitri Schneider (Q-ICP-MS), Philip Kegler (XRD) and Jakob Dellen (XRD/Raman). Also, I would like to thank Giuseppe Modolo, Andreas Wilden, Christian Schreinemachers, Katrin Baginski and especially Ralf König for their assistance with the radiation protection. From FZJ/ZEA-3 I would like to thank Volker Nischwitz (SF-ICP-MS), Matthias Balski (SF-ICP-MS) and Uwe Breuer (ToF-SIMS).

From the Paul Scherrer Institute (Villigen, Switzerland), I would like to thank Dario Ferreira Sanchez, Vallerie Ann Samson and Daniel Grolimund for the μ-XAS and μ-XRD measurements performed at the microXAS beamline of the Swiss Light Source. I also would like to thank Fabien Pointurier from CEA/DAM/DIF (Arpajon, France) for offering me the opportunity to visit his institute and performing μ-Raman measurements.

From the IAEA, I would like to express my sincere gratitude to Thip Tanpraphan, Laure Sangély, Ernesto Chinea-Cano, Jane Poths and Stephan Vogt for the numerous LG-SIMS measurements. Although described only briefly, their measurements have been the driving force behind this project. From the JRC-Geel (formerly JRC-IRMM) I would like to thank Jan Truyens, Stephan Richter and Yetunde Aregbe for providing us with custom made and verified solutions which were used to produce particles and their support by starting the official CRM project.

I also want to express my gratitude to Prof. Bosbach for giving me the opportunity to work in his institute. In line, I would like to thank Irmgard Niemeyer for giving me the chance to work in the International Safeguards team. I also would like to thank the entire International Safeguards team and all its extended and previous members. I want to express my gratitude to Alexander Knott for providing me a setup to work with and for his help with the μ-XAS and μ-XRD measurements. I would also like to thank Stefan Neumeier for his help.

And last but certainty not least, I would like to thank my family, friends and everyone who has helped me arriving where I am today!

Contents

1 Introduction

Due to the dual-nature of fissile (e.g. uranium and plutonium) materials, the usage of such materials is strongly regulated by various international treaties. One of the most important treaties is the Treaty on the Non-Proliferation of Nuclear Weapons [1] (NPT), which was enacted in 1970 and has been ratified by 191 countries [2]. Member States to the NPT declare not to pursue to obtain nuclear weapons and only use nuclear technologies for peaceful and civil purposes. In order to verify the commitment of member States to the NPT, nuclear safeguards have been implemented:

> **Article III** 1. Each non-nuclear-weapon State Party to the Treaty undertakes to accept safeguards, [...] for the exclusive purpose of verification of the fulfilment of its obligations assumed under this Treaty with a view to preventing diversion of nuclear energy from peaceful uses to nuclear weapons or other nuclear explosive devices. [...] [1]

Within the NPT, the International Atomic Energy Agency (IAEA) was assigned the task to perform nuclear safeguards in the NPT member States. As part of the implemented verification measures, the IAEA conducts inspections in nuclear facilities, during which the declared activities are verified. During such inspections, samples are taken from the nuclear material inventory. The collected samples are shipped to dedicated analytical laboratories of the so-called Network of Analytical Laboratories (NWAL) of the IAEA, where the samples are analyzed to quantify the content of fissile isotopes [3, 4]. Comparison of the measurement results with the member States declarations, i.e. material balance evaluation, acts as a tool to verify the correctness of the declarations.

Such verification measurements do, however, not verify the absence of undeclared activities. To increase the detection capabilities of undeclared activities, 146 countries have signed the Additional Protocol [5] to the NPT, which provides the IAEA with additional tools to verify the compliance of member States with their obligations. One of the tools capable of detecting undeclared activities is the collection of environmental samples, commonly described as swipe-samples:

> **Location-specific environmental sampling** means the collection of environmental samples (e.g., air, water, vegetation, soil, smears) [...] assisting the Agency to draw conclusions about the absence of undeclared nuclear material or nuclear activities at the specified location. [5]

Collected swipe samples during inspections are shipped to members of the IAEA NWAL dedicated towards the analysis of swipe samples. The swipe samples can be analyzed in two manners to investigate traces of collected nuclear materials; the bulk and particle analysis methods [6, 7]. For the bulk analysis, all nuclear materials collected onto a swipe sample are dissolved and the dissolved material is analyzed using high accuracy mass spectrometric methods to measure the amount and isotopic composition of the nuclear materials. Any deviation of the obtained results from the declared activities may indicate an undeclared activity. During the particle analysis, individual micrometer-sized particles are analyzed using microanalytical techniques, such as fission track-thermal ionization mass spectrometry (FT-TIMS) [8, 9] and secondary ion mass spectrometry (SIMS). The detection of single particles with isotopic compositions deviating from the declared materials hints towards undeclared activities within the investigated facility and particle analysis has therefore a higher detection probability compared to the bulk analysis of swipe samples. The recent introduction of large geometry (LG-) SIMS allows the rapid analysis of the entire particle population and accurate analysis of the minor isotopes [4, 10].

Analysis of individual particles collected on swipe samples has proven to be a valuable tool to gather information on the presence and nature of activities involving nuclear materials. The suitability of the particle analysis has been demonstrated in various cases and situations, where the handling and processing of nuclear materials could be detected (see [11, 12]). A practical example of the application of environmental swipe samples to verify the commitment of member States to the NPT was recently demonstrated in the Islamic Republic of Iran. The Joint Comprehensive Plan of Action [13] (JCPOA), signed on July 2015, states that Iran, among other obligations, is permitted to enrich uranium only up to 3.67 %. To verify the commitment of Iran to the JCPOA, the IAEA collects and analyses environmental swipe samples in various nuclear facilities in Iran, the results of which are used to derive safeguards conclusions [14].

The possible consequences of the obtained results from swipe sample analysis requires strict quality control measures to ensure reliable results are obtained. As a particular difficulty in particle analysis applied in the context of verifying safeguards commitments, the method applied should be capable of detecting particles, which would arise from a "suspicious" activity, and distinguishing it from particles resulting from regular operation. The problem is aggravated by the usually high background from normal dust, which is collected on the swipe. The problem has been described as like finding the "needle in the haystack". To ensure that single particles can be detected effectively by any laboratory involved in the analysis of swipe samples, regular analysis of well-defined samples within a quality control (QC) program are of vital importance. Such QC measurements do not only include the regular analysis of stable samples, both within and between various laboratories, but also calibration and validation of the methods.

Each of these QC measurements require dedicated materials [15, 16]; generally materials with a high degree of stability and homogeneity towards one or more property values are required. Materials with a high degree of stability and homogeneity are classified as reference materials (RMs), as defined by the International Vocabulary of Metrology [17] (VIM, ISO/IEC Guide 99:2007):

> **Reference Material.** material, sufficiently homogeneous and stable with reference to specified properties, which has been established to be fit for its intended use in measurement or in examination of nominal properties. [17]

Especially for calibration, but also validation and interlaboratory comparison exercises, materials with a defined "true" value are required. Such certified reference materials (CRMs) are defined as:

> **Certified Reference Material.** reference material, accompanied by documentation issued by an authoritative body and providing one or more specified property values with associated uncertainties and traceabilities, using valid procedures. [17]

As stated by the VIM, a CRM is issued by an authoritative body, for which the International Organization for Standardization (ISO) has published a norm, the ISO 17034:2016 [18] which describes the requirements to certify such materials. Of the various requirements, the technical requirements related to the certification of one or more property values are described in detail in ISO Guide 35 [19]. This ISO guide states that certification of a property value not only requires an accurate quantification of the intended property value, but also requires expanded uncertainties and metrological traceabilities of these values. The expanded uncertainty of the property values should not only include the uncertainty due to characterization, but also due to inhomogeneity and instability of the material [20]. Therefore, candidate reference materials should be investigated with regard to the inhomogeneity and instability of the intended property values and, if possible, the homogeneity and stability should be improved.

Over recent years, various attempts were undertaken to produce micrometer-sized uranium particles with known isotopic compositions. Of the various attempts, the hydrolysis of uranium hexafluoride [21, 22] was found to be suitable for the production of particles with a highly polydisperse particle size distribution and was employed in two interlaboratory comparison exercises [23, 24]. Although the produced particles were well suited for such exercises, accredited laboratories involved in the analysis of uranium microparticles for nuclear safeguards have expressed the need for particle reference materials consisting of monodisperse uranium microparticles with a certified isotopic composition [4, 25–27]. Due to the wide range of analysis samples and different quality control measures, various different types of samples would be required, ranging from "clean" samples with a single population of particles deposited onto a glass-like carbon disk towards a well-known mixture of particles with different isotopic compositions and dust onto cotton-swipes.

Aim of this Work

This work aims towards the production of micrometer-sized uranium particles based on the spray-pyrolysis of uranium containing aerosol-droplets. It presents scientific research on the particle production process using different uranium compounds and discussed findings on the morphology and chemical structure of produced particles. These material properties are important parameters for the suitability of particles for application as a (certified) reference material. In particular, this is shown to be of relevance in solid-liquid interactions of uranium particles, which are suspended in a solution. Particles in suspensions are of special interest, since it is a key enabler in addressing various needs towards a particle reference material. Based on these scientific findings, the viability of concrete application scenarios for preparation of a particle reference material for safeguards is demonstrated. The project was divided into four parts:

Process Characterization. The first part of this work focuses on the production of monodisperse microparticles using a spray-pyrolysis process, where an aerosol is produced using a vibrating orifice aerosol generator. The particle formation process is investigated with respect to various parameters, such as chemical precursor compound and thermal treatment temperature to optimize the homogeneity of the particle properties, for example the particle size and density.

Structural Investigations. After investigation and optimization of the particle production process, the obtained particles are investigated in more detail with respect to the structural properties, which are of importance towards the stability of the particles. Different microanalytical methods are applied, such as μ-X-ray diffraction (μ-XRD), μ-X-ray absorption spectroscopy (μ-XAS) and μ-Raman spectroscopy.

Solid-Liquid Interactions. In order to improve the homogeneity, particles could be transferred into suspensions. During storage in such suspensions, the particle stability might, however, be degraded. Therefore, various studies are performed to investigate interaction of uranium microparticles in liquid media, for example the dissolution of particles and the exchange of uranium isotopes between different phases.

Application as Particle Reference Material. Finally, the suitability of the produced particles for the production of microparticle certified reference materials is investigated and particles are produced which are to be used for the production of a certified reference material. Also, further possibilities to handle and process the particles are investigated using particle suspensions and the suitability of the produced particles for nuclear forensics is investigated.

2 Scientific Background

This chapter provides a scientific background for the results obtained within this work. In section 2.1 an overview of the chemistry of uranium and the relevant compounds is given. Section 2.2 describes the production of microparticles by spray-pyrolysis and gives an overview of the state of the art methods to produce uranium and/or plutonium particles for microanalytical applications. Finally, section 2.3 provides a theoretical background on the microanalytical methods employed in this work.

2.1 Uranium

2.1.1 Nuclear Properties

Uranium is a primordial element with an atomic number of 92 and a (natural) atomic weight of $238.028\,91(3)\,\mathrm{g\,mol^{-1}}$ [28]. A large number of isotopes of uranium are known, of which six are commonly encountered: ^{232}U, ^{233}U, ^{234}U, ^{235}U, ^{236}U and ^{238}U. Of these isotopes, ^{238}U is the most abundant isotope found in nature with an abundance of approximately $99.2742(10)\,\%$ [29]. The isotope of most interest for nuclear energy production is, however, ^{235}U because of the high neutron induced fission cross-section [30] (Figure 2.1). Due to the high fission yield of ^{235}U, it can be used to produce sustainable nuclear fission chain reactions, as used for the generation of electricity, but can also be used to produce nuclear weapons of mass destruction.

Due to the low natural abundance of ^{235}U ($0.7204(6)\,\%$ [29]) in the isotopic composition of uranium, natural uranium is not suitable for the production of nuclear weapons and also seldomly used for the generation of electricity. To use uranium for such applications, the abundance of ^{235}U needs to be increased, a process which is called enrichment. The enrichment of uranium is a very complex procedure; the two most common methods are based on gaseous diffusion and centrifugation [30]. During gaseous diffusion, a gaseous uranium species is heated and passed through a membrane filter. Due to the slightly lower mass of ^{235}U compared to ^{238}U, ^{235}U atoms are likelier to pass the filter and are therefore enriched. The efficiency of gaseous diffusion is, however, very low and has a very high power consumption. Gaseous centrifugation is, compared to diffusion, much more efficient. A gaseous uranium species is introduced into a rapidly rotating centrifuge, where the heavier ^{238}U is forced outside more strongly compared to the lighter ^{235}U. Due to the higher efficiency, gaseous centrifugation has become the most commonly applied technique for the enrichment of uranium.

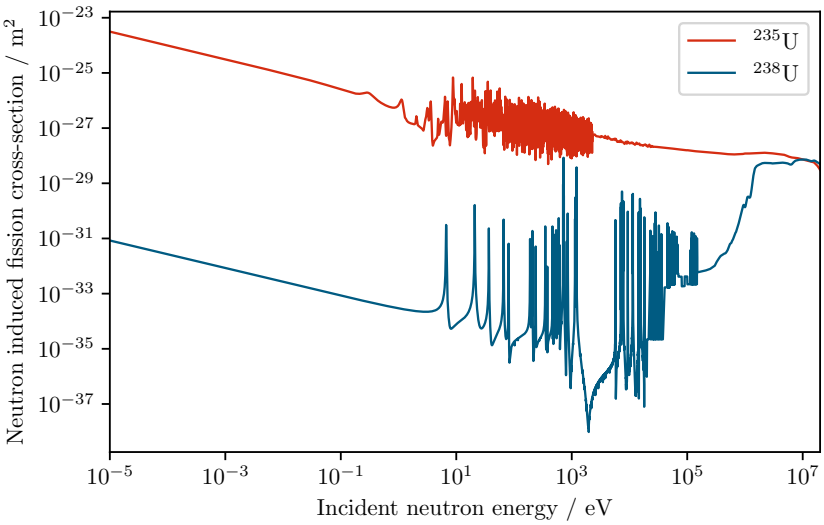

Figure 2.1: Neutron induced fission cross-section of ^{235}U and ^{238}U.

For the generation of electricity, uranium enriched to about 3 % to 5 % of ^{235}U is typically sufficient to efficiently create sustainable chain reactions. For nuclear weapons, however, a much higher enrichment is required; material with an enrichment above 20 % is considered to be suitable for the production of nuclear weapons. Therefore, for safeguards purposes uranium is commonly classified with regard to the enrichment as depleted uranium (DU), natural uranium (NU, U-nat or $^{\text{nat}}$U), low-enriched uranium (LEU), and high-enriched uranium (HEU), as described in Table I [31].

The ^{234}U isotope is a progeny in the decay-chain of ^{238}U and has a low abundance in natural uranium (0.0054(5) % [29]). However, due to the relative short half-life of ^{234}U (245.5 ka) compared to ^{235}U and ^{238}U, ^{234}U contributes for roughly 50 % of the specific activity of natural uranium. Although ^{234}U has no application except for radiological studies, ^{234}U can be used to determined the applied enrichment processes.

Table I: Overview of the uranium classification based on the ^{235}U enrichment [31]

Abbreviation	Description	$n(^{235}\text{U})/n(\text{U})$	Application (example)
DU	Depleted Uranium	$< 0.72\,\%$	Shielding
NU	Natural Uranium	$\approx 0.72\,\%$	Research
LEU	Low-Enriched Uranium	$> 0.72\,\%$	Nuclear power plants
HEU	High-Enriched Uranium	$> 20\,\%$	Nuclear weapons

As gaseous diffusion is based on the absolute weight difference whereas the centrifugal enrichment is based on the relative weight difference, the enrichment efficiency of ^{234}U and ^{235}U differs on the used technique. As an example, Wood [32] performed calculations on the minor isotope behavior during enrichment of natural uranium to 5 %, using both gaseous diffusion and gas centrifugation. When employing gaseous diffusion, a $n(^{235}\mathrm{U})/n(^{234}\mathrm{U})$ ratio of 104.6 was calculated whereas for gas centrifugation a ratio of 109.3 was obtained. The ^{234}U can therefore be used as a valuable indicator for the used enrichment process [4].

^{236}U is, other than ^{234}U, ^{235}U and ^{238}U, an artificial isotope and only traces of ^{236}U are found in natural uranium, mostly due to atmospheric testing of nuclear weapons and incidents involving nuclear materials. ^{236}U is produced by neutron activation of ^{235}U and is therefore almost only present in irradiated nuclear fuels. This, in turn, makes it a valuable isotope for nuclear safeguards as it acts as indicator for reprocessing of spent fuels.

^{232}U and ^{233}U are both purely artificial and not found in nature. Both are produced during the irradiation of ^{232}Th, where ^{233}U is the dominant isotope produced. Due to the relative wide availability of ^{233}U from irradiated thorium, this isotope is commonly used as spike for isotope dilution mass spectrometric (IDMS) analysis of uranium; a known amount of ^{233}U is added to a dissolved uranium sample, after which the isotope ratios are measured by high accuracy mass spectrometric methods. Using the amount of spike added and the measured isotope ratios, the total uranium content can be quantified with high accuracy. Due to the short half-life and therefore high activity, ^{232}U has no wide-spread applications.

An overview of the isotopes of uranium, together with the most common origin and the typical application for nuclear safeguards is given in Table II.

Table II: Overview of the different isotopes of uranium

Isotope	Half-life	Origin	Safeguards relevance
^{232}U	68.9 a	Irradiation of ^{232}Th	Indicator for ^{232}Th irradiation
^{233}U	159.2 ka	Irradiation of ^{232}Th	Indicator for ^{232}Th irradiation
^{234}U	245.5 ka	Progeny of ^{238}U	Indicator for enrichment process
^{235}U	703.8 Ma	Primordial	Enrichment
^{236}U	23.42 Ma	Irradiation of ^{235}U	Indicator for reprocessing
^{238}U	4.468 Ga	Primordial	Enrichment

2.1.2 The Uranium-Oxide System

Uranium Trioxide. Uranium is known to exist in five oxidation states: U(II), U(III), U(IV), U(V), and U(VI). Of these oxidation states, U(IV) and U(VI) are the most commonly encountered oxidation states. The different possible stable oxidation states of uranium lead to a complex binary uranium-oxygen system, as shown in the binary phase diagram in Figure 2.2 [33].

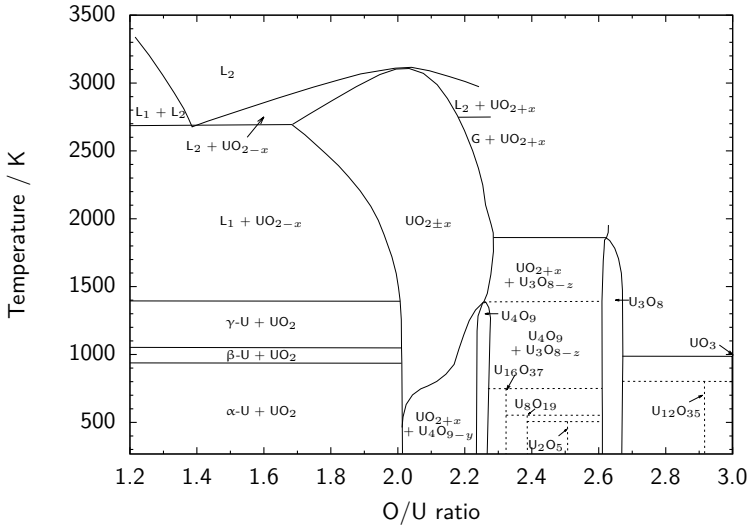

Figure 2.2: Phase diagram of the binary uranium-oxygen system [33].

As most uranium species dissolved in aqueous solutions consist of the hexavalent oxidation state, purely hexavalent uranium trioxide (UO_3) is often the first encountered uranium oxide after thermal decomposition. Due to the hexavalent oxidation state, UO_3 is relatively well soluble and therefore commonly used as intermediate product in the nuclear fuel cycle. The crystal structure of UO_3 strongly depends on the synthesis pathway and a total of seven different modifications are known, which are listed in Table III. Of these modifications, α-UO_3, β-UO_3 and γ-UO_3 are the most common encountered modifications [34–36].

Table III: Known modifications of UO_3 [33–35]

Formula	Structure	Space group	Color
UO_3(A)	Amorphous	-	Orange
α-UO_3	Orthorhombic	C222	Beige
β-UO_3	Monoclinic	$P2_1$	Orange
γ-UO_3	Orthorhombic	Fddd	Yellow
δ-UO_3	Cubic	$Pm\overline{3}m$	Deep red
ε-UO_3	Triclinic		Brick red
ζ-UO_3	Orthorhombic	$P2_12_12_1$	Brown

Triuranium Octoxide. Upon heating UO_3 above 500 °C, the uranium is partially reduced to a mixture of pentavalent and hexavalent uranium and forms the triuranium octoxide ($\overset{V}{U}_2\overset{VI}{U}\overset{II}{O}_8$, U_3O_8) compound [37, 38]. U_3O_8 consists of an orthorhombic structure and has a dark-green color [39]. Due to the mixed valance state of the uranium, U_3O_8 is considered to be the

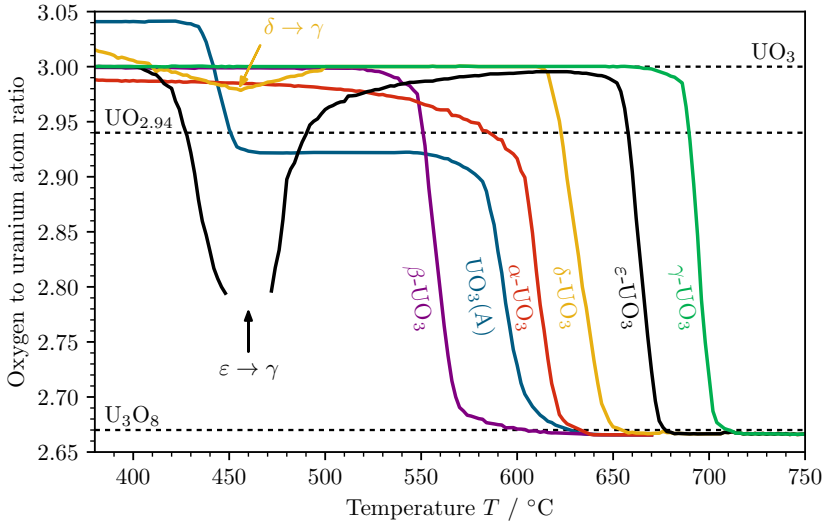

Figure 2.3: Oxygen to uranium atom ratio during the thermal decomposition of various modifications of uranium trioxide into triuranium octoxide [34, 35].

most stable uranium oxide compound and is commonly used for the storage of uranium, e.g. tails of depleted uranium from enrichment. Also, a number of certified reference materials are delivered as U_3O_8 materials.

The temperature at which UO_3 decomposes to U_3O_8 strongly depends on the modification of the UO_3. Whereas β-UO_3 decomposes at 560 °C, is the decomposition of γ-UO_3 found to occur at a temperature of 695 °C. Figure 2.3 shows the decomposition of the various modifications of UO_3 into U_3O_8, as measured by Hoekstra and Siegel [34] and Wheeler et al. [35]. Although most decompositions proceed with a single stage, ε-UO_3 is first recrystallized into γ-UO_3 before decomposition to U_3O_8 whereas the decomposition of amorphous UO_3 leads to the formation of $UO_{2.94}$ as an intermediate phase.

Uranium Dioxide. Uranium dioxide, consisting of pure tetravalent uranium, is obtained by heating U_3O_8 in a reducing atmosphere. Due to the purely tetravalent oxidation state of the uranium, UO_2 is highly insoluble and therefore used as nuclear fuels for most nuclear power plants. The tetravalent uranium is, however, rapidly oxidized at elevated temperatures in oxidizing atmospheres [40]. Even at room temperature, often super-stoichiometric uranium dioxide is formed, i.e. UO_{2+x}, where x goes up to 0.25 [33].

Uranyl Hydroxides. Due to the very low solubility of tetravalent uranium, uranium dioxide is barely soluble in water. However, upon contact with water, a part of the tetravalent uranium is oxidized to hexavalent uranium which, in turn, is soluble [41]. The oxidation can occur via a large number of oxidants, for example by H_2O_2, which could be formed after radiolysis of water:

$$H_2O_2 + UO_2(s) \longrightarrow OH^{\bullet} + OH^- + UO_2^+(s)$$
$$OH^{\bullet} + UO_2^+(s) \longrightarrow OH^- + UO_2^{2+}(s)$$

Many experimental determinations of the oxidative dissolution of UO_2 by H_2O_2 resulted in an activation energy between 24.5 kJ mol^{-1} to 27.2 kJ mol^{-1}, which is likely to consists of terms related to the oxidation of the tetravalent uranium and the decomposition of H_2O_2. The activation energy of the oxidation of tetravalent uranium is assumed to be around 30 kJ mol^{-1}. The oxidation of UO_2 by H_2O_2 typically leads to the formation of a studtite ($UO_4 \cdot 4\,H_2O$) surface layer whereas oxidation by O_2 typically leads to the formation of a (meta)schoepite ($UO_3 \cdot 2\,H_2O$) surface layer [41–43]. The hydration of U_3O_8 also leads to the formation of (meta)schoepite [44, 45].

2.1.3 Uranium in Aqueous Solutions

Uranium has a large number of possible oxidation states ranging from U(II) to U(VI), although the tetravalent and hexavalent oxidation states are predominantly found in uranium compounds. Tetravalent uranium is the most stable oxidation state of uranium and is nearly insoluble except in strong acidic solutions. On the contrary, hexavalent uranium is readily soluble in dilute acidic solution and usually present in solution as uranyl ion, UO_2^{2+} [33]. Similar to other actinoids (An), uranyl undergoes strong hydrolysis in aqueous solutions, where the general hydrolysis reaction can be given as:

$$p\,An^{z+} + q\,H_2O \rightleftharpoons An_p(OH)_q^{zp-q} + q\,H^+$$

Due to the hydrolysis of uranyl, uranyl containing solutions are often strongly acidic and a large number of uranyl hydroxides are known to be formed and eventually precipitate, as shown in the speciation diagram of uranium in water, given in Figure 2.4.

Uranyl Nitrate. One of the most common hexavalant uranium compounds is uranyl nitrate, $UO_2(NO_3)_2$, which forms uranyl nitrate hexahydrate upon drying. Uranyl nitrate hexahydrate is a bright yellow crystalline solid which is easily soluble in aqueous solutions. Uranyl nitrate hexahydrate is commonly used in the uranium industry as intermediate product and has been studied extensively in the past [30]. One of the main areas of interest is the thermal decomposition of uranyl nitrate hexahydrate to uranium trioxide, UO_3. The thermal decomposition of

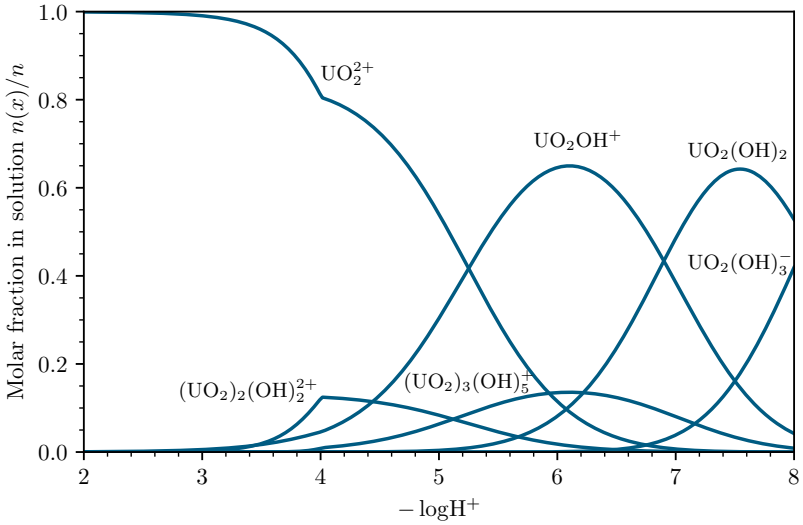

Figure 2.4: Simplified speciation diagram of U(VI) in water.

uranyl nitrate hexahydrate proceeds in two main stages; dehydration and denitration, although both stages have been observed to occur concurrently.

The dehydration has been described to proceed with up to six distinct steps, although the total number of steps and temperatures at which each step occurs differs strongly between various studies [46–51]. The most extensive study has been performed by Kozlova et al. [51], who measured six dehydration products, starting from 40 °C. Both the pentahydrate and tetrahydrate were not observed during previous studies; other authors [46, 50] report the direct dehydration of uranyl nitrate hexahydrate into uranyl nitrate trihydrate.

The dehydration of uranyl trihydrate into uranyl dihydrate has been reported by various authors [46, 49–51], although the temperature at which uranyl nitrate dihydrate is measured differs strongly; Kozlova et al. [51] observed the dehydration to proceed between 150 °C to 200 °C whereas Smith [50] measured the dehydration to occur at 72(1) °C. Anhydrous uranyl nitrate was found to be present at temperatures between 176 °C to 250 °C [47–51].

Although the dehydration was measured to be complete between 176 °C to 250 °C, first traces of uranium trioxide, the decomposition product after denitration, were found at temperatures as low as 176 °C [50], although Marshall et al. [46] explicitly mentions that no traces of uranium trioxide were measured at temperatures of 184 °C. Both Dawson et al. [47] and Kozlova et al. [51] report the denitration to proceed in two distinct steps between 250 °C to 400 °C and between 250 °C to 350 °C, respectively (Figure 2.5).

The thermal denitration of anhydrous uranyl nitrate is complicated by the auto-catalysis in

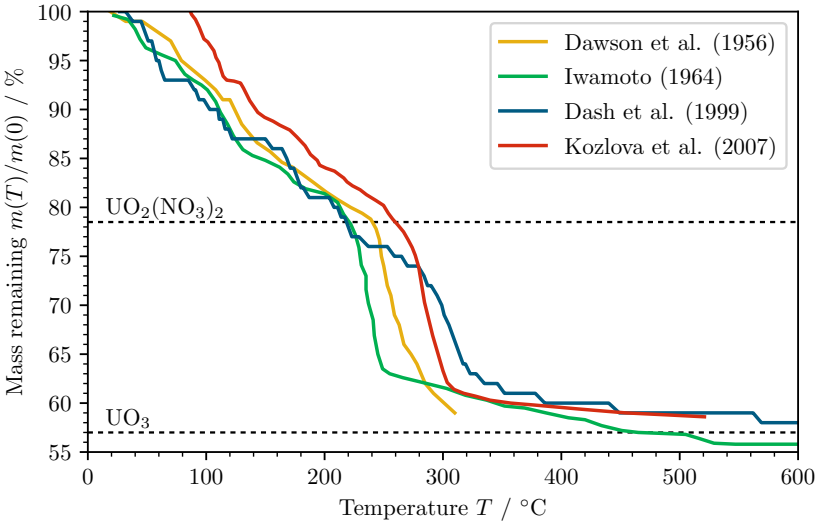

Figure 2.5: Thermogravimetric data on the thermal decomposition of uranyl nitrate hexahydrate in an air atmosphere [47, 51–53].

the presence of water vapor [49, 54]. Lodding and Ojamaa [49] studied the decomposition of uranyl nitrate in both air and steam. In air, the decomposition was measured to occur at 270 °C whereas the presence of steam reduced the decomposition temperature to 200 °C. The lower temperature at which decomposition took place in the presence of water vapor is caused by the reaction of released N_2O_5 with water to form nitric acid, which, in turn, lowers the oxygen partial pressure in the treatment atmosphere [49].

The thermal denitration of uranyl nitrate leads to the formation of uranium trioxide, although the conditions of the thermal decomposition influences the crystal structure of the obtained uranium trioxide. If no melting occurs during decomposition, amorphous UO_3 is obtained, which crystallizes to α-UO_3 between 450 °C to 520 °C. If melting occurs, either β-UO_3 or γ-UO_3 is obtained when the uranyl nitrate is heated with a fast ($\approx 35\,°C\,min^{-1}$) or slow ($\approx 3.5\,°C\,min^{-1}$) heating rate, respectively. The addition of sulphamic acid to the uranyl nitrate leads to the formation of amorphous UO_3 or ζ-UO_3 for treatments at 440 °C and 500 °C, respectively. [35]

Uranyl Acetate. The thermal decomposition of uranyl acetate dihydrate, $UO_2(CH_3COO)_2 \cdot 2\,H_2O$, follows a less complex pathway compared to uranyl nitrate (Figure 2.6) and only a single dehydration and decomposition step were identified. The dehydration from uranyl acetate dihydrate to anhydrous uranyl acetate was measured to occur between 95 °C to 140 °C [55–58]. The decomposition of the anhydrous uranyl acetate occurs by the fission of the U-C bonds

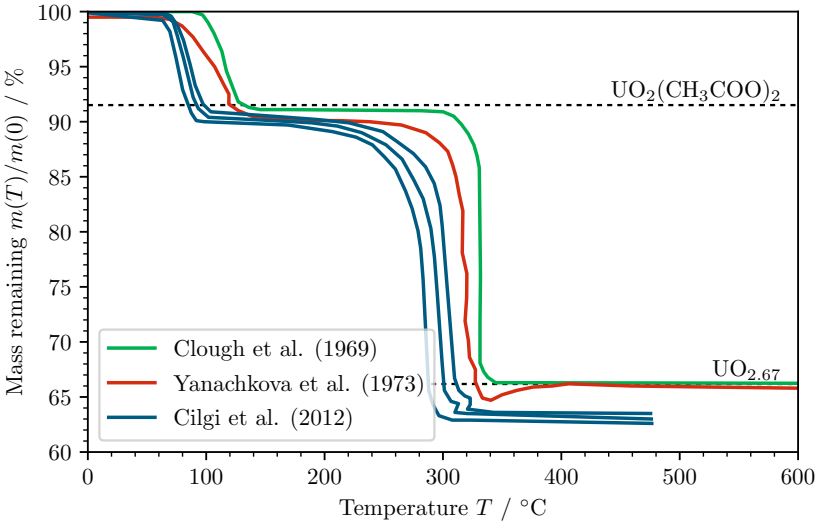

Figure 2.6: Thermogravimetric data on the thermal decomposition of uranyl acetate dihydrate in an air atmosphere [55, 56, 58].

and is accompanied by the reduction of the remaining uranyl to tetravalent uranium, resulting in the formation of uranium dioxide. However, when heated in an oxidizing atmosphere, the formed uranium dioxide is instantaneously oxidized and forms triuranium octoxide. The thermal decomposition of anhydrous uranyl acetate to uranium dioxide occurs around 345 °C [55–59].

Studies performed in a nitrogen atmosphere showed a similar behavior compared to the thermal decomposition in air, except for the oxidation of the formed uranium dioxide into triuranium octoxide and uranium dioxide was found as final decomposition product [58].

Uranyl Chloride. The thermal decomposition of uranyl chloride, UO_2Cl_2, was investigated less extensively and has been described by Sato et al. [60]. The dehydration of uranyl chloride trihydrate proceeds progressively (Figure 2.7) and anhydrous uranyl chloride is obtained at 175 °C. The decomposition of uranyl chloride into uranium trioxide also progresses continuously, although one intermediate product was identified. Between 220 °C to 430 °C, $U_2O_4Cl_2$ is obtained which successively decomposes to uranium trioxide around 490 °C. After decomposition, super-stoichiometric amorphous uranium trioxide was obtained which recrystallizes to α-UO_3 around 520 °C.

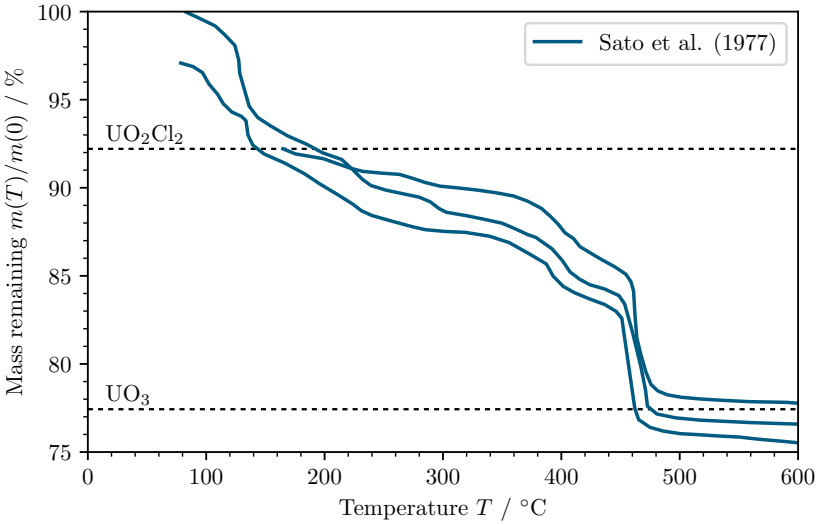

Figure 2.7: Thermogravimetric data on the thermal decomposition of hydrated uranyl chloride in an air atmosphere [60].

2.2 Aerosol-Based Particle Production Methods

2.2.1 Particle Formation Process

The production of micrometer-sized spherical particles for microanalytical applications has received considerable attention over the last decades due to the increased capabilities of analytical methods suitable of analyzing such materials. One of the most commonly employed methods to produce uranium microparticles is based on the spray-pyrolysis of a uranium containing aerosol.

During spray-pyrolysis, at first an aerosol is generated, where the aerosol droplets consist of a specific solute (e.g. uranium) dissolved in a volatile solvent (e.g. water). The aerosol droplets are heated, during which the solvent evaporates and the solute concentration within the droplet increases. Once the solute concentration within the droplets exceeds the solubility limit, the solute starts to precipitate, leading to the formation of a solid particle consisting of the precipitated solute.

The so-called evaporation/precipitation process has been described in detail by Reuge et al. [61], who provided three pathways at which the precipitation of the solute can occur and the effect of the precipitation upon the final particle morphology. Figure 2.8 shows the different evaporation/precipitation reactions which could occur after reaching saturation and the effect on the final particle morphology.

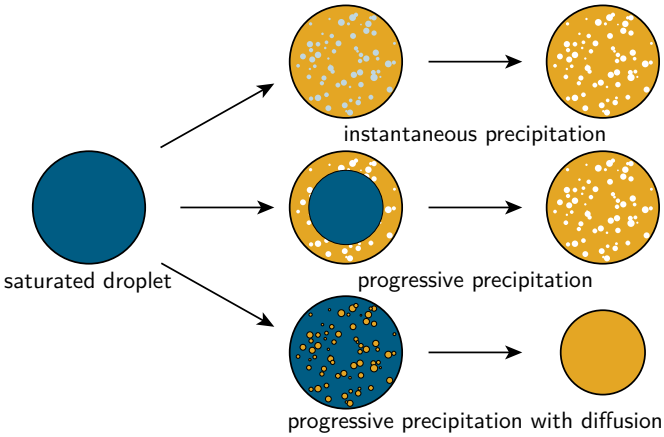

Figure 2.8: Schematic overview of the formation of particles from droplets upon evaporation of the solvent [61].

1. Instantaneous precipitation. In the simplest way, the precipitation of the solute occurs instantaneous throughout the droplet upon reaching the solubility limit. As the precipitation occur homogeneously throughout the particle, the diameter of the solid particle is similar to the diameter of the saturated droplet. As the density of the precipitated species is typically higher, pores are produced homogeneously throughout the particle.

2. Progressive precipitation. Instead of instantaneous precipitation of all solute, the solute could precipitate until the concentration has decreased below the saturation limit. Upon further evaporation of the solvent, the solute concentration exceeds the solubility limit and continues to precipitate. As the evaporation of the solvent occurs at the liquid/gas interface, the precipitation occurs near the boundary and therefore proceeds inwards with continuous evaporation of the solute. As the precipitation commences at the droplet boundary, the final particle size is similar to the size of the initially saturated droplet and pores are formed homogeneously throughout the particle.

3. Progressive precipitation with solute diffusion. The previous model assumed local precipitation of the solute once exceeding the saturation limit. However, if diffusion of the solute occurs before precipitation, the concentration of the droplet can be assumed to be homogeneous throughout the droplet and the precipitation can occur at any point within the droplet. If such diffusion occurs, nanoclusters of the precipitated solute are formed throughout the droplet. With further evaporation of the solvent, the nanoclusters agglomerate and finally yield a dense particle consisting of agglomerated nanoclusters, although a porosity gradient throughout the particle is typically observed with an increased porosity towards to particle surface.

In most cases, the solute used for particle production is well soluble. In order to decrease the solubility and therefore increase the stability of the produced particles, the obtained particles consisting of the precipitated solute are typically heated, during which the solute decomposes into a chemically more stable compound. The thermolysis of precipitated particles has been described by Jain et al. [62] (Figure 2.9), who distinguished two main pathways, depending on whether melting of the solute occurs before chemical decomposition.

The chemical decomposition of precursor A into the decomposition product B(s) can be expressed as:

$$\mathrm{A} + z\mathrm{G(g)} \longrightarrow x\mathrm{B(s)} + y\mathrm{C(g)}$$

In case of melting of A before decomposition, reactant A with a volume $M_\mathrm{A}/\rho_\mathrm{A}$ results in compound B with a volume of $xM_\mathrm{B}/\rho_\mathrm{b}$, where M and ρ are the molar weight and density of the respective species, respectively. If the total volume reduction exceeds 0.16 (equation 2.1), the decomposition results in the formation of hollow particles whereas smaller volume reductions generally lead to the formation of dense particles. Although the model was validated by Jain et al. [62] on a large number of single metal and single metal oxide systems, other effects, such as the release of decomposition gasses, might affect the morphology of the obtained particles.

$$x\frac{M_\mathrm{B}}{\rho_\mathrm{b}} < 0.16\frac{M_\mathrm{A}}{\rho_\mathrm{A}} \tag{2.1}$$

If no melting occurs before chemical decomposition, the size of the decomposed particle depends on the size of the precipitated particle. Based on the percolation theory, Jain et al. [62] derived equation 2.2, which can be used to estimate whether decomposition results in the formation of a hollow or dense particle. In equation 2.2, d_p is the size of the droplet at onset

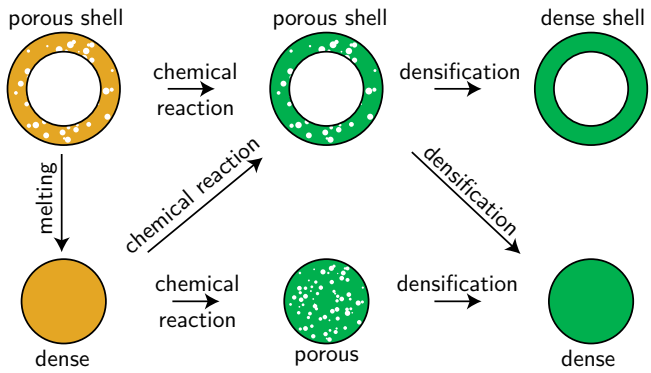

Figure 2.9: Schematic overview of the thermolysis of dried aerosol particles to form decomposed microparticles. Adapted with permission from Jain et al. [62] (see page 129).

of precipitation whereas d_{ps} is the theoretical size of the precipitated droplet assuming the formation of a dense particle. If the volume reduction during precipitation and decomposition remains smaller than 0.16, dense particles are formed, although the release of decomposition gasses could alter the particle morphology [63].

$$\rho_{\mathsf{A}} \left(\frac{d_{\mathsf{ps}}}{d_{\mathsf{p}}} \right)^3 < 0.16 \frac{\rho_{\mathsf{B}}}{x} \frac{M_{\mathsf{A}}}{M_{\mathsf{B}}} \tag{2.2}$$

2.2.2 Applied Aerosol-based Particle Production Methods

In order to support the IAEA's safeguards analytical services, various attempts were undertaken to produce microparticles containing fissile materials based on the spray-pyrolysis of aerosols.

Spinning Disk Aerosol Generator. The first attempts to produce uranium microparticles by spray-pyrolysis of an aerosol was performed by Tushingham [64], where a uranium containing aerosol was generated using a spinning disk aerosol generator. A diluted uranium solution was added drop-wise onto a rapidly rotating disk. Upon contact of the droplets with the disk, the droplets are forced outwards eventually being ejected from the disk as a fine aerosol [65, 66]. The ejected droplets were dried and thermally treated from which microparticles with sizes between 0.1 µm to 3.5 µm were obtained [64, 67]. A number of produced particles were investigated by laser ablation-inductively coupled plasma-mass spectrometry (LA-ICP-MS), where the isotopic composition of the particles was found to reflect the specified isotopic composition, although accurate analysis was complicated by the wide spread of particle size [67].

Atomizer. A second method using spray-pyrolysis was employed by Shinonaga et al. [68] to produce plutonium microparticles. An aerosol was generated from a freshly purified plutonium solution using an atomizer [69, 70]. In an atomizer, compressed air passes through an orifice, which causes a pressure difference before and after the orifice. Such produced pressure difference leads to the generation of an aerosol from the nearby located solution. The produced aerosol was transported through a condenser and a furnace set to 500 °C, before particles were extracted using a Berner-type low-pressure impactor.

The produced particles consisted of a spherical shape, although a wide particle size distribution was obtained (Figure 2.10). The produced particles were investigated with a wide range of techniques. The plutonium isotopic composition was measured by thermal ionization mass spectrometry (TIMS), sector field-ICP-MS (SF-ICP-MS) and α-spectrometry and was found to be consistent with the initially used CRM. The particles were also investigated by µ-Raman spectroscopy, from which was concluded that the particles consisted of a cubic plutonium dioxide (PuO_2) phase. Such a phase would be expected based on studies performed by Waterbury et al. [71] on the thermal decomposition of plutonyl nitrate. The particle density was estimated

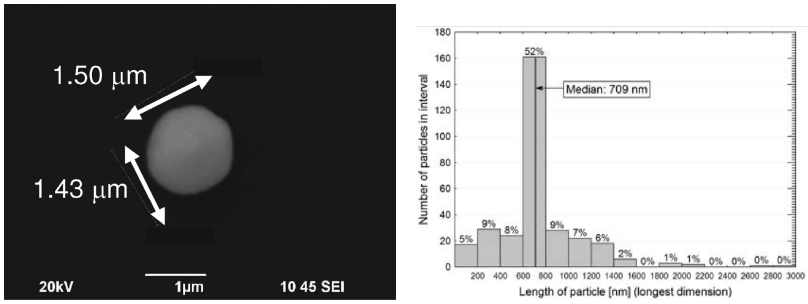

(a) SEM micrograph **(b)** Particle size distribution

Figure 2.10: SEM micrograph and particle size distribution of plutonium microparticles produced by spray-pyrolysis of an aerosol generated using an atomizer. Reprinted with permission from Shinonaga et al. [68] (see page 129).

to be between $4\,\mathrm{g\,cm^{-3}}$ to $9\,\mathrm{g\,cm^{-3}}$, which is lower than the theoretical density of PuO_2 of $11.5\,\mathrm{g\,cm^{-3}}$ [72].

Vibrating Orifice Aerosol Generator. Each of the previous studies resulted in the formation of particles with a polydisperse size distribution. To produce particles with a monodisperse particle size distribution, a vibrating orifice aerosol generator (VOAG) was employed to produce a monodisperse aerosol from solutions with known isotopic compositions. The operation of a VOAG is described in more detail in section 3.1.

First particles were produced from uranyl nitrate solutions [74–76], where the produced aerosol was guided through a series of furnaces, during which the particles were heated up to 800 °C. After cooling down, the particles were collected on Nuclepore filters. The produced particles showed a high degree of sphericity and a narrow particle size distribution was obtained (Figure 2.11). The particle size distributions typically showed two or three particle populations.

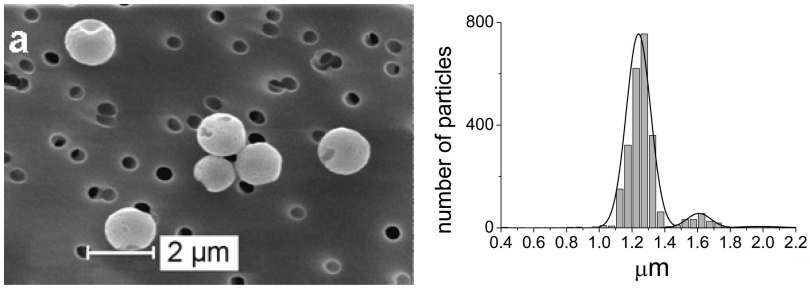

(a) SEM micrograph **(b)** Particle size distribution

Figure 2.11: SEM micrograph and particle size distribution of plutonium microparticles produced by spray-pyrolysis of an aerosol generated using a vibrating orifice aerosol generator. Reprinted with permission from Ranebo et al. [73] (see page 129).

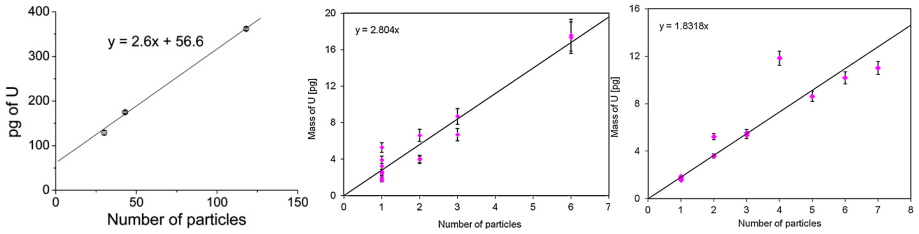

(a) U020-A [76] **(b)** U100 [77] **(c)** U020-A [77]

Figure 2.12: ID-TIMS analysis of uranium microparticles produced from various CRMs by spray-pyrolysis of an aerosol generated using a vibrating orifice aerosol generator. Reprinted with permission from Ranebo et al. [76] and Kraiem et al. [77] (see page 129).

The second and third populations were described to consist of particles with respectively two or three times the amount of uranium compared to the main population. The isotopic composition of the particles was confirmed to match the used CRM.

The uranium content of single particles and of a select number of particles was measured by isotope dilution (ID) TIMS [76, 77], for which particles were transferred using a micromanipulator onto a rhenium filament. The transferred particles were dissolved in nitric acid and a known amount of ^{233}U spike was added. Figure 2.12 shows the determined uranium content as function of the number of particles. All of the collected results show a high degree of linearity between the uranium mass and particle number, which shows the constant mass per particle. Comparison of the particle mass and volume, as obtained from SEM investigations, resulted in particle densities significantly lower compared to the theoretical density of both UO_3 ($7.2\,g\,cm^{-3}$) and U_3O_8 ($8.38\,g\,cm^{-3}$).

Particles were produced using the same setup consisting of a mixture of uranium and plutonium and pure plutonium [73, 78]. The particles were investigated by SIMS, which confirmed that the isotopic composition of both uranium and plutonium matches the initially used materials.

2.2.3 Comparison of Alternative Particle Production Methods

Other than the production of actinoid microparticles for microanalytical applications by spray-pyrolysis, a number of different methods were employed to produce such particles. The obtained particles from such methods typically show a polydisperse particle size distribution. In general, two types of particles were produced; particles containing a high fraction of actinoids and particles with only a minor fraction of actinoids.

Grinding/Milling. Raptis et al. [79] reported the production of microparticles by mixing a borosilicate glass melt with U_3O_8. A borosilicate glass with a composition of 70 % SiO_2, 15 % B_2O_3, 10 % Na_2O, 4 % CaO and 1 % Al_2O_3 was produced by mixing of the various solids and

heating the mixtures at 1400 °C. The produced melt was cast in water and subsequently milled and filtered to obtained glass particles with a size around 10 µm. The glass particles were mixed with U_3O_8 with the desired isotopic composition which was subsequently heated to 1450 °C, after which the melt was cast into water. The heating and casting was repeated four times to ensure thorough mixing of the uranium with the glass. The obtained uranium-doped glass was milled and filtered in a glove-box to obtain micrometer sized particles.

The obtained particles showed a wide particle size distribution and an irregular particle shape (Figure 2.13). The particles were measured to contain roughly 5 % (weight) uranium. Particles with various isotopic compositions, ranging from natural to high-enriched, were produced where the isotopic composition was confirmed to match the initially used CRMs [80].

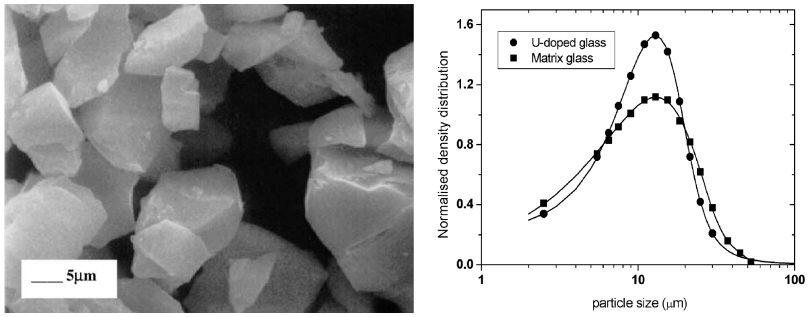

(a) SEM micrograph **(b)** Particle size distribution

Figure 2.13: SEM micrograph and particle size distribution of glass particles containing 5 % uranium, prepared by milling of a uranium glass. Reprinted with permission from Raptis et al. [79] (see page 129).

Ion Exchange. An alternative method to produce spherical microparticles with a small fraction of actinoids is by the adsorption on actinoids on aluminosilicate clay particles, as used by NIST for the production of a certified reference material of particles containing plutonium [81] and a mixture of uranium and plutonium [82].

Aluminosilicate clay particles were initially loaded with sodium, which were subsequently contacted with a plutonium sulfate solution, during which ion exchange leads to the adsorption of plutonium by the particles. After filtration and washing, the plutonium loaded particles were nebulized and introduced into a furnace set to 1150 °C, which causes the formation of glass particles with embedded plutonium. To reduce the spread of particle size, the particles were passed through a centrifugal aerosol spectrometer, where the particles are deposited onto a substrate separated by their aerodynamic diameter. Segments of the obtained foil were separated to obtain the produced particles with a narrowed particle size distribution.

The produced plutonium microparticles were found to have a spherical shape and a particle size between 1.4 µm and 2.0 µm with a median diameter around 1.75 µm. The chemical composition of the produced particles was analyzed by wavelength-dispersive X-ray spectrom-

etry (WDX), from which a plutonium weight fraction of $22.9\,\mathrm{mg\,g^{-1}}$ was obtained. Apart from silicon and aluminum, roughly $50\,\mathrm{mg\,g^{-1}}$ magnesium were found and traces of sodium, calcium and iron were measured. The isotopic composition of the plutonium in the particles was confirmed to match the initial plutonium sulfate by TIMS. Similar particles were produced consisting of a mixture of plutonium and uranium, where the produced particles contained about $22\,\mathrm{mg\,g^{-1}}$ uranium and $1.1\,\mathrm{mg\,g^{-1}}$ plutonium.

Uranium Adsorbed Silica Particles. The production of monodisperse microparticles with only a small fraction of uranium was investigated by Park et al. [83], combining the production of monodisperse particles from using a spray-pyrolysis procedure and ion exchange. At first, an aerosol was produced using a vibrating orifice aerosol generator from a sodium silicate solution. The aerosol droplets were dried and finally collected in a H_2SO_4 solution bath. To narrow the particle size distribution of the produced silica particles, an additional size fractionation step was performed based on gravitational sedimentation. The obtained silica particles were stored for 24 hours in a uranium solution, during which the uranium was absorbed onto the silica particles. After adsorption, the particles were filtered, washed and finally heated at 950 °C to obtain stable particles.

Figure 2.14 shows a SEM micrograph and the measured particle size distribution of the obtained particles. The particle distribution showed a wide spread (ca. $10\,\%$, $k = 1$), although the distribution appears to normally distributed around 10 µm. Additional particles were produced with particles sizes ranging from 5 µm to 20 µm. The uranium fraction of the particles was measured by EDX, from which a weight fraction around $0.15\,\mathrm{g\,g^{-1}}$ was found. The particles' chemical structure of the uranium was determined to consist of a U_3O_8 phase by XRD.

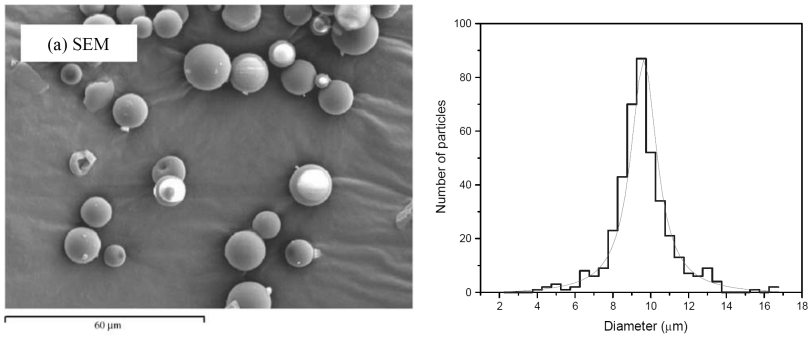

(a) SEM micrograph **(b)** Particle size distribution

Figure 2.14: SEM micrograph and particle size distribution of uranium microparticles produced by uranium adsorption on silica particles. Adapted with permission from Park et al. [83] (see page 129).

Controlled UF_6 Hydrolysis. The previously described methods produced spherical glass particles with a small fraction of actinoids. One of the alternative approaches to produce spherical particles containing a high fraction of actinoids is by the controlled hydrolysis of uranium hexafluoride [21, 22]. UF_6 with the desired isotopic composition in a sealed glass vial is introduced in a closed reaction chamber. Both the humidity (68 %) and temperature (21 °C) of the reaction chamber are regulated closely. After opening of the glass vial and sublimation of the UF_6, the UF_6 is hydrolyzed in the reaction chamber, causing the formation of spherical uranyl fluoride (UO_2F_2) particles:

$$UF_6(g) + 2\,H_2O(g) \longrightarrow UO_2F_2(s) + 4\,HF(g)$$

The formed UO_2F_2 particles precipitate onto graphite disks positioned at the bottom of the reaction chamber. The graphite disks are removed and heated using a quartz lamp, during which the UO_2F_2 decomposes into U_3O_8, which enhances the stability of the collected particles.

Particles produced by the controlled hydrolysis show a high degree of sphericity, although a wide particle size distribution was observed (Figure 2.15). The isotopic composition of the collected particles was confirmed to match the composition of the initial UF_6 and the produced particles were used in two interlaboratory comparison exercises, NUSIMEP-6 [23] and NUSIMEP-7 [24], where the latter exercise also included a sample consisting of a mixture of particles with two distinct isotopic compositions, which were produced by two subsequent depositions. The homogeneity and short-term stability of the particles was investigated and concluded to be fit for purpose for the interlaboratory comparison exercises.

In addition to the isotopic measurements, the produced particles were investigated by μ-Raman spectroscopy to determine the chemical phase [84, 85]. These measurements yielded a UO_2F_2 phase, although laser beam induced decomposition of the microparticles forming U_3O_8 was observed. The fluoride content of particles was also investigated [86] as indicator for the particle age, as a reduction of the fluoride content in time was observed.

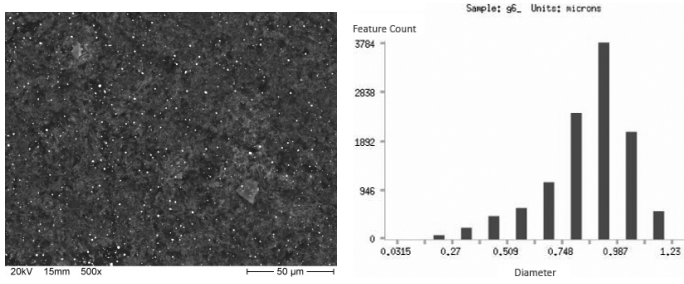

(a) SEM micrograph **(b)** Particle size distribution

Figure 2.15: SEM micrograph and particle size distribution of uranium microparticles produced by the controlled hydrolysis of UF_6. Adapted with permission from Kips et al. [21] (see page 129).

2.3 Microanalytical Methods

Numerous methods are available to analyze materials. Within this section, a select number of methods will be described which are capable of analyzing properties of micrometer-sized objects, such as microparticles.

2.3.1 Imaging Techniques

Visual investigation of objects is a wide-spread method to examine morphological properties of objects. For small objects, reflected light originating from an object can be passed through various lenses, causing a magnification of the object and therefore allows for visual interpretation of features not visible by the human eye. Such optical light microscopes usually illuminate a sample with a beam of photons with a wavelength in the visible light spectrum. However, as the wavelength of visible light is around a few hundred nanometers, the lower size limit of objects which can be investigated with typical light microscopes lies around a few micrometers.

Scanning Electron Microscopy. Scanning electron microscopes (SEMs) are commonly used to investigate objects smaller than a few micrometers. Instead of photons, such microscopes probe the sample with electrons. Similar to light microscopy, a fraction of the electrons are scattered by the sample surface and detection of such reflected electrons provides information on the sample surface. However, where light microscopes typically contain area sensors which provide information regarding the origin of the detected photons, electron microscopes normally contain only a single detector measuring the total intensity of scattered electrons. To obtain lateral information of a sample surface, the illumination electrons are focused to a beam with a diameter of a few nanometers. The focused electron beam is scanned over the sample surface in a step-wise fashion, were during each step the number of reflected electrons are measured.

Upon contact with the sample material, the illumination electrons can undergo various interactions resulting in the reflection of electrons. These interactions can basically be classified into two groups, elastic and inelastic scattering (Figure 2.16). Due to the negative charge of electrons, the electrons in close proximity of a nucleus are reflected, i.e. elastically scattered. The number of such elastically scattered electrons strongly depends on the charge of the nucleus and therefore the number of protons, i.e. Z. The relative amount of backscattered electrons increases with increasing proton number and can therefore be used to obtain information regarding the elemental composition of the sample surface. During inelastic scattering, the illumination electron causes the ionization of the sample material, resulting in the ejection of a K-orbital electron. As such ejected electron has a lower energy compared to the illuminating electrons, the mean path such secondary electrons can travel through the sample material is smaller. Detection of secondary electrons therefore provide a higher lateral resolution compared to the detection of backscattered electrons.

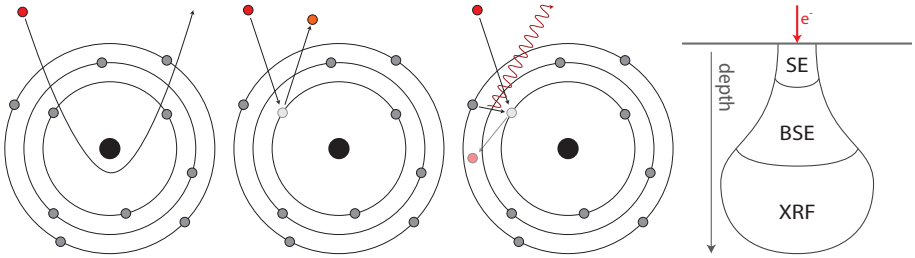

(a) Backscatter electron **(b)** Secondary electron **(c)** X-ray fluorescence **(d)** Interaction

Figure 2.16: Overview of the interactions of incident electrons with an atom, used for imaging with a scanning electron microscope.

Focused Ion Beam Milling. Charged particle beams like ion beams can be focused to nanometer-sized beams, which allows the imaging of samples by ion microscopy. However, due to the larger weight of ions compared to electrons, ions exhibit a higher kinetic energy and upon contact with a sample, atoms from the sample are ablated by the incident ions. This opens the possibility of machining nano- and micrometer-sized objects and removal of material in a controlled fashion. This way, micrometer-sized samples can be milled with the ion beam. During the ablation, both secondary ions and electrons are generated, where the secondary ions could be transported into a mass spectrometer for determination of the elemental or isotopic composition of the sample (section 2.3.3) whereas the generated secondary electrons could be used for imaging. The combination of a focused ion beam (FIB) with a SEM is commonly used to ablate sample materials followed by imaging, thereby revealing the internal morphology.

2.3.2 Elemental Analysis

X-Ray Spectroscopy. After ionization of elements, high orbital electrons are transferred to the vacancies in the low-orbitals. The excess energy stemming from the difference in bonding energy between high and low orbitals is emitted as a photon (Figure 2.16c). The energy of such emitted photons is specific for the electron transition and detection of such photons can therefore provide information regarding the chemical composition of the ionized material. There are a number of techniques employing such emitted photons to determine the elemental composition of samples.

Ionization induced by electrons, for example during SEM imaging, is one of the most common techniques to obtain high lateral resolution measurements of the elemental composition of a sample. The emitted photons can be detected by two types of detectors, either energy or wavelength based. With energy dispersive X-ray spectroscopy (EDX), the emitted photons are measured by a multichannel energy-dispersive detector, which allows the instantaneous recording of the energy spectrum of the emitted photons. This techniques therefore provides rapid

measurements results. However, the energy resolution of EDX is rather poor and such measurements can therefore suffer from peak overlap. Wavelength-dispersive X-ray spectroscopy (WDX) determines the photon wavelength using crystal diffraction with a far higher resolution and can therefore provide a much better elemental discrimination, although with much longer measurement times.

X-Ray Fluorescence. Another method using emitted photons to determine the elemental composition is X-ray fluorescence (XRF) spectroscopy, in which the sample is not ionized using electrons but with photons. Although the spatial resolution of photons beams is typically lower compared to electron beams, very high intensity focused photon beams can be generated using synchrotrons, allowing rapid analysis of very small amount of materials.

2.3.3 Isotopic Analysis

A different technique to analyze the elemental composition of micrometer-sized objects is using mass spectrometers. In general, a mass spectrometer ionizes sample material and subsequently separates the ionized compounds based on the ion mass and charge. Such mass spectrometers are therefore not only capable of analyzing elements, but also isotopes of a single element.

Three types of mass spectrometers are commonly used: quadruple, time-of-flight and sector field. In a quadruple mass spectrometer (Q-MS), four poles are rapidly fluctuating the polarity, due to which the charged ions are constantly deflected. The fluctuation of the polarity can be adjusted in such a way that only ions with a single mass-to-charge ratio reach the detector, while all other ions collide with the rods. A quadruple mass spectrometer can only detect ions with a single mass-to-charge ratio at a time, by changing the fluctuation frequency ions with different mass-to-charge ratios can be detected.

In a sector field mass spectrometer (SF-MS), charged ions are deflected by magnetic and/or electric fields. With increasing mass-to-charge, the deflection angle changes and allows for the separation of ions with a single mass-to-charge ratio. Although sector field mass spectrometers have a much higher mass resolution compared to quadruple mass spectrometers, SF-MS are much more expensive and less versatile compared to Q-MS.

A third type of mass spectrometer commonly used is a time-of-flight mass spectrometer (ToF-MS). Whereas a Q-MS and a SF-MS perform continuous measurements of a single mass-to-charge ratio, in a ToF-MS, charged ions travel a distance within the spectrometer, where the time required to travel the predefined distance depends on the ion mass-to-charge ratio. A ToF-MS therefore allows for the collection of a mass spectra with a single pulse of ions (Figure 2.17).

Each of these mass spectrometers require charged ions as input. To obtained such charged ions, a number of techniques are commonly available. The most common technique is an inductively coupled plasma (ICP) source. In an ICP, a solution containing the analyte is

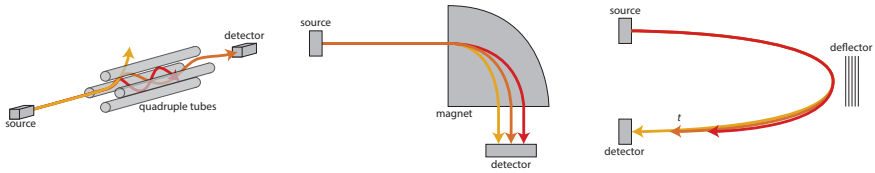

(a) Quadruple **(b)** Sector field **(c)** Time-of-Flight

Figure 2.17: Schematic overview of the most common types of mass spectrometers.

nebulized and introduced into a plasma, in which the atoms are vaporized and introduced into the mass spectrometers.

Most ICP systems require a solution as input. For solid samples, either the sample needs to be dissolved or a fraction of the material can be ablated by a laser puls. The ablated material can then be transferred into an ICP source. Such laser ablation-inductively coupled plasma (LA-ICP) systems are therefore commonly used to analyze sample surfaces, as a spatial distribution can be obtained by scanning the laser over the surface. LA-ICP-MS does, however, suffer strongly from molecular interferences (e.g. $[^{236}U]$ and $[^{1}H^{235}U]$) and the laser diameter is typically rather large (ca. 20 µm).

Another method to produce charged ions for mass spectrometric analysis is by secondary ion (SI), where a beam of charged ions (typically O^- of Cs^+) is used to vaporize a part of the solid sample surface. The vaporized secondary ions can then be introduced directly into a mass spectrometer. Such primary ion beams can be focused to much smaller spot sizes compared to laser beams and therefore allow for spatial scans of sample surfaces at lateral higher resolution compared to LA-ICP-MS systems.

Another ion source for mass spectrometers is by thermal ionization (TI), where a solid sample is placed onto a filament consisting of rhenium. A high current is applied to the filament which leads to the vaporization of elements within the sample. The major advantage of TI is the selectivity for a specific element. As an example, Lee et al. [87] determined that optimal vaporization of plutonium was achieved at a current of 2.2 A whereas the optimal vaporization of americium was achieved at a current of 1.5 A. By selectively vaporizing plutonium, the ^{241}Pu isotope can be measured free of ^{241}Am interferences.

2.3.4 Structural Analysis

X-Ray Diffraction. X-ray diffraction (XRD) is a non-destructive analytical technique to qualitatively and quantitatively examine crystal structures. In XRD, a crystalline sample is irradiated with monochromatic X-rays with a wavelength λ at an incident angle θ. Depending on the crystal structure of the irradiated solid, the incident photons are scattered, where the scattering angle depends on the lattice distance d, as described by Bragg's equation:

$$2d \cdot \sin\theta = \lambda \cdot n \tag{2.3}$$

The scattered photons are collected by a detector; either a single detector where the angle between the incident photons and the detector is varied or an area detector which allows the simultaneous collection of the photons scattered at different angles.

If the sample would consist of a single crystal or all crystals would be oriented in the same direction, all photons would be scattered in a similar fashion. When using an area detector, the collected diffraction pattern consists of spots of high scattered photon intensity. On the other hand, when samples are analyzed with numerous crystals facing randomly in all directions, e.g. powders, the scattering would be more diffuse and diffraction bands are obtained instead of spots. However, by reducing the X-ray beam size, a smaller fraction of the sample is irradiated. Therefore, nanocrystalline domains within a powdered sample can be distinguished using μ-XRD (Figure 2.18).

Although 2-dimensional diffraction patterns provide information regarding the crystallinity of the investigated samples, comparison of the lattice spacing of single crystal and powdered samples is complicated. To simplify such comparison, an azimuthal integration of the collected diffraction patterns leads to a diffractogram, i.e. the scattered photon intensity versus the diffraction angle. Such diffractograms can be used for qualitative comparison with reference diffractograms or can be used to estimate the lattice spacing of the observed reflexes using

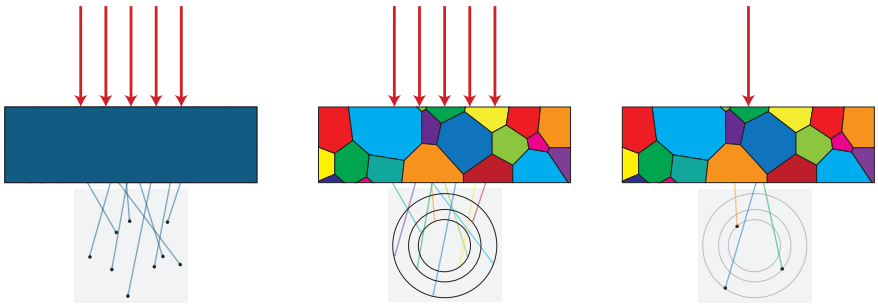

(a) Single-crystal **(b)** Powder **(c)** μ-XRD

Figure 2.18: X-ray diffraction of single crystals, powdered samples and using a micro-focused photon beam.

Bragg's equation (Equation 2.3). The lattice spacing depends on the crystal structure and lattice parameters of the measured phase and can therefore be used to estimate the lattice constants of the measured phase. For example, the lattice spacing of an orthorhombic phase can be calculated as

$$d = \frac{1}{\sqrt{\frac{h^2}{a^2} + \frac{k^2}{b^2} + \frac{l^2}{c^2}}} \tag{2.4}$$

which simplifies to

$$d = \frac{a}{\sqrt{h^2 + k^2 + l^2}} \tag{2.5}$$

for cubic phases [88, 89].

X-Ray Absorption Spectroscopy. X-rays can undergo a number of interactions in close vicinity of atoms and molecules. Other than elastic scattering, as used for X-ray diffraction, if the energy of the X-rays is sufficiently high, the photon energy can be transferred to electrons which causes the electrons to be ejected. The energy required to ionize atoms depends on the number of protons and electron shell, but also on the local coordination chemistry. As an example, the binding energy of the $2p_{3/2}$ electron of a uranium atom (L_{III}) is 17.166 keV. However, with increasing oxidation state of the uranium, the binding energy increases slightly. Minor changes of the absorption energies are used in X-ray absorption spectroscopy (XAS) to obtain information regarding the local coordination environment and chemistry [90].

The measurement of the shift of absorption energy can be achieved by irradiation of a sample with mono-energetic photons, which typically requires a synchrotron source for sufficient photon intensity. The absorption of photons can be measured directly by a detector located behind the sample or by a fluorescence detector, as fluorescence X-rays are emitted by electrons occupying the electron vacancy created by the ionization. During a typical XAS measurement, the energy of the incident photons is gradually increased and an absorption spectrum as function of incident photon energy is recorded. Such a collected absorption spectrum can be divided into two regions; the region around the main absorption band, the so-called white-line, is used for X-ray absorption near-edge structure (XANES) spectroscopy whereas the region beyond the white-line is used for extended X-ray absorption fine-structure (EXAFS) spectroscopy. As the white-line depends on the oxidation state of the ionized atom, XANES is often used for qualitative determination of the oxidation state whereas EXAFS is typically used to estimate the local coordination environment and bond-lengths [91].

3 Materials and Methods

The production of microparticles in this work is based on the spray-pyrolysis of a monodisperse aerosol generated using a vibrating orifice aerosol generator (VOAG). Within this chapter, the operation of a VOAG is described in section 3.1 whereas the established particle production setup is described in section 3.2. Section 3.3 describes the preparation of the required liquid feed solutions whereas the typical measurement conditions of the various analytical techniques used within this work are described in section 3.4.

3.1 Aerosol Generation

A vibrating orifice aerosol generator is based on the formation of a liquid jet by forcing a solution through an orifice. By applying an oscillating frequency to the orifice, the liquid jet breaks-up into droplets [92]. In order to obtain a liquid jet, at first the liquid feed should be forced through the orifice at a minimal volume flow ($Q_{\mathrm{V,min}}$), which depends on the surface tension (σ_{f}) and the density (ρ_{f}) of the feed solution and on the orifice diameter (d_{o}), and can be calculated using equation 3.1 [93, 94].

$$Q_{\mathrm{V,min}} = (0.433 d_{\mathrm{o}})^2 \cdot \pi \cdot \sqrt{\frac{8\sigma_{\mathrm{f}}}{0.866 d_{\mathrm{o}} \cdot \rho_{\mathrm{f}}}} \tag{3.1}$$

Once a stable jet is established with a volume flow rate Q_{V} ($Q_{\mathrm{V}} \geq Q_{\mathrm{V,min}}$), an oscillating frequency (f) can be applied to the orifice which causes the liquid jet to break-up into droplets (Figure 3.1). As during each perturbation a droplet is formed, the volume of a single droplet (V_{d}) can be calculated as:

$$V_{\mathrm{d}} = \frac{Q_{\mathrm{V}}}{f} \tag{3.2}$$

However, the formation of droplets with constant volumes only occurs when the perturbation of the liquid jet occurs within a given interval. Schneider and Hendricks [95] determined an empirical range in which the jet perturbation results into the formation of monodisperse droplets, where the required perturbation is given by the wavelength λ, which depends on the volume flow rate (Q_{V}), oscillating frequency (f) and orifice diameter (d_{o}) [93, 95]:

$$\lambda = \frac{Q_{\mathrm{V}}}{f\pi(0.433 d_{\mathrm{o}})^2} \tag{3.3}$$

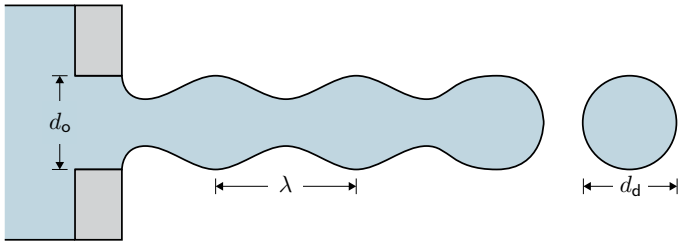

Figure 3.1: Schematic overview of the VOAG, where a solution is forced through an orifice with diameter d_o and the liquid jet is disturbed with a wavelength λ, resulting in the formation of monodisperse droplets with diameter d_d.

If the wavelength lies within the range of $3.03 d_o \leq \lambda \leq 6.06 d_o$, monodisperse droplets are formed with a constant droplet volume.

As the droplets can be assumed to consist of the same composition as the liquid feed, the elemental concentration of M within a single droplets ($c(M)_d$) is similar to the elemental concentration in the liquid feed ($c(M)_f$). Multiplication of the elemental concentration with the droplet volume (V_d) therefore results in the total elemental amount contained within a single droplet ($m(M)_d$). However, as the elemental concentration of the liquid feed is typically known as weight fraction ($w(M)_f$), the droplet volume should be corrected for the liquid feed density (ρ_f), resulting in equation 3.4.

$$m(M)_d = \frac{Q_V}{f} \cdot w(M)_f \cdot \rho_f \tag{3.4}$$

3.2 Particle Setup

Within this work, a commercially available vibrating orifice aerosol generator (Model 3450, TSI Inc., USA) was installed inside a fume-hood located in the controlled area, which allows the generation of uranium containing aerosols. The aerosol generator is placed upside down to decrease the gravitational loss of droplets. Two separate streams of compressed air are introduced into the VOAG to disperse ($0.8\,l\,min^{-1}$) and dilute ($18.2\,l\,min^{-1}$) the generated aerosol droplets. The air is filtered using a HEPA filter and both flow rates are controlled using mass flow controllers (Brooks Instrument GmbH, Germany). After passing a drying column, in which the volatile solvent partially evaporates, the droplet-bearing stream is passed through a virtual impactor, in which the flow rate is reduced to $5\,l\,min^{-1}$ with minimal loss of droplets/particles.

The concentrated particle-bearing stream is passed through a 200 mm long aerosol heater (Pressurized air heater, Dekati Ltd., Finland), which provides closed-loop control to ensure reproducible conditions and can achieve a maximal temperature of 600 °C. After the aerosol heater, the particle-bearing flow is passed through a 500 mm long air-cooled stretch. $1\,l\,min^{-1}$

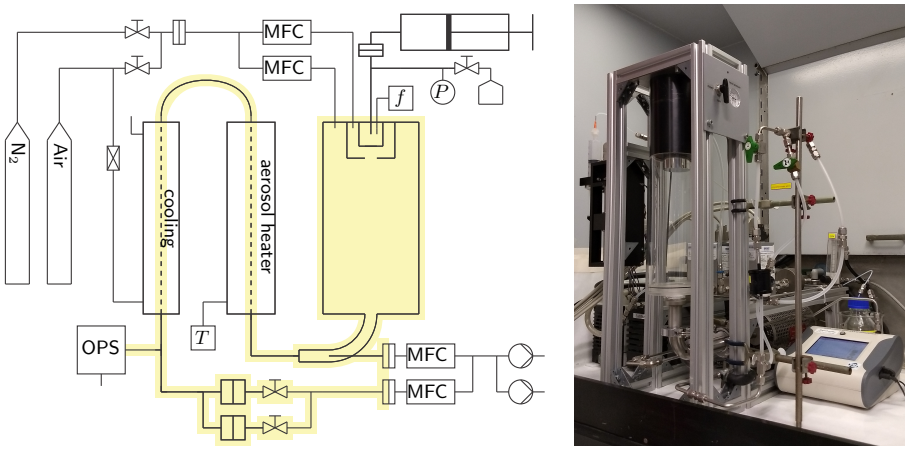

(a) Schematic **(b)** Photograph

Figure 3.2: Schematic layout of particle production system. The yellow-colored regions indicate the particle bearing flows. OPS: Optical Particle Sizer; MFC: Mass Flow Controller.

of the cooled particle-bearing flow is diverted into an optical particle sizer (Model 3330, TSI Inc., USA), which provides online information regarding the particle count and particle size distribution. The remaining $4\,\mathrm{l\,min^{-1}}$ particle-bearing flow is passed through a single-stage inertial impactor [96], in which the particles are deposited onto solid substrates with a maximal diameter of 25.4 mm. Typically, glass-like carbon disks, silicon wafers or quartz disks were used for particle collection. To ensure continuous flows throughout the system, pumps are installed upstream, where the outgoing flow rates are controlled using mass flow controllers. A schematic overview of the system as well as a photograph of the system are shown in Figure 3.2.

3.3 Liquid Feed Preparation

During regular production of particles, a liquid feed consisting of uranyl nitrate dissolved in a water/ethanol mixture was used. Uranyl nitrate solutions were first diluted with ultra-pure water ($18.2\,\mathrm{M\Omega\,cm}$, Elga PURELAB Ultra, ELGA LabWater, Germany) to a uranium content around $180\,\mathrm{\mu g\,g^{-1}}$, after which the solution was diluted with ethanol (Ethanol absolute for analysis EMSURE, Merck KGaA, Germany) to a water to ethanol volume ratio of 1. The addition of ethanol accelerates the droplet drying process and improves the morphological properties of the obtained particles. Ethanol was used instead of 2-propanol, which is advised in the operation manual [97] and was used by Erdmann et al. [74], to prevent reduction and eventually precipitation of uranium [98].

The prepared solution, with a uranium content around $100\,\mu g\,g^{-1}$ and a density around $894\,kg\,m^{-3}$ ($89\,\mu g\,ml^{-1}$), was transferred into a syringe (60 ml) and connected to the system. The syringe pump was set to a speed of $4.2\,\mu m\,s^{-1}$, which corresponds to a volume flow rate around $2.59\,\mu l\,s^{-1}$ (described in more detail in section 5.2.2). The solution was forced through a stainless-steel disk with an orifice of 20 µm. To prevent excessive corrosion of the stainless-steel disks by the uranyl nitrate solutions, the disks were coated with gold. Aerosols were generated with an oscillating frequency around 69 kHz. Based on equation 3.2 and equation 3.4, the produced droplets are expected to have a diameter and a uranium content of 40 µm and 3.4 pg, respectively.

The uranyl nitrate solutions were prepared from different certified reference materials with certified uranium isotopic compositions. Within this work, CRMs consisting of uranyl nitrate ($UO_2(NO_3)_2$), uranium hexafluoride (UF_6) and triuranium octoxide (U_3O_8) were used. To convert the UF_6 and U_3O_8 into uranyl nitrate, the UF_6 and U_3O_8 were hydrolyzed and dissolved in concentrated nitric acid, respectively. The obtained uranyl nitrate solutions were dried at 90 °C to remove all excess nitric acid after which the obtained uranyl nitrate hexahydrate was dissolved in dilute nitric acid to obtain uranyl nitrate solutions with a nitrate to uranium ratio ($n(NO_3)/n(U)$) around 10. All dilutions were performed gravimetrically and volumetrically, from which the solution density can be derived. The uranium content was determined by Q-ICP-MS (PerkinElmer/SCIEX Elan 6100 DRC, PerkinElmer Inc., USA) analysis. The nitrate concentration was estimated using a UV/VIS test kit (LCK339, Hach Lange GmbH, Germany) and the pH (WTW inoLab 7310, Xylem Analytics, Germany) of the produced solutions was measured for verification. All processing steps were performed under controlled conditions to minimize the risk of cross-contaminations.

In addition to the uranyl nitrate solutions, uranyl chloride and uranyl acetate solutions were prepared by dissolution of uranium trioxide in concentrated hydrochloric acid (Bernd Kraft, Germany) and acetic acid (Merck KGaA, Germany), respectively.

$$UO_3(s) + 2\,HCl(aq) \longrightarrow UO_2Cl_2(aq) + H_2O(l)$$
$$UO_3(s) + 2\,CH_3COOH(aq) \longrightarrow UO_2(CH_3COO)_2(aq) + H_2O(l)$$

Uranium trioxide was prepared by thermal decomposition of dried uranyl nitrate at 500 °C. The dissolution in the respective acids was repeated three times to ensure complete conversion, after which the obtained solutions were dried at 90 °C. The obtained uranyl acetate crystals were measured by XRD (D8 Advance, Bruker Co., USA) whereas uranyl chloride was measured by Raman spectroscopy (LabRam HR, Horiba Ltd., Japan) to verify the produced compounds. The dried products were dissolved in water, after which the uranium concentration was determined by Q-ICP-MS.

3.4 Particle Characterization Techniques

3.4.1 Morphology Characterization

A Fei Quanta 200F (Fei Company, The Netherlands) scanning electron microscope (SEM) was used in this work to investigate the produced particles. The SEM is equipped with a backscatter-electron detector (BSED), a secondary electron (SE) detector and an energy-dispersive X-ray spectrometer (EDX). The SEM is capable of measuring samples in low-vacuum mode (typically 60 Pa), due to which particles deposited onto either silicon wafers or glass-like carbon disks could be analyzed as obtained without applying an additional conductive layer.

Typical SEM studies were performed using the BSED detector, as this detector proved to provide highest contrast, and with acceleration voltages of 10 kV or 20 kV, which provide higher spatial resolution and improved EDX signal intensities, respectively.

To investigate a large number of particles in an automated manner, a particle analysis tool of EDAX Genesis was used. During such a particle analysis, micrographs were collected using the BSED detector over a given area of the sample. The collected micrographs are processed based on a gray-value threshold, clusters of pixels exceeding the threshold intensity are identified as particles. For each identified particle, basic morphological properties, such as the particle diameter and aspect ratio, are extracted. The automated processing of the collected micrographs to extract basic morphological properties of particles is exemplarily shown in Figure 3.3. As the determination of the particle diameter strongly depends on the selection of the particle edge, which is often slightly diffuse within the collected micrographs, the accurate determination of the particle diameter is a complex process. Also, as no suitable calibration standards were available, all diameters given in this work are informative values only. In addition to the morphological properties, EDX spot measurements were performed on each identified particle, which provides information regarding the chemical composition of the identified particle.

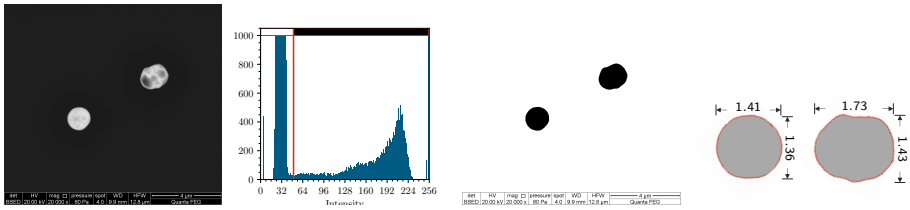

(a) Original **(b)** Histogram **(c)** Binary **(d)** Analyzed

Figure 3.3: Processing of collected SEM micrographs to extract basic morphological properties of microparticles.

To enhance the data processing, the collected micrographs can be post-processed using ImageJ [99, 100], where a gray-value threshold is selected in a similar fashion compared to the particle analysis using the EDAX Genesis software. However, by using ImageJ, the gray-value threshold can be selected in a more robust manner and more detailed morphology data can be extracted, such as the circularity of the particles.

The determined properties of a large number of particles allows to estimate the particle size distribution of the investigated particle population. Figure 3.4a shows a compilation of collected SEM micrographs of 300 randomly selected particles belonging to a single particle population. For each particle, the maximum and minimum diameter was determined using ImageJ, from which the mean particle diameter was calculated by taking the average of the maximum and minimum diameter. Figure 3.4b shows the empirical cumulative distribution function (E-CDF) of the mean particle diameter whereas Figure 3.4c displays the histogram. Both graphs indicate that the particle diameter is normally distributed and a Gaussian distribution function was fitted through the data by a least-square approach, which provides the mean particle size ($\bar{d}_\mathrm{p} = 1.259\,\mu\mathrm{m}$) and standard deviation ($s(d_\mathrm{p}) = 0.027\,\mu\mathrm{m}$) of the investigated particle

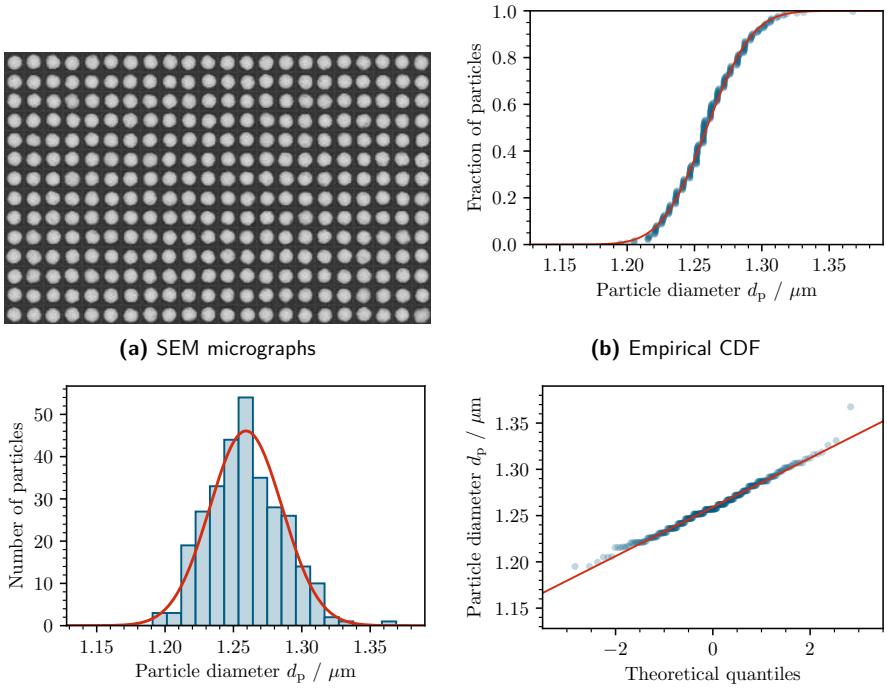

(a) SEM micrographs **(b)** Empirical CDF

(c) Histogram **(d)** Q-Q plot

Figure 3.4: Determination of the particle size distribution of 300 randomly selected particles identified on a single sample.

population. The validity of fitting a Gaussian function through the data was demonstrated by preparing a quantile-quantile (Q-Q) plot (Figure 3.4d), where the data shows a linear dependence. It should, however, be noted that the particle size strongly depends on the selection of the gray-value threshold and all given particle sizes in this work are estimates only and have not been calibrated/validated.

The spread of the particle size is often used to classify a particle population to consist of monodisperse or polydisperse particles. Although no official definition exist, NIST provided a practical guide [101] which defines a monodisperse particle population as:

> **Monodisperse** [...] a particle distribution may be considered monodisperse if at least 90 % of the distribution lies within 5 % of the median size [101]

If a sample contains a single particle population where the median particle diameter ($\tilde{d}_\mathrm{p}$) is equal to the mean particle diameter ($\bar{d}_\mathrm{p}$), the monodispersity of the population could be given based on the standard deviation of the particle distribution ($s(d_\mathrm{p})$), i.e. a particle population is considered to be monodisperse if $1.645 s(d_\mathrm{p})/\bar{d}_\mathrm{p} \leq 0.05$ [102]. Such assumption is, however, only valid if a sample consists of a single particle population. Additional particle populations, such as broken fragments, would overestimate the monodispersity of the distribution when only considering a single particle population.

The internal morphology of the particles was investigated by partial ablation of the particle material using a focused Ga^+ ion beam (Zeiss NVision 40 Cross Beam workstation, Carl Zeiss AG, Germany). Prior to ablation, the samples were coated with a conductive and protective carbon layer, deposited by electron and ion beam induced deposition. Selected particles were milled using a 40 keV Ga^+ ion beam with a current of 40 pA. Simultaneous recording of SEM micrographs using a build-in SE detector allows the recording of the ablation process. The recorded micrographs can be used to produce three-dimensional reconstructions of the ablated particles.

3.4.2 Synchrotron μ-X-Ray Studies

Synchrotron X-ray studies were performed at the microXAS beamline of the Swiss Light Source (PSI, Villigen, Switzerland). For the μ-X-ray studies, particles were collected on polyimide foil coated with vacuum grease (Apiezon L, M&I Materials Ltd., U.K.) to prevent loss of particles. To enhance the stability of the foil during particle collection, the foil was attached onto a quartz disk and transferred onto the required sample holder prior to the measurement.

μ-X-ray diffraction measurements were performed using a 17.2 keV (λ = 72.1 pm) X-ray beam focused to a spot size of 4.0 by 1.5 μm. Diffraction patterns were collected using a two-dimensional X-ray detector (marCCD 225, Rayonix, L.L.C., USA; formerly Mar USA Inc.) with a resolution of 3072 by 3072 pixels and a pixel size of 72 μm. Diffraction patterns were collected by scanning the focused beam over an area of 250 by 250 μm in steps of 4 μm. During each step, a XRD pattern was collected, resulting in the collection of 3969 patterns.

Simultaneous X-ray fluorescence spectra were recorded using a scintillator detector, which allow the spatial correlation of measured diffraction patterns with the chemical composition. In order to examine the data, all collected patterns were superimposed and an azimuthal integration was performed to yield diffractograms. The collected diffractograms were used for phase identification by comparison with reference patterns from ICDD PDF-2 database [103]. The lattice parameters of the identified phases were estimated by iteratively reweighted least squares to obtain the maximum likelihood estimators for the lattice constants.

μ-XANES measurements were performed by scanning over the uranium L_{III} edge using a diffuse 300 by 300 μm photon beam, which was used to increase the measurement quality of the collected spectra. The absorption spectra were collected in fluorescence mode and during each measurement ten spectra were collected. Reference spectra were collected of β-UO_3, U_3O_8 and UO_2 powders, which were verified by μ-XRD analysis prior to μ-XANES measurement.

3.4.3 μ-Raman Measurements

μ-Raman measurements were performed at CEA/DAM-Île-de-France (Arpajon, France) using a Renishaw "inVia" spectrometer (Wotton-Under-Edge, UK). Measurements were performed on particles deposited onto uncoated silicon wafers using a 514 nm laser. The laser was focused to a spot size around 0.6 μm, alignment of the laser onto particles was performed using an optical light microscope. To prevent weathering of the particles under the laser [85], the laser beam energy was reduced to approximately 1 % of full power, which is estimated to correspond to a power of 0.25 mW. Measurements were performed in confocal mode and a typical measurement consisted of five repetitions of 30 seconds or 180 seconds each. For each analyzed sample, at least twelve randomly selected particles were measured.

3.4.4 Mass Spectrometry

Mass spectrometric analyses of dissolved samples was performed using an inductively coupled plasma quadruple mass spectrometer (PerkinElmer/SCIEX Elan 6100 DRC, PerkinElmer Inc., USA). Samples were diluted in 156 mmol l^{-1} nitric acid, prepared by dilution of concentrated nitric acid (65 %, Suprapur, Merck KGaA, Germany) in ultra-pure water (18.2 MΩ cm, Elga PURELAB Ultra, ELGA LabWater, Germany). Mass fractionation correction factors were determined by measurement of a depleted and low-enriched uranium CRM and external calibration was performed using calibration standards prepared from a gravimetrically diluted CRM with a certified natural uranium isotopic composition and uranium content.

4 Results and Discussion

4.1 Process Characterization

Various studies have focused on the production of monodisperse uranium oxide microparticles by spray-pyrolysis of a uranium aerosol [64, 67, 68, 73–76, 78, 104]. However, a thorough search of the literature yielded no studies which investigated the particle formation process in detail, although extensive investigations for different systems [61–63, 105–107] have shown to be of importance towards optimization of the particle production method. Such optimization would result in a particle production process which can be controlled in a more reliable way and could lead to an improvement of various particle properties, such as the particle size distribution and density. During the entire particle production process, the thermal treatment is considered to be of critical importance, as during the thermal treatment both the evaporation/precipitation and the thermolysis stage of the particle formation process occurs (section 2.2), both of which affect the final particle morphology and chemical composition. In order to investigate the influence of these particle formation stages, the thermal decomposition of micrometer-sized droplets consisting of uranyl chloride, uranyl nitrate and uranyl acetate was investigated. Various particle formation stages were probed by investigating the particle morphology and the elemental composition of particles at different heat treatment temperatures. The systematic investigation of three different chemical systems provide insight into particle formation process and demonstrates that the particle production can be described in a consistent way.

4.1.1 Particle Formation from Uranyl Chloride

An aerosol was produced from a uranyl chloride solution using the setup described in section 3.2. The aerosol was guided through an aerosol heater where the aerosol heater temperature was increased in a step-wise fashion from 100 °C to 600 °C with steps of 100 °C. During each step, particles were collected on new silicon wafers (10 by 10 mm, Ted Pella Inc., USA) which were subsequently analyzed by SEM/EDX. Figure 4.1 shows one of the collected SEM (BSED) micrographs of the obtained particles and the corresponding EDX spectra. The particles can be identified easily in the micrograph based on the contrast provided by the uranium. The two particles do, however, show a different morphology; particle A has a spherical shape and a rather homogeneous density throughout the particle whereas particle B has an irregular shape and spots with lower intensity, indicating such spots contain only a little amount of uranium, i.e. the particle has a heterogeneous density.

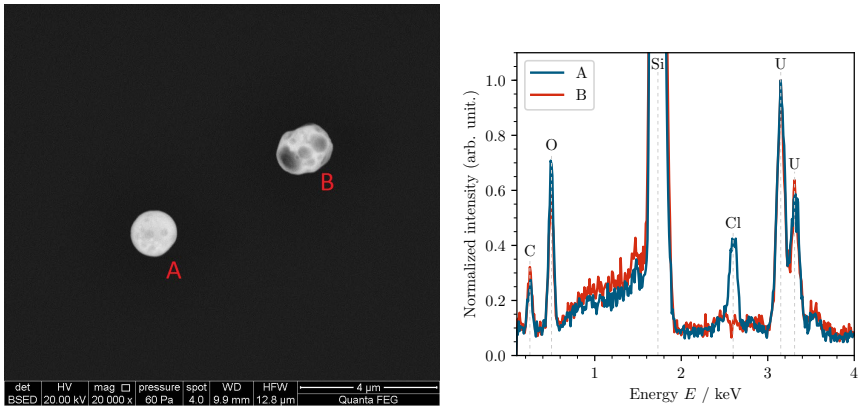

(a) SEM micrograph **(b)** EDX spectra

Figure 4.1: Collected SEM/BSED micrograph (a) and EDX spectra (b) of microparticles produced from uranyl chloride with a treatment temperature of 400 °C. The EDX spectra were collected at the center of the corresponding particles.

The corresponding EDX spectra, shown in Figure 4.1b, provide information on the chemical composition of the particles. Although the spectra were collected at the center of the particles, minor movements of the investigated particles due to charging effects are commonly observed, which does not allow the direct comparison of the collected EDX spectra. In order to compare the relative intensities, both spectra were normalized to the integrated intensity of the measured uranium lines, between 3.0 and 3.7 keV. The interpretation of the spectra is also complicated by the small size of the microparticles; both a 10 keV and 20 keV electron beam penetrate the particle and reaches the underlying substrate, which consists of silicon. This results in the very intense peak at an energy of 1.75 keV (Si K_α). Apart from the peak due to the silicon substrate, a few more peaks can be identified. The three peaks at 3.18 keV, 3.34 keV and 3.5 keV are attributed to uranium (M_α) and confirm that the investigated particles contain uranium. Two peaks can be observed in the lower energy range, where the peak at 0.29 keV is tentatively assigned to carbon (K_α) and the peak at 0.52 keV to oxygen (K_α). The oxygen is expected to stem from the uranium particles; both uranyl chloride (UO_2Cl_2) and uranium oxide (UO_3) contain oxygen. The carbon is, however, rather unexpected. Although the presence of carbon could stem from the decomposition of ethanol, the peak at 0.29 keV is likely caused by the uranium, as all investigated uranium samples contain this line, including pure U_3O_8. At 2.64 keV an additional peak is observed, which is only present in the collected spectrum for particle A. This peak is assigned to chloride (K_α) and demonstrates the suitability of EDX measurements to follow the chemical decomposition; particle A consists of uranyl chloride whereas particle B is decomposed and consists of uranium oxide.

In addition to the micrographs collected at a high magnification (20 000×) as shown in Figure 4.1a, a large number of micrographs were collected using an automated particle search procedure. A region of 3.41 by 2.67 mm was scanned at a lower magnification (2500×) and the collected micrographs were automatically processed to identify particles. For each investigated temperature, a separate scan was performed, Figure 4.2 shows a select number of particles found during these analyses. Based on the collected micrographs, three distinct types of particles can be observed; at low temperatures ($\leq$ 300 °C) large spherical objects were observed. EDX measurements show that the objects contain both uranium and chloride, from which can be concluded that these particles consist of uranyl chloride. Upon increasing the treatment temperature, an increasing amount of small particles was obtained. The small particles exhibit a higher BSED intensity compared to the large objects, indicating that the density of such particles is higher compared to the large objects. EDX measurements show that the dense particles still consist of uranyl chloride, based on which can be concluded that the large, low density objects are uranyl chloride droplets which have not yet fully precipitated whereas the dense particles are fully dried. The results show that the evaporation/precipitation proceeds most likely instantaneous (section 2.2.1), as no partially dried particles were observed, which would be expected in the case of progressive precipitation.

The third type of particles observed still exhibits a high density, but the density appears to be heterogeneous throughout the particles and the particles have a lower degree of sphericity. One such particles was observed in Figure 4.1 (particle B) and EDX measurements show the absence of chloride, from which can be concluded that the particles consist of uranium oxide and were decomposed. The irregular shape of the particles act as indicator that, during decomposition, gaseous products were released which remained trapped within the particle. This is an indication that the particles undergo melting before decomposition, as during the melting phase the porosity of the surface decreases, preventing the gaseous decomposition

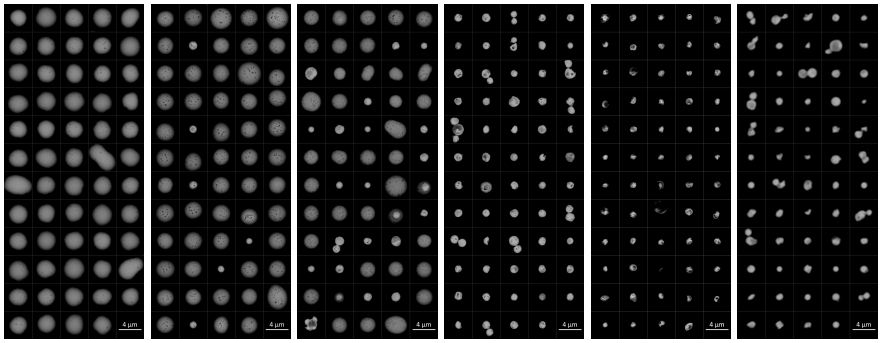

(a) 100 °C **(b)** 200 °C **(c)** 300 °C **(d)** 400 °C **(e)** 500 °C **(f)** 600 °C

Figure 4.2: Compilation of SEM/BSED micrographs of particles produced from uranyl chloride at different treatment temperatures.

products to diffuse out of the particle, which causes the swelling of particles and results in the irregular shape and heterogeneous density.

To investigate the internal particle morphology, a particle treated at 500 °C was investigated by FIB/SEM. Figure 4.3 shows one of the micrographs collected after ablation of half a particle; the micrographs show that the particle consists of a dense shell with a hollow core, as was expected based on the previously investigated SEM micrographs.

To obtain a better insight at the actual temperatures during which each transformation occurs, the obtained SEM and EDX data from the automated particle analyses scans was further analyzed. For each observed particle the mean diameter was calculated and the uranium and chloride intensity measured by EDX were integrated. The uranium to chloride ratio was calculated for each particle based on the integrated EDX intensities. To prevent division by zero for particles free of chloride, net intensities were used and no background subtraction was applied. The calculated intensity ratio is plotted against the determined mean particle diameter in Figure 4.4, where each point indicates an individual particle and the color of the points correspond to the temperature of the aerosol heater. The obtained plot depict the previously described transformations; at first large droplets were obtained. Upon drying, the particle diameter decreases while the uranium to chloride ratio remains constant. During the next stage the precursor particles are decomposed into the uranium oxide particles, increasing the uranium to chloride ratio while the particle diameter remains constant. A minor increase of the diameter was observed at elevated temperatures, which is likely caused by the agglomeration of particles. Using Figure 4.4, particles can be classified into three groups: (I) uranyl chloride droplets, (II) uranyl chloride particles and (III) uranium oxide particles. The various groups are indicated in Figure 4.4 and for each temperature, the total number of particles within each group is counted and shown graphically in Figure 4.5.

The findings from the SEM/EDX studies of microparticles produced from uranyl chloride with different treatment temperatures allow for qualitative comparison of the obtained results

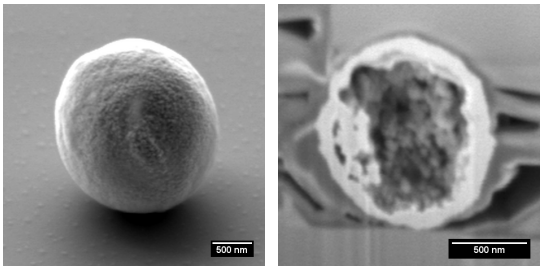

(a) Initial **(b)** Cross-section

Figure 4.3: FIB/SEM investigation of microparticles produced from uranyl chloride treated at 500 °C. Micrographs acquired in collaboration with Dr. M. Klinkenberg (FZJ/IEK-6).

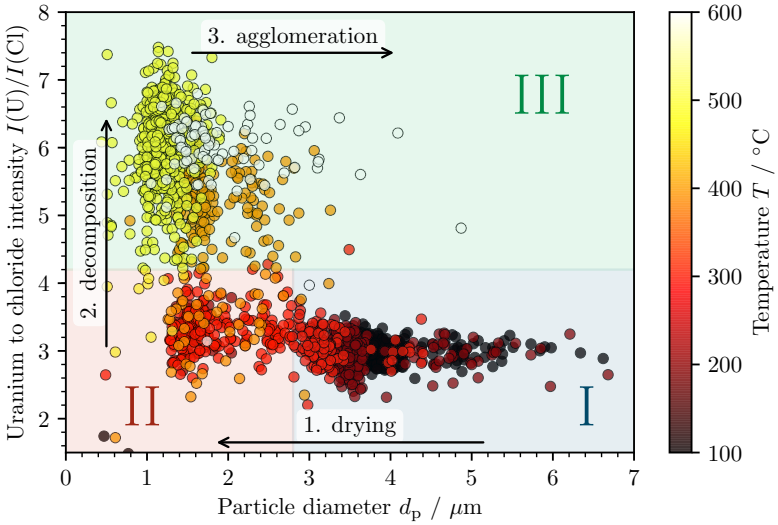

Figure 4.4: Particle properties of particles produced from uranyl chloride. (I) Uranyl chloride droplets; (II) Uranyl chloride particles; (III) Uranium oxide particles.

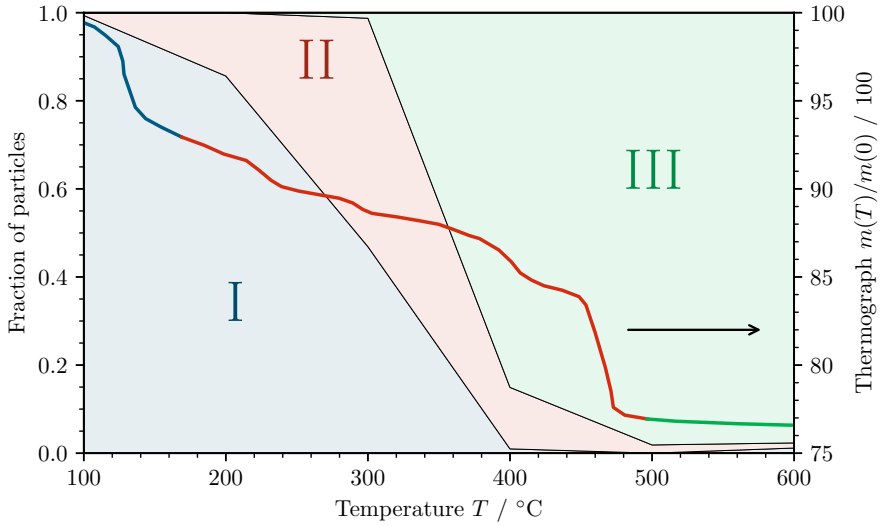

Figure 4.5: Fraction of particle classes found for different treatment temperatures. The line is the thermograph for the decomposition of uranyl chloride reported by Sato et al. [60].

with the results reported by Sato et al. [60], who investigated the thermal decomposition of hydrated uranyl chloride powders using thermogravimetric analysis (TGA), X-ray diffraction and infrared spectroscopy. In the work of Sato et al. [60], hydrated uranyl chloride was measured up to 175 °C, which dehydrates into anhydrous uranyl chloride around 175 °C, [60]

$$UO_2Cl_2 \cdot xH_2O \xrightarrow[\text{dehydration}]{175\,^\circ\text{C}} UO_2Cl_2$$

The dehydrated uranyl chloride then decomposes into amorphous, superstoichiometric UO_{3+x} in two distinct steps, where each step is accompanied by the release of chloride. The first step proceeds between 220 °C and 430 °C whereas the dechloration is completed at a temperature of 490 °C. The dechloration reaction can be written as: [60]

$$UO_2Cl_2 \xrightarrow[\text{dechloration(1)}]{220\text{-}430\,^\circ\text{C}} [UO_2Cl] \xrightarrow[\text{dechloration(2)}]{490\,^\circ\text{C}} UO_{3+x}$$

After decomposition, amorphous UO_3 was obtained, which recrystallizes at 520 °C to the orthorhombic α-UO_3 phase. This crystalline phase then decomposes to U_3O_8 ($UO_{2.67}$) at a temperature of 650 °C, which temperature is beyond the scope of the current investigations.

$$UO_{3+x} \xrightarrow[\text{crystallization}]{520\,^\circ\text{C}} \alpha{-}UO_3 \xrightarrow[\text{reduction}]{650\,^\circ\text{C}} UO_{2.67}$$

The produced microparticles show a similar behavior as described by Sato et al. [60]. The uranyl chloride droplets (I) correspond to the dissolved uranyl chloride and the hydrated uranyl chloride ($UO_2Cl_2 \cdot xH_2O$). Although Sato et al. [60] observed two distinct decomposition stages, the EDX data only allow for the identification of the overall decomposition from UO_2Cl_2 to UO_3, where the UO_2Cl_2 is observed in the uranyl chloride particles (II) and the uranium oxide particles (III) contains of either UO_{3+x} or α-UO_3, which can not be distinguished using the applied methods. The temperatures at which the various decomposition stages are observed differs, however, slightly from the reported temperatures. In general the particles appear to decompose at lower temperatures compared to the investigated powders, which might be caused by the high surface area of the particles. The expected particle formation pathway derived from the previously described investigations is shown graphically in Figure 4.6.

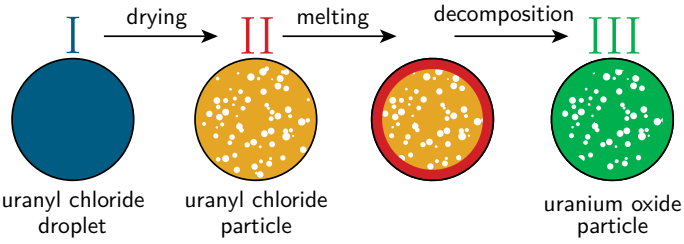

Figure 4.6: Particle formation from a uranyl chloride aerosol droplet.

4.1.2 Particle Formation from Uranyl Acetate

Similar SEM/EDX studies were performed using uranyl acetate as precursor. Uranyl acetate was selected due to the different product obtained after thermal decomposition; the decomposition of uranyl acetate leads to the formation of triuranium octoxide (U_3O_8) whereas uranyl chloride first leads to the formation of uranium trioxide. The decomposition reaction has been studied by various authors [55–59] and proceeds in two distinct steps. At first, the hydrated uranyl acetate is dehydrated, which occurs around 80 °C:

$$UO_2(CH_3COO)_2 \cdot x H_2O \xrightarrow[\text{dehydration}]{80\,^\circ\text{C}} UO_2(CH_3COO)_2$$

Upon a further increase of the temperature, typically around 300 °C, the uranyl acetate decomposes by removal of the two acetate groups, resulting in the formation of uranium dioxide:

$$UO_2(CH_3COO)_2 \xrightarrow[\text{decomposition}]{300\,^\circ\text{C}} UO_2$$

Uranium dioxide, which consists of pure tetravalent uranium, is unstable at elevated temperatures in an oxidizing atmosphere and, when heated in air, is rapidly oxidized to triuranium octoxide [33, 40]:

$$UO_2 + O_2 \xrightarrow[\text{oxidation}]{300\,^\circ\text{C}} UO_{2.67}$$

Investigation of the thermal decomposition of uranyl acetate by SEM/EDX studies is, however, complicated by the spectral interference of the carbon K_α line at 277 eV. As seen in Figure 4.1b, all EDX spectra of uranium compounds result in a line around 0.29 keV, which is expected to be a measurement artifact. Figure 4.7 shows the collected EDX spectra from particles produced using uranyl acetate solutions with different treatment temperatures. During the temperature increase from 100 °C to 300 °C, a strong reduction of the measured carbon and oxygen intensity was observed. This decrease is likely to represent the drying and possibly the decomposition reaction, although the EDX spectra do not allow to distinguish between these two reactions. A further increase of the treatment temperature to 400 °C and above does not significantly alter the EDX spectra.

The collected SEM micrographs of particles produced from uranyl acetate at different treatment temperatures (Figure 4.8) do, however, provide information on the particle formation process. Already at 100 °C spherical particles with a relative high BSED intensity were obtained, indicating that dried particles were formed. An increase of the temperatures to 200 °C only caused a minor decrease of the particle diameter, indicating some continuing evaporation. The continuing evaporation and decrease of the particle diameter indicates that the evaporation/precipitation stage of the particle formation process proceeds by the progressive precipitation with species diffusion model (section 2.2.1); upon evaporation of the solvent (water/ethanol), the solute (uranyl acetate) diffuses rapidly throughout the droplet and precipitates randomly throughout the droplet. With continuing evaporation and precipitation,

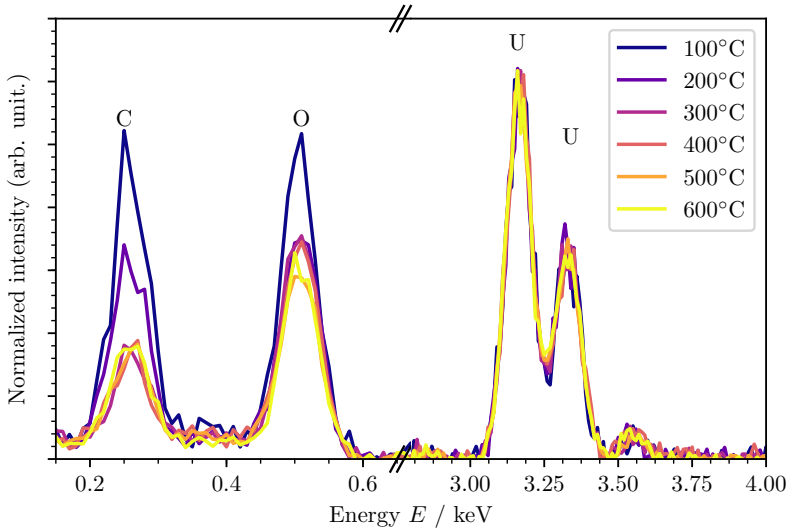

Figure 4.7: Collected EDX spectra of microparticles produced from uranyl acetate with different treatment temperatures. The spectra have been normalized to the measured uranium signal.

clusters of precipitated uranyl acetate form, while the droplet diameter continuously decreases, finally causing an agglomeration of the precipitated clusters, which forms the precursor particle. The increased sphericity of particles formed at 200 °C compared to 100 °C indicates that at 100 °C the precipitation is not completed and the impact of the partially precipitated droplets onto the substrate causes the deformation of the particles.

At 300 °C, the particle diameter decreases while an increase of the BSED intensity was observed, which indicates an increase of the particle density. This trend continues up to 400 °C and represents the thermal decomposition of the uranyl acetate precursor particles into uranium oxide particles.

A further increase of the treatment temperature to 500 °C and 600 °C shows the formation of particle agglomerates, where the number of agglomerated particles and total number of agglomerates seem to increase with increasing temperature. Although some agglomeration was observed for particles produced from uranyl chloride, the fraction of agglomerates is much higher for uranyl acetate. The agglomeration is most likely caused by the rapid oxidation of the formed uranium dioxide after decomposition, which involves a small weight gain (ca. 4 %) and expansion (ca. 36 %) of the particle. As the particle movement within the furnace increases with increasing temperature due to Brownian motion [63], the probability that two particles collide and coagulate during oxidation is increased with increasing temperature.

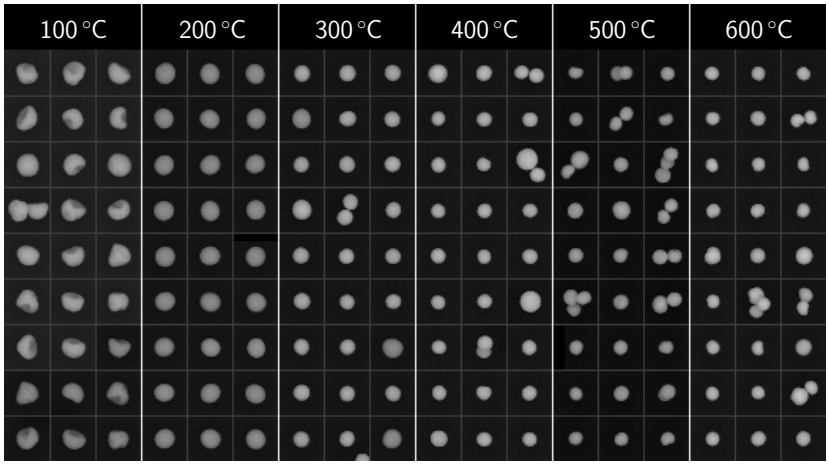

Figure 4.8: Compilation of collected SEM (BSED) micrographs of particles produced from uranyl acetate at different treatment temperatures.

The SEM micrographs show a high degree of homogeneity of the particle density and all particles exhibit a spherical shape. In order to investigate the internal morphology of the obtained particles, particles produced with a treatment temperature of 400 °C were milled using a FIB. The collected cross-sectional micrographs (Figure 4.9) show that the particles consist of a dense particle core, although some homogeneously distributed nanopores could be seen. Also, a mean density around 4.7 g cm^{-3} was estimated based on the determined particle diameter and calculated uranium content (equation 3.4). As the theoretical density of triuranium octoxide is 8.38 g cm^{-3} [72], the density of the produced particles is approximately 56 % of the theoretical density. This low density is an indicator that the particles contain a large number of pores which are not readily visible in the collected FIB/SEM micrographs.

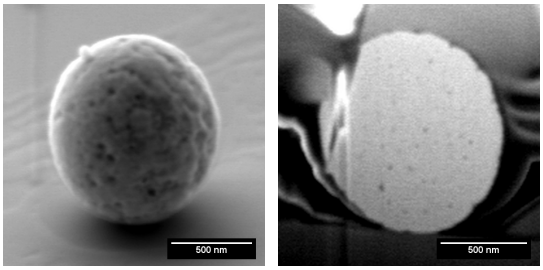

(a) Initial **(b)** Cross-section

Figure 4.9: FIB/SEM investigation of microparticles produced from uranyl acetate treated at 400 °C. Micrographs acquired in collaboration with Dr. M. Klinkenberg (FZJ/IEK-6).

Based on the SEM investigations, both particle formation and uranyl acetate decomposition stages could be followed. Already at 100 °C, hydrated uranyl acetate particles tend to form, although the formation of uranyl acetate particles continues up to a temperature of 200 °C. As the dehydration of uranyl acetate is observed at 80 °C, the formed particles are expected to consist of dehydrated uranyl acetate. An increase of the temperature from 200 °C to 300 °C causes the decomposition of the uranyl acetate into uranium dioxide followed by rapid oxidation to triuranium octoxide. The observed temperature at which the particles are decomposed is in good agreement with the decomposition temperature of 300 °C reported for powdered uranyl nitrate samples [46–51]. The presence of homogeneously distributed nanopores within the decomposed particles indicates that no significant melting occurs and the formed decomposition gasses can readily leave the particle. The final decomposition pathway is shown graphically in Figure 4.10.

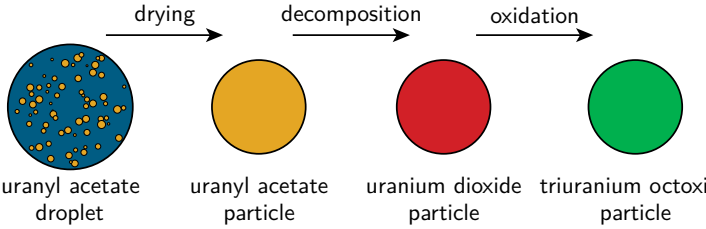

Figure 4.10: Schematic pathway of the particle formation from a uranyl acetate droplet to uranium oxide particle.

4.1.3 Particle Formation from Uranyl Nitrate

SEM/EDX investigations of the particle formation starting from uranyl nitrate solutions is complicated by the interference in the EDX spectra between carbon (277 eV), nitrogen (392 eV) and oxygen (525 eV). Even though, the various stages of the particle formation process could be identified using the collected SEM micrgraphs (Figure 4.11). At a treatment temperature of 100 °C, large spherical objects were obtained which are likely to be wet droplets, similar to the droplets observed at 100 °C when starting from uranyl chloride. An increase of the temperature to 200 °C results in the formation of dense particles, which are likely to consist of uranyl nitrate. Similar to the particle formation of uranyl chloride particles, the uranyl nitrate droplets seem to precipitate instantaneously (section 2.2.1) into the uranyl nitrate particles, forming porous precursor particles.

A temperature increase to 300 °C followed by 400 °C leads to a change of the particle morphology and density, indicating the decomposition of uranyl nitrate into uranium trioxide. The process appears to be continuous and the particle diameter decreases slightly up to a temperature of 500 °C. An increase of the temperature to 600 °C does, however, produce less uniform particles. Figure 4.12 shows the obtained particle size distribution of particles produced

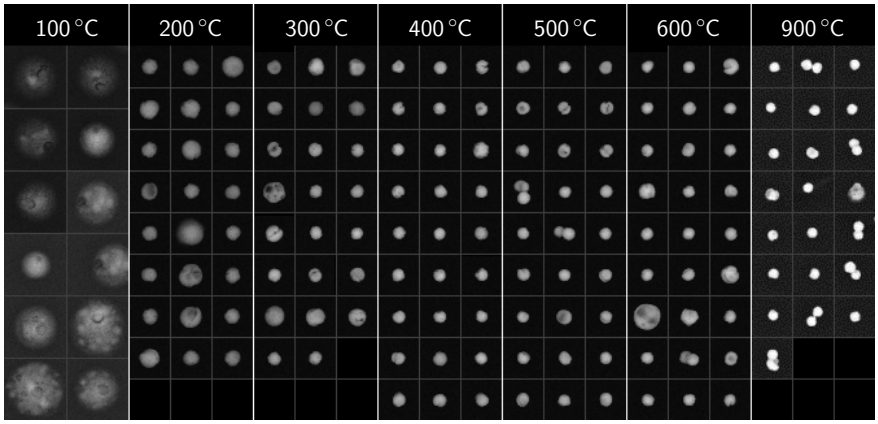

Figure 4.11: Collected SEM micrographs of particles produced from uranyl nitrate at different treatment temperatures.

at 500 °C and 600 °C. The particles were produced during the same production run without interruption of the liquid jet; particles were first produced at 500 °C after which the aerosol heater temperature was increased to 600 °C. The particle size distribution of particles produced at 600 °C does, however, show a second population of particles around 1.40 µm, whereas only very few such particles were found in the sample treated at 500 °C. Such a second population was previously observed by Erdmann et al. [74] and Ranebo et al. [73] and consists of particles containing double the amount of uranium compared to the main population. The diameter of particles containing n times the elemental amount (d_n) compared to particles with a diameter d can be calculated using equation 4.1.

$$d_n = d \cdot \sqrt[3]{n} \tag{4.1}$$

The second population, with a diameter of 1.40 µm, therefore consists of particles with double the amount of uranium ($n = 2$) compared to the main particle population with a mean diameter of 1.11 µm. The increased number of particles within the second population was previously attributed to the fusion of two aerosol droplets shortly after generation. The results of this work do, however, indicate that the coagulation occurs during the thermal decomposition stage. Such coagulation of two particles at elevated temperature is likely due to the increased Brownian motion of particles within the aerosol heater [63] accompanied by the melting of the precursor particle.

Although EDX analysis is complicated by spectral interference of nitrogen (392 eV) from carbon (277 eV) and oxygen (525 eV), the decomposition can be partially followed by the collected EDX spectra. Figure 4.13 shows a select number of EDX spectra collected for particles obtained at different treatment temperatures. The spectra show a strong decrease of the measured carbon, nitrogen and oxygen signal upon a temperature increase from 100 °C

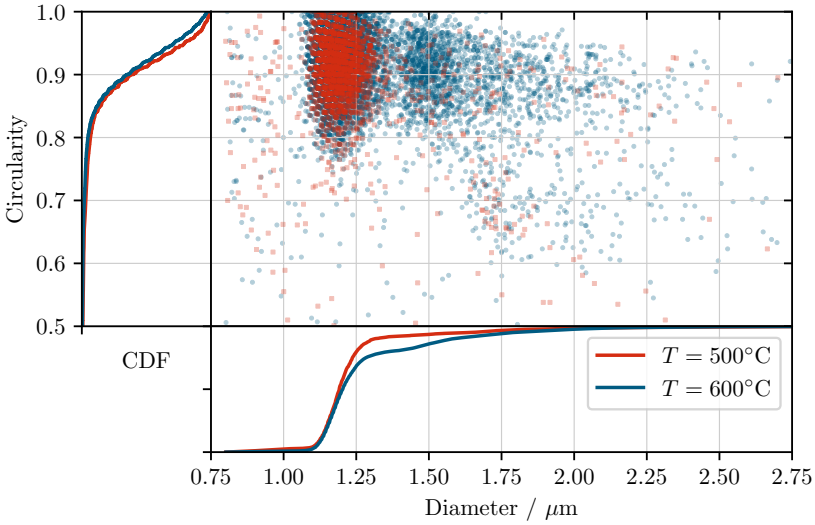

Figure 4.12: Measured particle size distribution and circularity (4π[area]/[perimeter]^2) of microparticles produced from uranyl nitrate with thermal treatments of 500 °C and 600 °C.

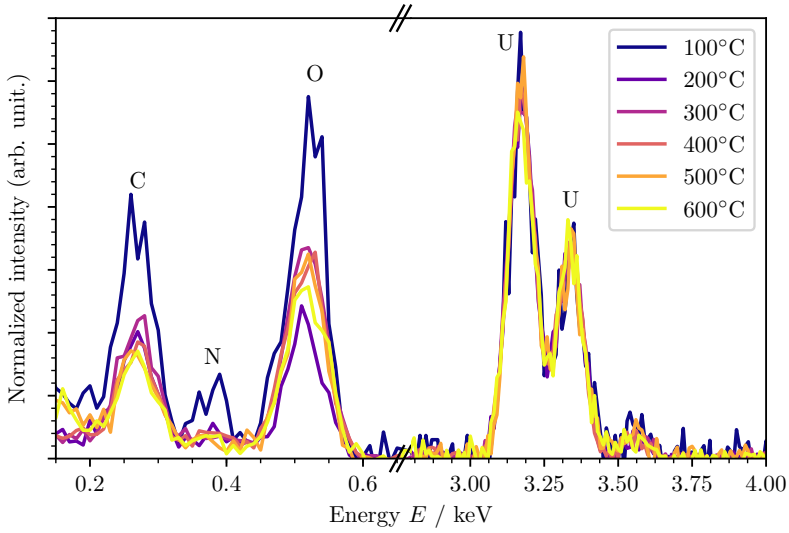

Figure 4.13: Collected EDX spectra of microparticles produced from uranyl nitrate with different treatment temperatures. The spectra have been normalized to the measured uranium signal.

to 200 °C. This reduction of oxygen and nitrogen is likely caused by the drying and therefore evaporation of nitric acid from the droplets. Due to the intense signals from carbon and oxygen, no more remaining nitrogen is observed and further decomposition could not be followed by the EDX spectra.

Particles were also produced from uranyl nitrate in an adjusted setup, where a second furnace was installed after the aerosol heater. The furnace, with a length of 1.20 m was set to a temperature of 900 °C while the aerosol heater was set to a temperature of 600 °C. Collected micrographs of the obtained particles are shown in Figure 4.11. To achieve a temperature of 900 °C, a second furnace was installed, due to which also the geometry of the particle production setup was changed. The obtained particles are more deformed and have a lower degree of monodispersity compared to particles produced at 500 °C and even 600 °C. These findings support the hypothesis that both melting and particle agglomeration occurs during the thermal treatment and also explains the increased degree of monodispersity of particles produced in this work compared to particles produced by Erdmann et al. [74] and Ranebo et al. [73], who treated the particles at a temperature of 800 °C.

Comparison with Literature. The thermal decomposition of uranyl nitrate powders has received considerable attention over the last decades [46–54]. However, inconsistent results were obtained and the decomposition pathway is not yet fully understood. Upon heating, the hydrated uranyl nitrate starts to dehydrate with up to six distinct stages, which is expected to be complete around 240 °C.

$$UO_2(NO_3)_2 \cdot x\,H_2O \xrightarrow[\text{dehydration}]{40\,^\circ\text{C-}240\,^\circ\text{C}} UO_2(NO_3)_2$$

The drying of droplets and formation of particles was observed between 100 °C and 200 °C, from which can be expected that the formed particles consist of partially dehydrated uranyl nitrate. However, traces of uranium trioxide, the first decomposition product, were found at temperatures as low as 176 °C [50]. The decomposition of uranyl nitrate also proceeds in a continuous manner between 220 °C and 340 °C and results in the formation of uranium trioxide. The rate at which the decomposition occurs does, however, affect the modification of the obtained UO_3. When heated rapidly and melting occurs during decomposition, monoclinic β-UO_3 is formed whereas with slow heating orthorhombic γ-UO_3 is formed [34, 35].

$$UO_2(NO_3)_2 \xrightarrow[\text{denitration}]{220\,^\circ\text{C-}340\,^\circ\text{C}} UO_3$$

The obtained modification of the UO_3 is of importance for the next stage of the decomposition, during which the UO_3 is partially reduced and decomposed into U_3O_8. The UO_3 decomposes into U_3O_8 at 560 °C and 695 °C for β-UO_3 and γ-UO_3, respectively (Figure 2.3). This reaction

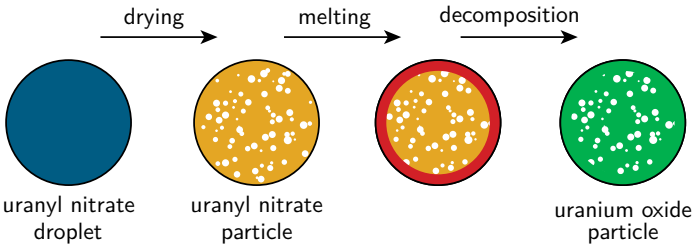

Figure 4.14: Schematic pathway of the particle formation from a uranyl nitrate droplet to uranium oxide particle.

is, however, beyond the temperature investigated in this work.

$$\beta\text{-}UO_3 \xrightarrow[\text{reduction}]{560\,^\circ C} UO_{2.67}$$
$$\gamma\text{-}UO_3 \xrightarrow[\text{reduction}]{695\,^\circ C} UO_{2.67}$$

The previous results can be used to derive the particle formation process from uranyl nitrate droplets to uranium oxide microparticles. The formed droplets are first dried and upon reaching saturation, hydrated uranyl nitrate particles are formed by instantaneous precipitation. After dehydration, the particles melt after which the uranyl nitrate decomposes to uranium oxide. Due to the melting of the precursor particle, densification of the surface occurs resulting in the formation of voids at the particle center due to produced decomposition gasses. The schematic overview of the particle formation process is shown in Figure 4.14.

FIB/SEM Investigation. In order to investigate the internal morphology of particles produced at 500 °C, FIB/SEM investigations were conducted using ten randomly selected particles. The obtained micrographs (Figure 4.15) showed that the obtained particles have a dense surface with a porous core, where the porosity increases towards the particle core. These results confirm that the particles undergo melting before decomposition, resulting in the dense surface layer. The particles are, however, not as hollow as the particles produced from uranyl chloride. Such a difference could be caused by the different polarity of the decomposition gasses. Where the decomposition of uranyl chloride leads to the formation of the strongly polar HCl, the decomposition of uranyl nitrate leads to formation of NO_2. As the formed uranium oxide also has a high polarity, the diffusion of HCl through the dense uranium oxide shell might be slower than the diffusion of NO_2, resulting in a lower internal pressure and the formation of voids provide sufficient volume for the decomposition gasses to accumulate.

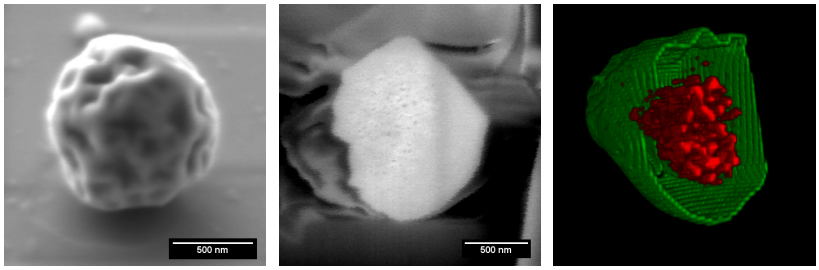

(a) Initial [108] **(b)** Cross-section [109] **(c)** 3d reconstruction

Figure 4.15: FIB/SEM investigation of microparticles produced from uranyl nitrate treated at 500 °C. Micrographs acquired in collaboration with Dr. M. Klinkenberg (FZJ/IEK-6).

Nitrate to Uranium Ratio. In order to investigate the effect of the formation of gaseous decomposition products onto the final particle morphology, particles were produced using uranyl nitrate solutions with different nitrate to uranium ratios, where the ratio $n(\mathrm{NO_3})/n(\mathrm{U})$ is hereafter given as R. At first, a stoichiometric uranyl nitrate solution ($R = 2$) was prepared by dissolution of uranyl nitrate hexahydrate in water. The nitrate content was then increased by the addition of nitric acid (65 % Suprapur, Merck Millipore, Germany).

Also, a sub-stoichiometric solution ($R \approx 1.3$) was prepared by dissolution of β-UO_3 in stoichiometric uranyl nitrate solution, as is the common method to produce acid deficient uranyl nitrate (ADUN) solutions [110–113]. The added β-UO_3 is dissolved consuming free protons, thereby increasing the uranium concentration, decreasing the free proton concentration while maintaining the nitrate concentration. The general dissolution reaction can be written as:

$$\mathrm{UO_3} + 2\,\mathrm{H^+} \rightleftharpoons \mathrm{UO_2^{2+}} + \mathrm{H_2O}$$

Where the free protons are available due to the hydrolysis of water by the uranyl:

$$p\mathrm{UO_2^{2+}} + q\mathrm{H_2O} \rightleftharpoons (\mathrm{UO_2})_p(\mathrm{OH})_q^{2p-q} + q\,\mathrm{H^+}$$

The produced, sub-stoichiometric uranyl nitrate solution can be written in a generalized way as $\mathrm{UO_2(NO_3)}_R\mathrm{(OH)}_{2-R}$, where R is the $n(\mathrm{NO_3})/n(\mathrm{U})$ ratio, which can be decreased down to 1.3. Such ADUN solutions are typically used to yield uranyl nitrate solutions with a high pH or with a very high uranium concentration (up to $3\,\mathrm{mol\,l^{-1}}$).

The prepared solutions were characterized with respect to the nitrate and uranium concentration by UV/VIS (LCK339, Hach Lange GmbH, Germany) and Q-ICP-MS (Elan 6100 DRC, PerkinElmer Inc., USA) measurements, respectively. pH measurements were performed as additional verification measure, where a clear decrease of the pH with increase of the nitrate concentration was observed. After preparation and characterization of the various solutions,

the solutions were used to produce microparticles, with the aerosol heater set to 500 °C. The particles were collected on silicon wafers which, in turn, were investigated using SEM (Figure 1, Appendix). The collected micrographs were post-processed using ImageJ [100] to obtain information on the particle morphology. For each particle, the circularity was calculated as:

$$[\text{circularity}] = \frac{4\pi[\text{area}]}{[\text{perimeter}]^2}$$

Which yields a circularity of 1 for a perfect sphere and decreases for more deformed circular shapes. A plot of the circularity against the mean particle diameter was prepared for each sample, the plot for particles produced from solutions with a NO_3/U ratio of 10 and 20 is shown exemplary in Figure 4.16, together with the empirical cumulative distribution function (E-CDF) of both the circularity (left side) and particle diameter (bottom). Similar plots for all other samples are placed in Figure 2 (Appendix).

Figure 4.16 shows that particles produced from uranyl nitrate solutions with a NO_3/U ratio of 10 have both a narrower particle size distribution and a higher degree of sphericity compared to particles produced from a solution with a NO_3/U ratio of 20. Such deformation is caused by the release of nitrous gasses during the decomposition of uranyl nitrate, where the total volume of gaseous release products is higher for the particles produced from a solution with a ratio of 20 then for particles produced from a solution with a ratio of 10. Although particles produced

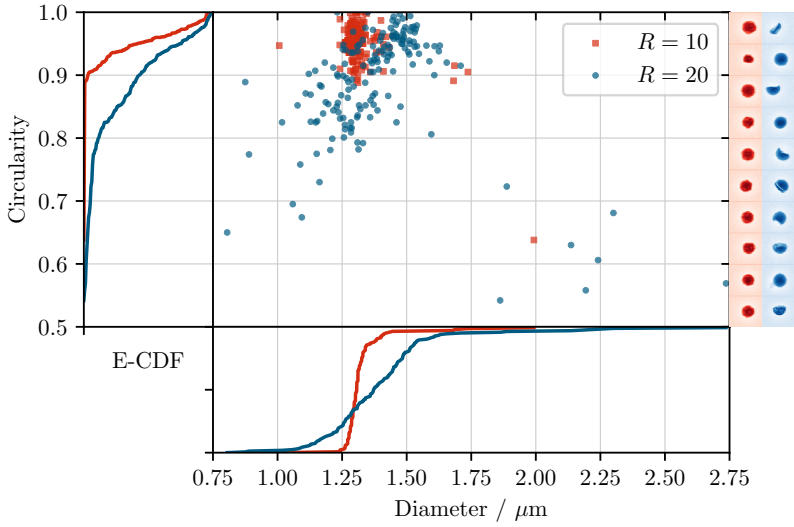

Figure 4.16: Empirical cumulative distribution function of the particle circularity ($4\pi[\text{area}]/[\text{perimeter}]^2$) and particle diameter of particles produced from uranyl nitrate solutions with different NO_3/U ratios (R).

from a solution with a ratio of 13 are only shown in Figure 2 (Appendix) and not in Figure 4.16 as the uranium concentration of the solution differs slightly, the sphericity seem to be lower than the particles produced from a solution with a ratio of 10. All particles produced from solutions with a ratio smaller than 10 appear to be similar with respect to the diameter and sphericity. From these results can be concluded that up to a ratio of 10 to 13, the formation of decomposition gasses can be compensated for by the diffusion of the gaseous decomposition products out of the particles.

At a ratio higher than 13 the formation of gaseous products exceeds the evacuation of such products, causing the deformation of the particles. An increase of the ratio to 85 causes an even stronger decrease of the particle circularity. However, in addition to deformed particles, a number of highly spherical but large particles ($d \approx 4\,\mu m$) were observed. One such particle was investigated by FIB/SEM, the collected micrographs are shown in Figure 4.17. The cross-section view of the milled particle shows that the particle is hollow. Such particles would result from the very large volume of NO_2 produced upon thermal decomposition. Where irregular particles with local voids were produced from solutions with a ratio of 20, such a large volume release results in the inflation of the particle.

Particle density. As the aerosol generator produces droplets with constant volumes, the final particle size could be adjusted by changing the uranium concentration of the liquid feed solution (equation 3.4, section 3.1). There are, however, a large number of effects which can affect the overall particle production process; within the enclosed system large particles are more affected by gravity whereas smaller particles tend to diffuse more strongly, both which could result in a strong decrease of the production efficiency. Also, precipitation of the solute during the drying stage might result in the formation of dispersed nanoclusters instead of microparticles when the solute concentration is very low. On the other hand, the structural integrity of large particles might cause problems, for example during collection.

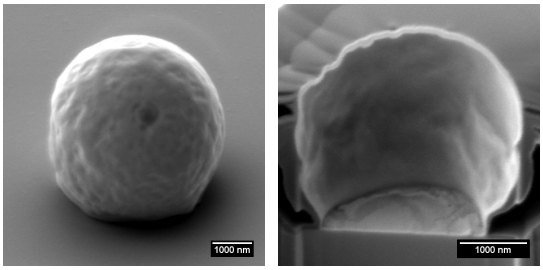

(a) Initial **(b)** Cross-section

Figure 4.17: FIB/SEM investigation of microparticles produced from uranyl nitrate solutions with a nitrate to uranium ratio of 85, treated at 500 °C. Micrographs acquired in collaboration with Dr. M. Klinkenberg (FZJ/IEK-6).

In order to investigate the range in which microparticles can be produced and estimate the mean particle density, microparticles were produced from uranyl nitrate solutions with uranium concentrations ranging from 54 µg g^{-1} to 221 µg g^{-1}. The particles were produced over a large number of productions runs with a total time-span of 687 days. The nitrate to uranium ratio was kept constant between 10 and 13 and a constant volume flow rate of 2.6 µl s^{-1} was applied. The oscillating frequency was adjusted within the range of 40 kHz to 70 kHz. The expected uranium content of a single particles was calculated as described in section 3.1. SEM micrographs were collected at either 2500× or 20 000× magnification of different 47 samples, resulting a total of 1293 particles. The collected micrographs were post-processed using image processing software (ImageJ [100]) to calculate the mean particle diameter. For each sample, the arithmetic mean was calculated based on all determined diameters and the standard deviation was used as uncertainty. This method is, however, likely to overestimate the actual spread of the particle size. The mean particle diameter is plotted against the calculated uranium content in Figure 4.18.

The figure shows a clear correlation between the measured particle diameter and calculated uranium mass. The obtained data allows for the estimation of the mean particle density, where a mean uranium density of 3.8(11) g cm^{-3} was determined. In order to compare the derived density with theoretical values, the chemical composition of the particle needs to be taken into account. The particle density (ρ_p) can be calculated from the elemental density of M ($\rho(M)_\mathrm{p}$)

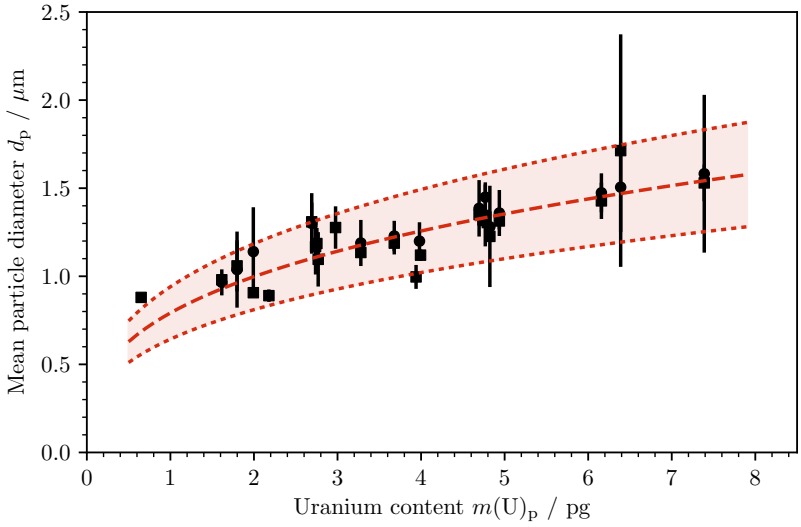

Figure 4.18: Particle size as function of uranium content for 1293 particles analyzed by SEM. The red line corresponds to an estimated density of 3.8 g cm^{-3}.

taking the weight fraction of M in the particle ($w(M)_\mathrm{p}$) into account (equation 4.2).

$$\rho_\mathrm{p} = \frac{\rho(M)_\mathrm{p}}{w(M)_\mathrm{p}} \tag{4.2}$$

When assuming particles to consist of UO_3 ($w(\mathrm{U}) = 832\,\mathrm{mg\,g^{-1}}$) or eventually U_3O_8 ($w(\mathrm{U}) = 848\,\mathrm{mg\,g^{-1}}$), 64 % and 54 % of the theoretical densities [72] were reached, respectively. Such low densities compared to pure material is commonly observed during bulk material production and is likely due to the porous structure of the particles. The results do, however, show that the used setup is capable of producing particles with consistent densities over a long period of time, even with varying various production settings, such as the oscillating frequency. Also, the estimated density is comparable with the density measured by Kraiem et al. [77], who analyzed multiple particles from two production batches by isotope dilution thermal ionization mass spectrometry (ID-TIMS), resulting in mean uranium densities of $3.8\,\mathrm{g\,cm^{-3}}$ and $4.7\,\mathrm{g\,cm^{-3}}$.

For particle produced from uranyl acetate, only a single sample was prepared, from which a mean density of $4.0\,\mathrm{g\,cm^{-3}}$ was derived. This density is also lower than the theoretical density of U_3O_8. As only a limited number of nanopores were observed in the cross-section micrographs obtained after FIB milling (Figure 4.9), the low density indicates the presence of a large number of very small nanopores which could not be discerned by SEM. Due to the irregular shape of particles produced from uranyl chloride, the particle volume can not be calculated based on the measured particle diameter, therefore it is not possible to derive a mean particle density.

4.2 Structural Investigation

4.2.1 Particles from Uranyl Nitrate

In order to characterize the produced microparticles with respect to the chemical composition and structure, μ-XRD measurements were performed of particles produced from uranyl nitrate treated at 500 °C. A select number of the collected diffraction patterns are shown in Figure 4 (Appendix). However, in order to examine all data, all collected patterns were superimposed (Figure 4.19a) and an azimuthal integration was performed to yield the diffractogram (Figure 4.19b). The superimposed pattern, as well as individual patterns, show a number of diffraction bands. In the case of μ-XRD, such bands indicate the presence of nanocrystalline domains within the particles. The obtained diffraction pattern were compared with patterns of known uranium containing compounds, which resulted in a close match with reference patterns of triuranium octoxide (U_3O_8). The presence of a U_3O_8 phase is rather unexpected as Hoekstra and Siegel [34] and Wheeler et al. [35] both measured the decomposition of UO_3 to U_3O_8 to occur at temperatures well in excess of 500 °C.

In order to verify the existence of a U_3O_8 phase, μ-XANES measurements were performed at the uranium L_{III} edge. U_3O_8 consists of a mixture of both pentavalent and hexavalent uranium [37], whereas UO_3 consists purely of hexavalent uranium [33]. Therefore, a shift of the white line can act as an indicator for the oxidation state of uranium. However, as described by various authors [91, 115, 116], the energy shift of the white line does not only depends on the formal

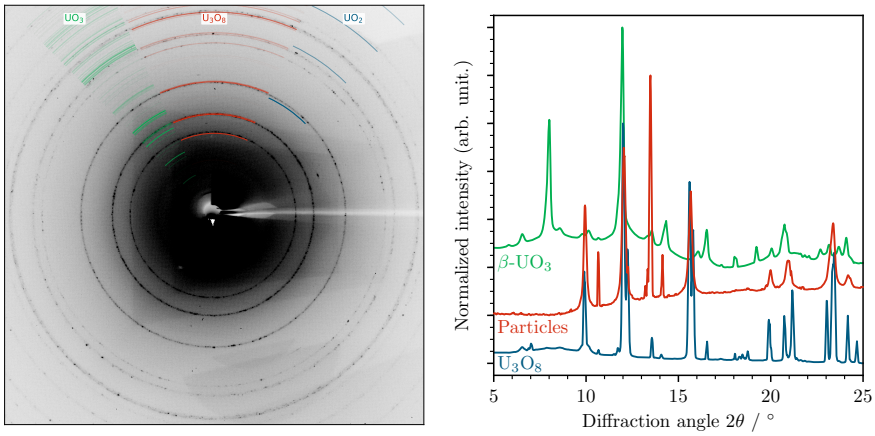

(a) Diffraction pattern **(b)** Diffractogram

Figure 4.19: Superimposed XRD pattern of microparticles produced from uranyl nitrate treated at 500 °C. The red bands correspond to the orthorhombic U_3O_8 phase. Reprinted with permission from Middendorp et al. [108 & 114] (see page 129).

oxidation state of the uranium, but also on the local coordination. The measured absorption spectra, collected on two different locations of the sample, are shown in Figure 4.20, together with spectra collected of β-UO_3 (U^{VI}) and U_3O_8 (U^{V} and U^{VI}) reference powders. The spectra collected of the microparticles are comparable to the spectra collected of U_3O_8 powder and therefore provide confirmation to the XRD results that the particles consist of U_3O_8 and not of UO_3, as would be expected based on the measurement of bulk uranyl nitrate.

The presence of U_3O_8 could be explained by the very low mass and relative high surface area of the microparticles compared to bulk amounts of material. Upon the thermal decomposition of uranyl nitrate, UO_3 is the first decomposition product. Although dependent on the modification, UO_3 decomposes to U_3O_8 starting from 550 °C to 700 °C. However, due to the very small amount of material present in a single particle and the relative high surface area, the decomposition could occur at a lower temperature. Also, Lodding and Ojamaa [49] reported on the auto-catalysis reaction of the thermal decomposition of uranyl nitrate hexahydrate in the presence of water vapor. Without the presence of water vapor, the formed N_2O_5 is expected to decompose into NO_2 and O_2, i.e. [49]

$$UO_2(NO_3)_2 \longrightarrow UO_3 + N_2O_5 \longrightarrow UO_3 + 2\,NO_2 + 0.5\,O_2$$

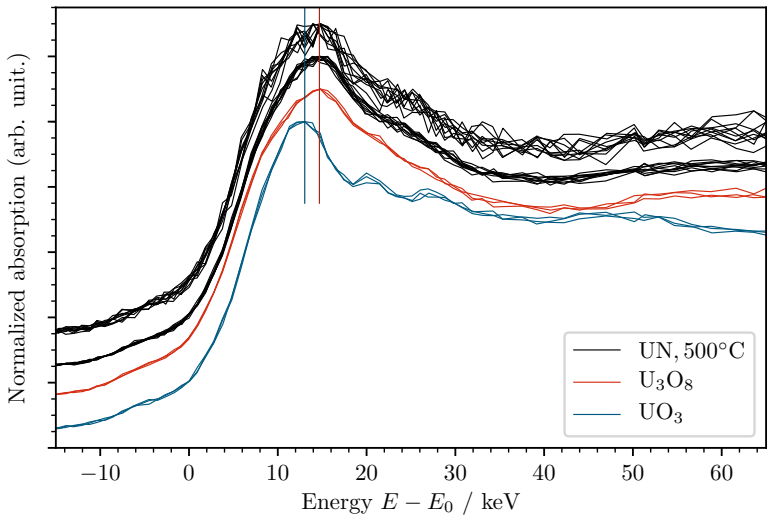

Figure 4.20: XANES spectra of particles produced from uranyl nitrate (UN) at 500 °C compared with spectra collected of β-UO_3 and U_3O_8 reference powders. The x-axis shows the energy shift compared to the uranium L_{III} absorption edge ($E_0 = 17.165$ keV).

However, in the presence of water vapor, the formed N_2O_5 is expected to react with water to form HNO_3, i.e.:

$$UO_2(NO_3)_2 \longrightarrow UO_3 + N_2O_5 + H_2O \longrightarrow UO_3 + 2\,HNO_3$$

Due to the lower oxygen partial pressure, the decomposition of UO_3 to U_3O_8 is more likely to occur in the presence of water vapor. Since most experiments dealing with bulk amounts of material have been performed under well controlled conditions whereas the production of microparticles is performed in an enclosed system, the presence of significant quantities of water vapor is more likely during the formation of microparticles. Therefore, more HNO_3 is expected to be produced which leads to a less strong oxidizing atmosphere. This, in turn, would cause the premature reduction of the formed UO_3 into U_3O_8. The final reaction taking place during particle formation from uranyl nitrate feed solution can therefore be written as:

$$\begin{aligned} UO_2(NO_3)_2 \cdot 6\,H_2O\,(s) &\xrightarrow[\text{dehydration}]{T < 200\,^\circ\text{C}} \\ UO_2(NO_3)_2\,(s) + H_2O\,(g) &\xrightarrow[\text{decomposition}]{200\,^\circ\text{C} \leq T < 400\,^\circ\text{C}} \\ UO_3\,(s) + 2\,HNO_3\,(g) &\xrightarrow[\text{reduction}]{200\,^\circ\text{C} \leq T < 400\,^\circ\text{C}} \\ UO_{2.67}\,(s) + 2\,HNO_3\,(g) + \tfrac{1}{6}\,O_2\,(g) & \end{aligned}$$

Although the XRD diffractogram in Figure 4.19 contains reflexes typical for the orthorhombic U_3O_8 phase, there are a number of additional reflexes which could not be assigned to any uranium containing phase. In order to verify whether these reflexes stem from uranium compounds, spatial maps were prepared containing the measured uranium L_α XRF intensity combined with the measured intensity of various reflexes. Figure 4.21 shows the spatial map of both a reflex assigned to the U_3O_8 phase ($2\theta = 15.3°$, red contours) and an unknown reflex at $2\theta = 13.5°$ (blue contours). The gray-scale image in the background represents the measured uranium L_α intensity in the XRF spectra. The XRF map shows a number of spots with increased intensity, which represent individual particles. The observed spots appear to be spherical and both individual particles and particle agglomerates can be identified. The large number of particle agglomerates is due to the high particle loading and used adhesive.

The intensity of the U_3O_8 phase shows a clear correlation with the measured uranium XRF intensity and all particles consists of the U_3O_8 phase. The contour plot of the unknown reflex shows one main spot, which is located next to a uranium particle. This unknown phase appears to be attached to the particle, but is free of uranium. This supports the hypothesis that the unknown phase originates from the adhesive. A number of particles also appear to contain traces of this phase, which is, however, likely due to an elevated intensity of the background at 13.5°, since background subtraction was complicated by the irregular background intensity.

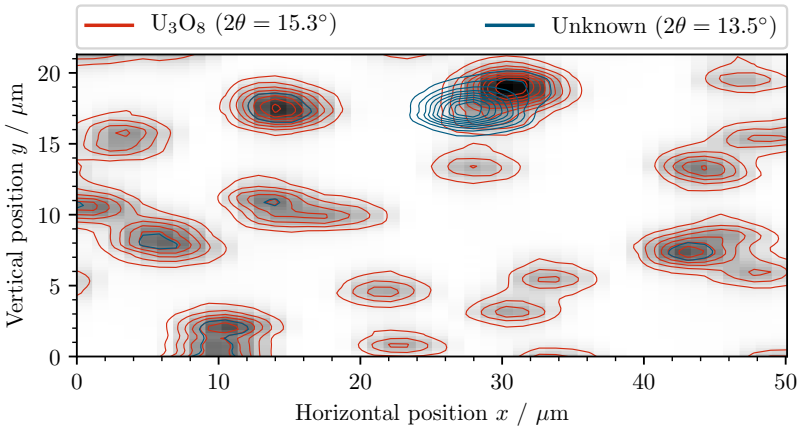

Figure 4.21: Spatial map of the measured uranium XRF intensity (map) with contour plots of two reflexes.

In addition to the particles treated at 500 °C, particles produced from uranyl nitrate treated at 400 °C and 600 °C were investigated. The collected XRD patterns (Figure 3 and Figure 5, respectively, Appendix) contain the orthorhombic U_3O_8 phase for all particles, which indicates that the thermal decomposition to U_3O_8 proceeds at much lower temperatures than reported in literature, as no U_3O_8 has yet been measured at temperatures as low as 400 °C. The lattice constants of the orthorhombic phase were refined by fitting Gaussian functions through the relevant reflexes and optimizing the lattice constants using the least-squares method. The obtained lattice parameters are given in Table IV, together with the lattice constants of all known orthorhombic uranium oxide phases. The lattice constants show good agreement with the α-U_3O_8 phase. Visual investigation of the collected XRD patterns indicates that the degree of crystallinity increases with increasing treatment temperature. At 400 °C, strong diffraction bands have been obtained whereas at 500 °C and increasingly at 600 °C more nanocrystalline domains were obtained. Although the observation lacks quantitative confirmation, such a behavior is expected to occur.

The presence of the U_3O_8 phase in particles treated at 400 °C and 600 °C was also confirmed by μ-XANES measurements, which yielded spectra comparable to the spectra collected for particles treated at 500 °C (Figure 7, Appendix). Based on the combined μ-XRD and μ-XANES studies, it can be concluded that uranyl nitrate microdroplets decompose to orthorhombic α-U_3O_8 at temperatures as low as 400 °C. Although different from expectation, the presence of the pentavalent and hexavalent uranium is likely to be advantageous compared to the purely hexavalent uranium UO_3 with respect to the long-term stability.

Table IV: Refined lattice constants of the orthorhombic phase observed in particles produced from uranyl nitrate at different treatment temperatures. The lattice constants of all known orthorhombic uranium oxide phases are given as comparison [33].

Phase	a / pm	b / pm	c / pm	V / nm^3
400 °C	686.8	1190.8	415.4	0.340
500 °C	680	1192	415.5	0.337
600 °C	685.0	1187.3	415.6	0.338
α-UO_3	684	4345	415.7	1.235
γ-UO_3	981.3	1993	971.1	1.899
ζ-UO_3	751.1	546.6	522.4	0.214
α-U_3O_8	671.6	1196.0	414.7	0.333
β-U_3O_8	706.9	1144.5	830.3	0.672
Schoepite	1433.7	1681.3	1473.1	3.551
Meta-schoepite	1127.06	710.55	2080.7	1.666

In addition to the μ-XRD and μ-XANES measurements, μ-Raman measurements were performed on particles produced from uranyl nitrate, although only particles treated at 500 °C were investigated. All collected spectra (Figure 9, Appendix) contain a single, high intensity peak at 521 cm^{-1} which is assigned to silicon [117], present as substrate material. Apart from the high intensity peak, a number of broad, low intensity peaks could be identified. The broadening of the peaks indicate a low degree of crystallinity, as previously seen in the μ-XRD patterns. Comparison of the obtained peak positions with reference spectra of uranium compounds [36, 85, 118–129] did, however, not provide a clear match. The closest match of spectral features was with spectra of decomposed U_3O_8 microparticles [85] and uranyl hydroxides ($UO_2(OH)_2$) [127] (Figure 4.22). Uranyl hydroxides are commonly used in a broad sense to indicate uranium ore concentrates (UOC's) and have been measured by numerous authors, although the measurement results are often not reproducible. The collected spectra of the produced microparticles show a resemblance with a spectrum collected from "South Dakota UOC", which is presumed to consist of $UO_2(OH)_2$.

Tamasi et al. [45] investigated the oxidation and hydration of U_3O_8 at various temperatures and humidities. After 3.5 a, hydration to schoepite ($UO_3 \cdot 2+x\,H_2O$) was observed, which can be described as a crystalline form of uranyl hydroxide ($UO_2(OH)_{2+x}$). As μ-Raman is a surface sensitive technique whereas μ-XRD and μ-XANES are penetrating methods, the formation of a thin layer of uranyl hydroxide on the surface of the particles would not be measurable by μ-XRD and μ-XANES. The measurements therefore show that the formed U_3O_8 particles apparently undergo surface hydration, i.e.:

$$U_3O_8 + 3\,H_2O \longrightarrow 3\,UO_2(OH)_2 + 0.5\,O_2$$

It should, however, be noted that the microparticles investigated by μ-XRD and μ-XANES were

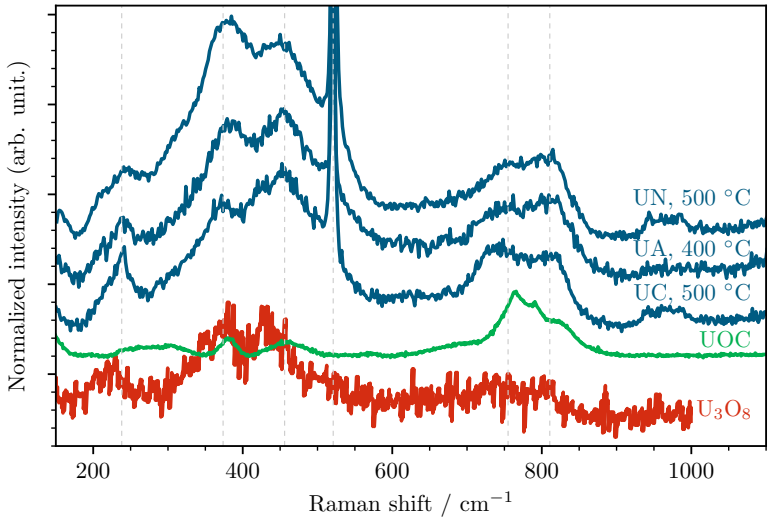

Figure 4.22: μ-Raman spectra of particles produced using a uranyl nitrate (UN), uranyl acetate (UA) and uranyl chloride (UC) feed solution and a thermal treatment of 500 °C, 400 °C and 500 °C, respectively. Reprinted with permission from Middendorp et al. [108] (see page 129).

stored under regular laboratory conditions for 35 days whereas the microparticles investigated by μ-Raman spectroscopy were stored for 155 days before measurement.

4.2.2 Particles from Uranyl Acetate

Investigation on the particle formation process using uranyl acetate precursor solutions resulted in the formation of spherical particles. Based on results published in literature [55–59, 130], these particles are expected to consist of U_3O_8 at 400 °C already, different from the uranyl nitrate based particles. However, as uranyl nitrate based particles were found to consists of U_3O_8 instead, particles produced from uranyl acetate solutions were investigated by μ-XRD, μ-XANES and μ-Raman to confirm the obtained phase.

The collected μ-XRD patterns (Figure 4.22 and 6, Appendix) show similar diffraction bands as in uranyl nitrate based particles, although the bands appear to be far more diffuse. The diffraction angles are similar to those of particles produced from uranyl nitrate, based on which can be concluded that the decomposition of uranyl acetate droplets at 400 °C results in microparticles consisting of an orthorhombic U_3O_8 phase. The collected μ-XANES spectrum (Figure 7, Appendix) also confirms this finding. The decomposition of micrometer-sized uranyl acetate particles can therefore be described as follows, where the decomposition of the acetate groups has been left out for clarity:

$$\mathrm{UO_2(CH_3COO)_2 \cdot 2\,H_2O\,(s)} \xrightarrow[\text{dehydration}]{T < 200\,^{\circ}\mathrm{C}}$$
$$\mathrm{UO_2(CH_3COO)_2\,(s) + 2\,H_2O\,(g)} \xrightarrow[\text{decomposition}]{200\,^{\circ}\mathrm{C} \leq T < 400\,^{\circ}\mathrm{C}}$$
$$\mathrm{UO_2\,(s) + 2\,CH_3COO\,(g) + 2\,H_2O\,(g) + O_2\,(g)} \xrightarrow[\text{oxidation}]{200\,^{\circ}\mathrm{C} \leq T < 400\,^{\circ}\mathrm{C}}$$
$$\mathrm{UO_{2.67}\,(s) + 2\,CH_3COO\,(g) + 2\,H_2O\,(g) + \tfrac{2}{3}\,O_2\,(g)}$$

μ-Raman measurements performed on particles produced from uranyl acetate also yields spectra (Figure 10, Appendix) comparable to the spectra collected for particles produced from uranyl nitrate. These results show that the obtained particles are similar to particles produced from uranyl nitrate and appear to have a thin surface layer consisting of uranyl hydroxide.

4.2.3 Particles from Uranyl Chloride

Due to the irregular shape of the obtained microparticles from uranyl chloride precursors, particles from uranyl chloride were only investigated by μ-Raman spectroscopy. The collected spectra (Figure 4.22 and 11, Appendix) are, however, comparable to the spectra obtained for particles produced from uranyl nitrate and uranyl acetate. As particles prepared from both uranyl nitrate and uranyl acetate resulted in the orthorhombic U_3O_8 phase and both yielded a uranyl hydroxide surface layer, the presence of such a uranyl hydroxide surface layer is an indicator that the particles produced from uranyl chloride also consists of U_3O_8 instead of the expected UO_3. The decomposition reaction leading to the formation of U_3O_8 can than be written as:

$$\mathrm{UO_2Cl_2 \cdot 2\,H_2O\,(s)} \xrightarrow[\text{dehydration}]{T < 300\,^{\circ}\mathrm{C}}$$
$$\mathrm{UO_2Cl_2\,(s) + 2\,H_2O\,(g)} \xrightarrow[\text{decomposition}]{300\,^{\circ}\mathrm{C} \leq T < 500\,^{\circ}\mathrm{C}}$$
$$\mathrm{UO_3\,(s) + 2\,HCl\,(g) + H_2O\,(g)} \xrightarrow[\text{reduction}]{300\,^{\circ}\mathrm{C} \leq T < 500\,^{\circ}\mathrm{C}}$$
$$\mathrm{UO_{2.67}\,(s) + 2\,HCl\,(g) + H_2O\,(g) + \tfrac{1}{6}\,O_2\,(g)}$$

4.2.4 Mixed Uranium/Cerium Microparticles

The previous investigations have focused on the production of pure uranium oxide microparticles from solutions with different uranyl species. In addition to such particles, particles were prepared consisting of a mixture of uranium and cerium(IV). Cerium is of interest as lanthanoide elements are often found in uranium compounds due to the similar chemical behavior. Of the lanthanoids, cerium has been selected as it is commonly used as surrogate for tetravalent actinoides, such as plutonium and thorium. A cerium(IV) nitrate solution was prepared by

dissolution of cerium dioxide in concentrated nitric acid. After drying and redissolution, the obtained solution was mixed with a uranyl nitrate solution. The obtained uranium/cerium nitrate solution was used to produce particles as described previously (section 3.2) with a thermal treatment of 500 °C. The uranium to cerium ratio of the solution was measured by Q-ICP-MS whereas the obtained particles were investigated by SEM/EDX (single particles) and Q-ICP-MS (bulk). No alteration of the elemental ratio was observed and no between-particle inhomogeneity larger than the measurement uncertainty was observed (Figure 4.23).

Produced particles with a cerium fraction ($N(\mathrm{Ce})/[N(\mathrm{Ce})+N(\mathrm{U})]$) of 0.17 mol mol^{-1} and 0.68 mol mol^{-1} were investigated by μ-Raman spectroscopy. Particles containing 0.68 mol mol^{-1} cerium (Figure 13, Appendix) showed different spectra compared to pure uranium microparticles, with a medium intense peak around 459 cm^{-1}. Such a single peak is commonly observed for cubic fluorite structures, such as UO_2 (445 cm^{-1}) [118, 120, 131] and CeO_2 (465 cm^{-1}) [132–134]. The single peak with a Raman shift in-between pure UO_2 and CeO_2 indicates that a solid-solution has been formed, although such cubic solid-solutions typically require a reducing atmosphere to form. However, studies on uranium/neodymium powders has shown the tendency to form such cubic structures upon heating in air, although the phase transformation was found as much higher temperatures ($T > 900$ °C) [112, 113].

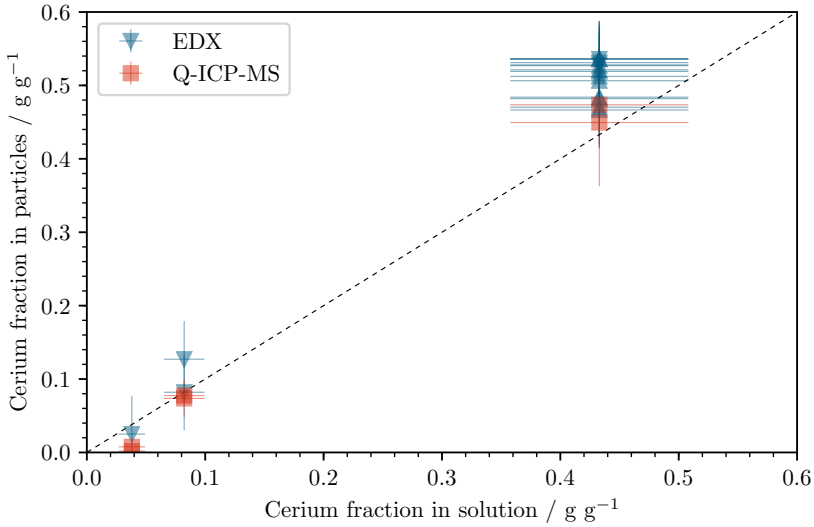

Figure 4.23: Cerium weight fraction of input solution (Q-ICP-MS) and produced particles (Q-ICP-MS and SEM/EDX).

Particles with a cerium fraction of 0.17 mol mol^{-1} (Figure 12, Appendix) do not show such a cubic phase and spectra comparable to pure uranium particles were obtained, which indicate that such particles still consist of orthorhombic U_3O_8. However, upon increasing the laser power from 0.25 mW up to 6.25 mW, an irreversible transformation was observed (Figure 4.24), resulting in a structure with a single Raman band around 455 cm^{-1}. This transformation shows that the cubic structure is thermodynamically more stable compared to the orthorhombic phase. Particles consisting of pure uranium were also investigated with a laser beam of 6.25 mW, which did not induce a phase transformation. These results show that the phase transformation is dependent on the presence of cerium in the particles and an increase of the cerium content leads to a decrease of the required energy.

The particles with a cerium fraction of 0.68 mol mol^{-1} were also investigated at increasing laser powers, were the power was increased in a step-wise fashion up to 12.5 mW (Figure 4.24b). During each step, a shift of the peak towards lower wavenumbers was observed, which indicates an increase of the bond lengths [135–138]. Upon decreasing the laser power back to 0.25 mW, the Raman band reverted to the original wavenumber, although a contraction of the peak compared to the initial measurement was observed, which indicates that the laser-induced particle heating causes recrystallization.

Particles containing a cerium fraction of 0.36 mol mol^{-1} were investigated by μ-XRD. The collected XRD patterns (Figure 4.25) contained a different structure than the previously ob-

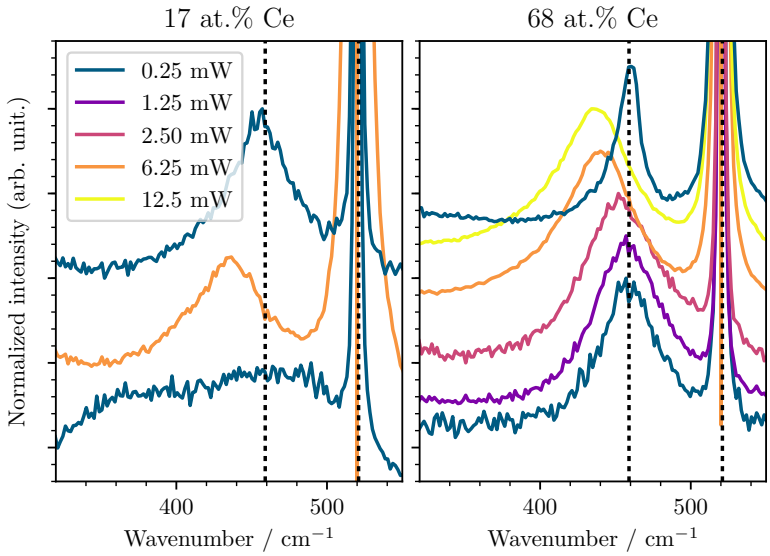

Figure 4.24: μ-Raman spectra of mixed uranium and cerium microparticles, measured at increasing laser power. The blue lines are collected at a laser power of 0.25 mW.

served orthorhombic phase and a cubic phase could be identified, although with a very low crystallinity. A lattice constant of approximately 545 pm was determined using the Nelson-Riley method [139]. This lattice constant lies between the lattice constants of pure UO_2 (546.8 pm) [140] and CeO_2 (541.1 pm) [141] and assuming Vegard's law [142],

$$a_{A_{1-x}B_x} = (1-x)a_A + x \cdot a_B, \tag{4.3}$$

the determined lattice constant corresponds to a cerium fraction of 0.49(22) mol mol^{-1}. Although the very broad reflexes indicate a low degree of crystallinity and a lattice deformation of 0.95 % was determined using the Williamson-Hall method [143], the results confirm the hypothesis that a stable uranium/cerium solid solution has been formed.

Although both μ-Raman spectroscopy and μ-XRD measurements resulted in a cubic phase for mixed uranium and cerium particles, the actual mechanism to the phase transformation remains unclear. In order to verify whether the phase transformation is accompanied by the reduction of the uranium to the tetravalent oxidation state, as would be expected for a UO_2 phase, μ-XANES measurements were performed on the particles containing a cerium fraction of 0.36 mol mol^{-1}. However, due to the low amount of material, the collected spectra were of low intensity, complicating the comparison with reference data. Even though, the spectral shape of the collected μ-XANES spectra (Figure 8, Appendix) appears to be comparable to the spectra obtained for the pure uranium particles, i.e. the μ-XANES measurement indicates that the uranium remains present in the mixed pentavalent/hexavalent oxidation state and no

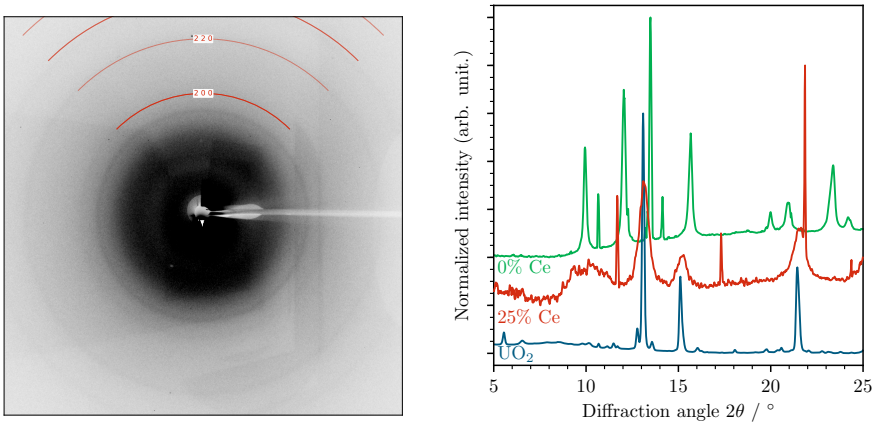

(a) Diffraction pattern **(b)** Diffractogram

Figure 4.25: XRD pattern of microparticles containing a mixture of cerium (0.36 mol mol^{-1}) and uranium (0.64 mol mol^{-1}) produced from the respective nitrate solutions treated at 500 °C.

reduction occurred during the phase transformation.

The oxidation of $U_{1-x}Ce_xO_2$ powders was previously investigated by Ruedorff and Valet [144]. Pure $U_{1-x}Ce_xO_2$ powders with different cerium fractions were oxidized in oxygen at 900 °C. A partial oxidation of the tetravalent uranium was observed, although based on the weight gain, no complete oxidation was attained. The obtained powders, consisting of a fluorite structure, were described as $CeO_2 \cdot UO_{2.5}$. Based on the μ-Raman, μ-XRD and μ-XANES studies and the results published by Ruedorff and Valet [144], the formed microparticles are expected to consist of tetravalent cerium and either pentavalent uranium or a mixture of tetravalent and hexavalent uranium. As the measured μ-XANES spectra are of rather low quality, it is not possible to differentiate between these structures and therefore the issue remains unresolved. The uranium and cerium are present as a solid-solid in a fluorite structured cubic phase. The simplified decomposition and particle formation reaction can therefore be given as:

$$(\overset{VI}{U}O_2)_{1-x}\overset{IV}{Ce}_x(NO_3)_{2+2x} \xrightarrow{\text{decomposition}}$$
$$\overset{V}{U}_{0.67}\overset{VI}{U}_{0.33}O_{2.67} + \overset{IV}{Ce}O_2 \xrightarrow{\text{transformation}}$$
$$\overset{V}{U}_{1-x}\overset{IV}{Ce}_xO_{2.5-0.5x} \; or \; \overset{IV}{U}_{0.5-0.5x}\overset{VI}{U}_{0.5-0.5x}\overset{IV}{Ce}_xO_{2.5-0.5x}$$

The given reactions assume that cerium remains in the tetravalent oxidation state. Possible reduction of cerium might influence the stability of the obtained product. Although initial studies did not show preferential leaching of cerium from the produced particles while stored in ethanol, further studies including XANES measurements of cerium are required before expanding the project to replace cerium by plutonium. However, based on previous studies focusing on the production of mixed uranium/plutonium microparticles [73] and the structural results obtained in this work, particles produced from a mixed uranium/plutonium solution are likely to consist of a highly homogeneous mixture of both elements.

4.3 Solid-Liquid Interactions

The previous investigations have focused on the particle formation process and chemical characterization of uranium oxide microparticles produced from various uranyl containing precursor solutions. The characterized particles obtained from these investigations can be used to investigate various reactions occurring between solid uranium oxides and solutions. Such stability assessments are of interest towards the certification of particles with respect to the uranium content and isotopic composition, as the transfer of particles into suspensions offer various advantages compared to the certification of directly collected particles (chapter 5.1). The stability of the uranium content of particles in solution is connected to the dissolution behaviour of the particles. Although dissolution reactions are generally well understood in aqueous solutions with bulk amounts of material, the behavior of microparticulate matter might be different. As the uranium isotopic composition of particles is of vital importance for the application as a particle reference material, the isotope exchange phenomenon is studied as well. Although the isotope exchange of oxygen isotopes between various phases is generally well understood [145–149], an extensive literature survey provided only a single experiment investigating the exchange of oxygen between water and uranium oxides [150] while no data for the exchange of uranium was found.

4.3.1 Dissolution

Uranyl Nitrate based Particles. The first effect investigated is the dissolution of particles in various solvents. Particles produced from uranyl nitrate solutions treated at 500 °C were collected onto silicon wafers which were, subsequently, stored in an enclosed vial containing the investigated solvent. To investigate the dissolution of particles, the produced particles were first stored in dilute nitric acid ($0.15\,\mathrm{mmol\,l^{-1}}$) for 17 hours and 24 hours, after which the particles were investigated by SEM. The obtained micrographs are shown in Figure 4.26 and show that significant dissolution occurred during storage. The micrographs collected after 17.3 hours still show spherical particles, although the measured BSED intensity was strongly

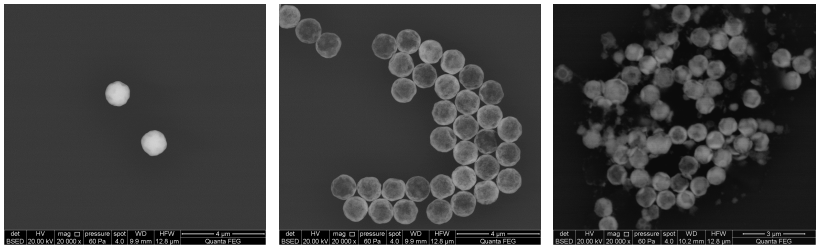

(a) Initial **(b)** 17.3 hours **(c)** 23.6 hours

Figure 4.26: SEM micrographs of microparticles after storage in dilute nitric acid ($0.156\,\mathrm{mol\,l^{-1}}$) for 17 hours and 24 hours.

decreased, indicating homogeneous dissolution of uranium from the particles. As the particle size is comparable to the particle size before dissolution, this decrease of intensity indicates a decrease of particle density. Although consisting of a different sample, particles stored in nitric acid for 23.6 hours show a strongly different morphology and only shells remain. This transition indicates that the core of the particle was dissolved. As the particles were found to consist of a dense shell but with a porous core, these results indicate that the solvent is capable of penetrating the dense shell and infiltrate the pores. As the total surface area of the particle core is much higher than the particle surface, the dissolution of the core proceeds at a faster rate, resulting in the found shells.

Similar studies were performed for a wide range of solvents, which were selected on their availability in high purity (water, ethanol, 2-propanol, and n-decane) or with the prospect of further processing options, such as dimethyl formamide (DMF) which is used for the preparation of polyimide foils [151, 152]. Also, water with an added surfactant (PVP-20 000) was included to investigate the effect of a surfactant, which often enhance the stability of nano- and microparticles in suspensions [153]. The particles were stored in the various solvents for 16 days, the collected micrographs after storage are shown in Figure 4.27.

The collected micrographs show that particles stored in water undergo dissolution in a similar fashion compared to the particles stored in nitric acid; the particle core is dissolved at a higher rate than the particle surface. The addition of a surfactant (PVP-20 000) to the water does

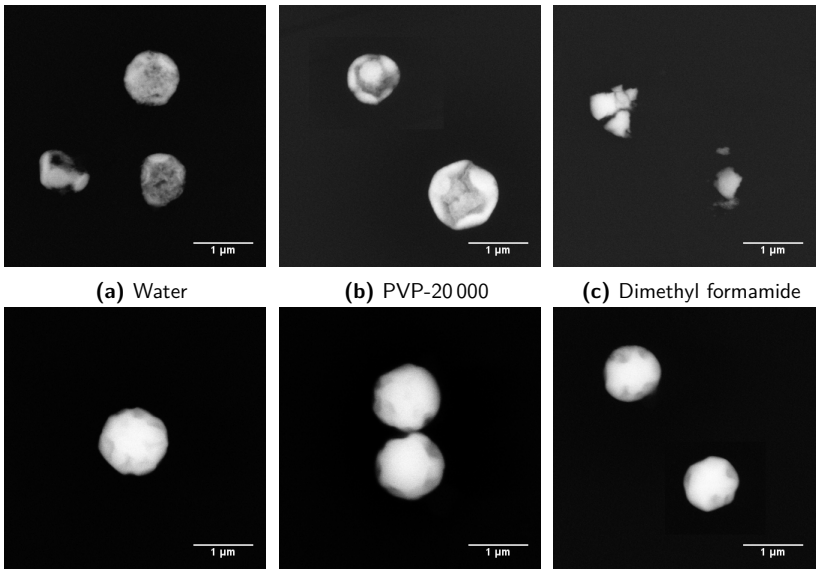

(a) Water **(b)** PVP-20 000 **(c)** Dimethyl formamide

(d) Ethanol **(e)** 2-Propanol **(f)** n-Decane

Figure 4.27: SEM micrographs of particles after storage in various solvents for 16 days. Adapted with permission from Middendorp et al. [114] (see page 129).

not prevent the dissolution of the particle. Although the efficiency of the surfactant could be improved by further adjustment of the surfactant concentration or the length of the surfactant chains, such investigations have not been undertaken in this work. A different behavior of the particles was observed in dimethyl formamide. Instead of dissolution, particle fragments were found where the BSED intensity indicate that the observed fragments have a high density, similar to the initial particles. This, in turn, indicates that the particles break-up. Such effect might be caused by the evaporation of the dimethyl formamide upon drying of the sample, causing an increase of the internal pressure, leading to the fracturing of the particles. The particles which were stored in ethanol, 2-propanol and n-decane do not show any signs of dissolution or fracturing.

For further handling of the particles, the particles need to be detached from the substrate, which can be achieved by ultrasonification. The detachment efficiency of the particles from the substrate (α_C) depends, however, on the density (ρ) and viscosity (η) of the solvent, as expressed by equation 4.4 [154] and shown graphically for a number of solvents in Figure 4.28.

$$\alpha_C = \frac{\eta x_0 R_p^2 \sqrt{\frac{P_C}{\rho\beta(1-\beta)}}}{1.5 W_A} \tag{4.4}$$

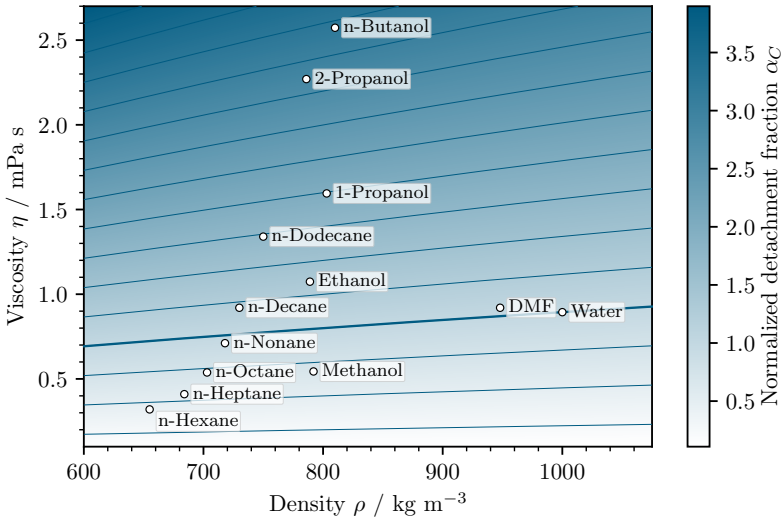

Figure 4.28: Normalized detachment efficiency of particles from a substrate using an ultrasonic bath in various media. Reprinted with permission from Middendorp et al. [114] (see page 129).

Although a number of the factors from equation 4.4 are unknown, the equation shows that the detachment efficiency increases strongly with an increasing viscosity whereas a minor increase is expected for media with an increasing density. It was found that the detachment of particles into ethanol and 2-propanol was highly efficient, whereas detachment of particles in n-hexane was very inefficient. n-Hexane was investigated due to the high boiling point of n-decane, which would cause complications during the drying of suspensions onto substrates for further investigations. These investigations show that, although no dissolution appears to occur while the particles are stored in alkane solution, alkane solutions were not further investigated. The particles stored in ethanol and 2-propanol were also investigated after storage for 432 days in solution, although no alteration of the particles was observed (Figure 4.29). This indicates that the particles can be considered stable for prolonged storage in both ethanol and 2-propanol. During the investigations, particles suspended in 2-propanol were found to agglomerate more than particles suspended in ethanol (see section 5.3). Therefore, all following studies were performed using ethanol.

In addition to the visual investigation, the ethanol contacted with microparticles was extracted and analyzed by Q-ICP-MS. The collected samples showed traces of uranium present in the solution. To distinguish between dissolved uranium and suspended uranium particles, the samples were filtered over a 0.45 µm membrane filter. The collected filtrate is expected to contain the dissolved uranium whereas the filter is expected to contain the retained suspended microparticles. Both samples were dissolved in nitric acid and measured by Q-ICP-MS. The uranium mass in the dissolved phase (filtrate) is very low and close to the limit of detection, which could not be determined in a reliable way. The relative amount of uranium dissolved was calculated based on the total uranium mass present in the system (7.16(55) µg), which was determined by dissolution of all particles after removal of the final sample aliquot and was corrected for removal of material during sampling. For the last three samples, which were collected simultaneously after a contacting time of 228 days, a mean dissolved fraction of 1.32(22) mg g^{-1} was calculated (Table V).

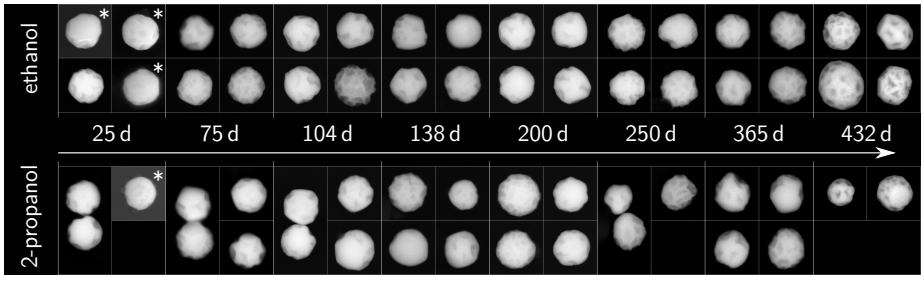

Figure 4.29: SEM/BSED micrographs of particles produced from uranyl nitrate during storage in ethanol for up to 432 days. *SEM/SE micrograph.

Table V: Uranium content measured in ethanol after contact with microparticles for time t. The relative amount of uranium dissolved (w_{diss}) is based on the initial uranium mass of 7.16(55) µg.

t / d	$m(\mathrm{U})_{\mathrm{diss}}$ / ng	w_{diss} / mg g^{-1}
140	10.5(29)	1.46(42)
172	12.1(25)	1.69(37)
228	9.3(17)	1.30(25)
228	9.3(15)	1.31(24)
228	7.2(13)	1.01(20)

This low fraction indicates that traces of uranium were dissolved, which could stem from two sources. As not all particles present on the sample could be investigated, the samples could have contained a small number of "non-conforming" particles, such as inflated particles, with a higher tendency to dissolve compared to the "typical" particles, for example due to higher surface areas. Rapid dissolution of such "non-conforming" particles would increase the uranium concentration of the solution without significant dissolution of the intended reference particles. On the other hand, it would be possible that a small amount of material was dissolved from all present particles. In such a case, the small amount of dissolved material (0.132(22) %) is negligible compared to the expected accuracy of the ID-TIMS measurements of 5 % [77, 78] with which the uranium content is planned to be certified. Moreover, it could not be ascertained that the prepared samples are free of cross-contaminations, for example during filtration. Possible cross-contamination from an external source would increase the measured uranium concentration of the solution.

Uranyl Acetate based Particles. In addition to the investigations of the dissolution of microparticles produced from uranyl nitrate precursor solutions, particles produced from uranyl acetate were investigated. Figure 4.30 shows SEM micrographs collected of particles after storage in ethanol for 83 days. The micrographs show clear signs of dissolution. The micrographs not only show that the dissolution proceeds at a much higher rate compared to particles produced from uranyl nitrate, but also a different mechanism. Where the dissolution of particles produced from uranyl nitrate commences at the particle core appears the dissolution of the uranyl acetate based particles to be more or less homogeneous throughout the particles.

Such a behavior would be in accordance to the observed porosity as seen in Figure 4.9. Uranyl nitrate based particles have dense shells with relative large pores in the particle cores (Figure 4.15) whereas uranyl acetate based particles have homogeneously distributed nanopores throughout the particles. The total surface area of the uranyl acetate based particles is therefore much higher compared to the uranyl nitrate based particles, due to which dissolution occurs at a higher rate. Also, as the porosity is homogeneously distributed, the dissolution commences at all pores whereas for uranyl nitrate based particles, most surface area is present at the particle

core, due to which the dissolution commences from the particle core instead. It can therefore be concluded that the particles produced from uranyl acetate are not suitable for transfer via particle suspensions.

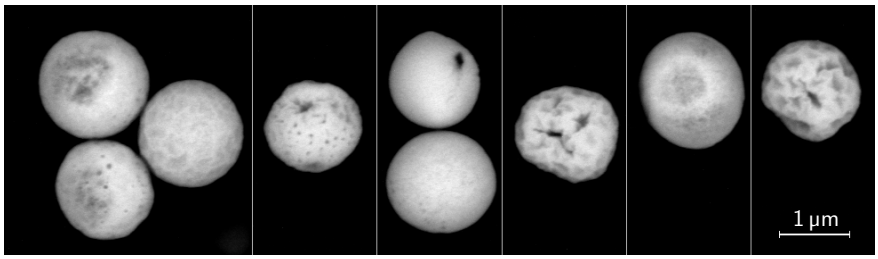

Figure 4.30: SEM/BSED micrographs of particles produced from uranyl acetate after storage in ethanol for 83 days.

4.3.2 Uranium Isotopic Exchange

Theoretical. The previous dissolution experiments have shown the behavior of microparticulate matter in unequilibrated systems, the solid phase dissolved resulting in a decrease of the uranium content in the solid phase and an increase of the uranium content in the liquid phase. Such reactions do, however, also continue in equilibrated systems, although the rate at which species are transferred from the solid phase to the liquid phase is equal to the reverse reaction, for example by precipitation, i.e. $R_{\text{dissolution}} = R_{\text{precipitation}}$.

In the case of a system where the isotopic composition of one of the atoms in the solid phase differs from the isotopic composition of the same atom in the liquid phase, the continuous exchange of atoms between both phases results in the change of the isotopic composition of both phases. The reaction rate involved in the exchange reaction has previously been described by several authors [146, 155–158], although the derivations will be repeated in the following section due to minor differences of the used methods employed in this work, notably the usage of isotope ratios instead of concentrations or activities.

The general reaction occurring during isotope exchange processes can be described as

$$\mathrm{AX} + \mathrm{BX^*} \rightleftharpoons \mathrm{AX^*} + \mathrm{BX}$$

in which AX and BX are two species and $\mathrm{X^*}$ denotes a distinctive isotope of element X. The concentration of the various species can be defined as

$$\begin{aligned} x &= c(\mathrm{AX^*}); \qquad & a &= c(\mathrm{AX}) + c(\mathrm{AX^*}); \\ y &= c(\mathrm{BX^*}); \qquad & b &= c(\mathrm{BX}) + c(\mathrm{BX^*}). \end{aligned}$$

The rate at which x changes can be described as a combination of two functions, representing the forward and reverse reactions

$$\frac{\delta x}{\delta t} = k f_{\mathrm{f}}(a) f_{\mathrm{r}}(b) \tag{4.5}$$

The rate can also be expressed by the reaction rate R, which represents the absolute rate or reaction occurring in the investigated system and is dependent on the sample properties, such as the concentration and temperature. The change of x can then be defined as

$$\frac{\delta x}{\delta t} = R\frac{y}{b} - R\frac{x}{a} = \frac{R}{ab}(ay - bx) \tag{4.6}$$

The change of x continues until equilibrium, i.e. $x/a = y/b$. The equilibrium concentrations of x and y at $t = \infty$ can then be calculated as

$$x(\infty) = x_\infty = \frac{x+y}{a+b} \cdot a \tag{4.7}$$

$$y(\infty) = y_\infty = \frac{x+y}{a+b} \cdot b. \tag{4.8}$$

As the concentration of y depends on the concentration of x,

$$y = x_\infty + y_\infty - x \tag{4.9}$$

and

$$y_\infty = x_\infty \frac{b}{a}, \tag{4.10}$$

the concentration of y can be rewritten as

$$y = x_\infty + x_\infty \frac{b}{a} - x \tag{4.11}$$

Combining equation 4.6 and 4.11 leads to

$$\frac{\delta x}{\delta t} = \frac{R}{ab}\left[a(x_\infty + x_\infty \frac{b}{a} - x) - bx\right] \tag{4.12}$$

$$= \frac{R}{ab}\left[(a+b)(x_\infty - x)\right] \tag{4.13}$$

which can be rearranged to

$$\frac{\delta x}{x_\infty - x} = \frac{R}{ab}(a+b)\delta t. \tag{4.14}$$

Integration results in a first-order rate equation which can be used to determine the reaction rate R,

$$-\ln\left(1 - \frac{x}{x_\infty}\right) = \frac{R}{ab}(a+b)t. \tag{4.15}$$

In practical cases, often the isotope ratio is measured instead of concentration, i.e. $X = x/a$ and $Y = y/b$. Also, to compare the different phases, the degree of reaction α is commonly calculated, which described the progress towards equilibrium, where $\alpha = 0$ is the initial state and $\alpha = 1$ indicates equilibrium,

$$\alpha(t) = \frac{X(t) - X(0)}{X(\infty) - X(0)}. \tag{4.16}$$

The reaction rate of the exchange reaction can then be calculated as

$$R = -\frac{\ln(1-\alpha)}{t}\frac{ab}{a+b}. \tag{4.17}$$

Assuming the reaction follows first-order kinetics, the rate constant k of the reaction can be calculated as

$$\ln\left(\frac{x_\infty}{x_\infty - x}\right) = \frac{R}{ab}(a+b)t = kt, \tag{4.18}$$

which can, in turn, be used to estimate the activation energy E_A according to the Arrhenius equation,

$$k = A_0 e^{-E_\mathrm{A}/(RT)} \tag{4.19}$$

Exchange in Aqueous Systems. The exchange of uranium between solid triuranium octoxide (U_3O_8 or $UO_{2.67}$) and uranium dissolved in water (presumably UO_2^{2+}) was investigated using the isotope pair ^{235}U and ^{238}U. The exchange reaction can be given as:

$$\underset{AX}{^{235}UO_{2.67}(s)} + \underset{BX^*}{^{238}UO_2^{2+}(aq)} \rightleftharpoons \underset{AX^*}{^{238}UO_{2.67}(s)} + \underset{BX}{^{235}UO_2^{2+}(aq)}$$

The solid phase consists of millimeter-sized particles with an average diameter of $884(48)\,\mu m$ ($1.76(16)\,mg$ uranium) which were prepared by an external gelation sol-gel synthesis [112, 159], where droplets of uranyl nitrate mixed with urea and hexamethylenetetramine (HMTA) are added drop-wise to heated silicon oil, in which the HMTA decomposes and ammonium hydroxide is released which, in turn, leads to the precipitation uranyl hydroxide. Due to the droplet shape and the silicon oil medium, spherical particles are formed. After washing and drying, the millimeter-sized particles were calcined at $900\,^\circ C$ during which the uranyl hydroxide decomposes to triuranium octoxide. The existence of a U_3O_8 phase was confirmed by powder XRD. BET measurements of the produced millimeter-sized particles resulted in a surface area of $1.52\,m^2\,g^{-1}$.

The liquid phase was prepared by storage of β-UO_3 in ultra-pure water for 144 days, after which the solution was expected to be in equilibrium. β-UO_3 was used due to the presence of hexavalent uranium, which dissolved in water at a higher rate compared to U_3O_8. Single millimeter-sized particles were contacted with the prepared liquid phase, in time aliquots of the solution were removed for Q-ICP-MS analysis. After three subsequent samplings, the millimeter-sized particle was removed, flushed with ultra-pure water and dissolved for analysis of the solid phase.

Figure 4.31 shows the evolution of the $m(^{235}U)/m(^{238}U)$ isotope ratio, hereafter given as X, after prolonged contact of the solid [DU]U_3O_8 millimeter-sized particles with a LEU saturated aqueous solution. At $t = 0$, the measured ratio is similar to the ratio of the used LEU material, indicating that no significant cross-contamination occurred during sample preparation. Over time, the ratio of the liquid phase decreases, indicating an exchange of ^{235}U with the solid DU phase. The decrease of the isotope ratio appears to follow first-order kinetics, as is typically observed in isotope exchange experiments [146]. The isotope ratio appears to reach equilibrium slightly above the initial isotope ratio of the solid phase. The equilibrium ratio of the system was estimated based on the amount of uranium in the solid and liquid phase and the initial isotope ratio, resulting in a ratio of $0.554\,\%$. As the reaction follows first-order kinetics, an exponential function was fitted through the data using the least-squares method, from which an equilibrium isotope ratio $X(\infty)$ of $0.545\,\%$ was estimated. The close agreement of the calculated and fitted equilibrium ratio shows that the observed decrease of isotope ratio reflects the expected isotope exchange reaction.

In addition to the measurements performed on the liquid phase, a number of measurements were performed on the solid phase. As the isotope exchange occurs between the solid and

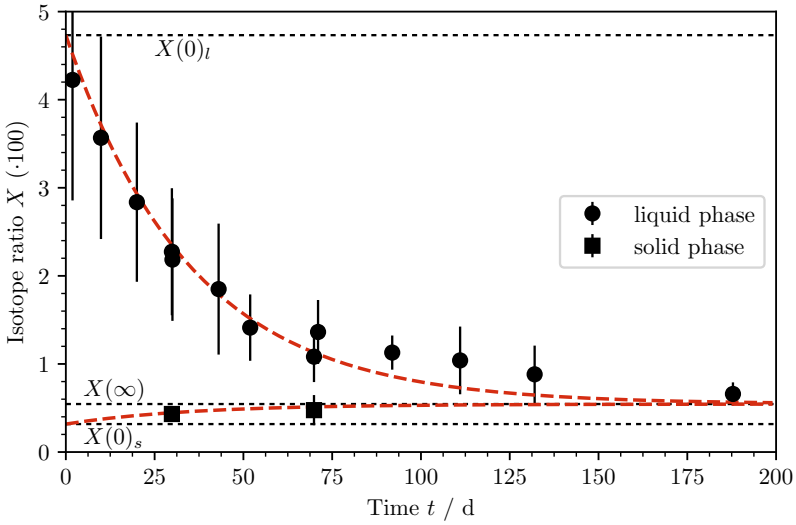

Figure 4.31: Isotope ratio of the solid (U_3O_8) and liquid (UO_2^{2+}(aq)) phase after contact in aqueous solutions at 21 °C. The horizontal lines $X(0)_s$ and $X(0)_s$ denote the initial isotope ratio of the solid and liquid phase, respectively, and $X(\infty)$ denotes the expected isotope ratio at equilibrium.

liquid phase, the isotope ratios of both phases are proportional to one another. In order to compare the ratios from both the solid and liquid phase, the degree of reaction (α) was calculated for each measurement based on equation 4.16. A plot of $\ln(1-\alpha)$ versus t should result in a straight line which intersects through zero. Figure 4.32 shows the obtained plot for the exchange in aqueous solutions at 21 °C and shows a linear decrease of $\ln(1-\alpha)$ for both the solid and liquid phase. Also, the calculated degree of reaction of both the solid and liquid phase are in agreement with another, confirming that exchange of isotopes between both phases occurs without the presence of a second, concurrent mechanism. The slope of the linear fit can also be used to estimate the reaction rate R, according to equation 4.15 and a reaction rate of 142(24) nmol g^{-1} m^{-2} h^{-1} was calculated.

Other than the studies performed at room temperature ($T \approx 21$ °C), the experiments were repeated at elevated (50 °C) and decreased (14 °C) temperatures. The obtained data showed similar trends as observed at 21 °C, although an increase of the reaction rate was measured at increasing temperature. In order to compare the data obtained from the different experiments, the reaction rate constant k was calculated using equation 4.17. The determined rate constant shows a dependence on the temperature at which the experiments were performed, the increase of the rate constant as function of the temperature can be described by the Arrhenius equation (equation 4.19), from which the activation energy E_A of the reaction can be calcu-

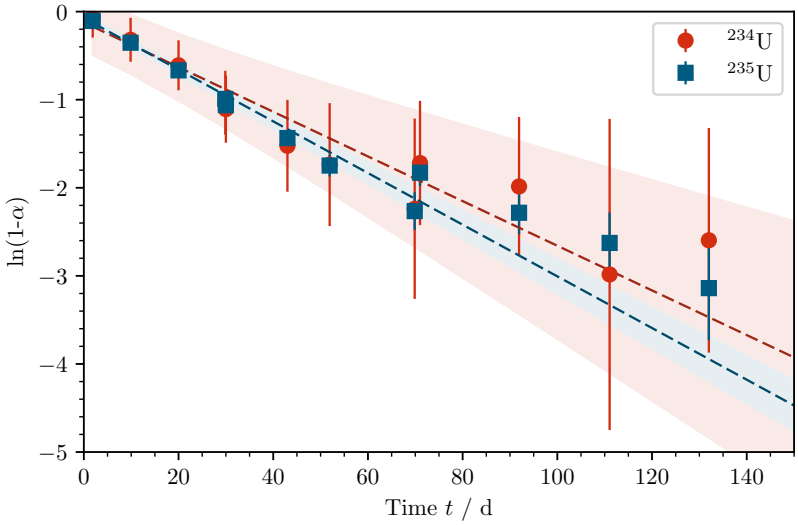

Figure 4.32: Degree of reaction α determined from experimental data as function of time for both the solid and liquid phase, after contact in water at 21 °C.

lated by plotting the natural logarithm of the reaction rate against the inverse temperature (Figure 4.33). Such a plot leads to a straight line where the slope corresponds to E_A/R. For the investigated system, an activation energy of 34.7(29) kJ mol^{-1} was calculated. The activation energy can be used as indicator for the mechanism of the observed reaction; Cole and Chakraborty [146] reported on a large number of exchange reactions, where the following reaction mechanisms were given with their respective activation energies:

- Reactions in solutions: $E_A \approx 20\,\text{kJ mol}^{-1}$,
- Mineral transformation/surface reactions: $40\,\text{kJ mol}^{-1} < E_A < 80\,\text{kJ mol}^{-1}$,
- Solid state diffusion: $E_A \gg 100\,\text{kJ mol}^{-1}$.

Although the given values provide by no means a conclusive mechanism, the measured activation energy of the investigated reaction indicates that the exchange occurs via a surface reaction rather then diffusion.

In order to obtain additional information towards the reaction mechanism, a number of experiments were performed by contacting powdered U_3O_8 and β-UO_3 to saturated uranium solutions with varying pH. At neutral pH, exchange was observed for both U_3O_8 and β-UO_3, although the exchange reaction for β-UO_3 proceeded at a faster rate than the reaction involving U_3O_8. Due to the experimental conditions, no accurate reaction rates could be calculated. The increased reaction rate for β-UO_3 compared to U_3O_8 indicates that the actual exchange occurs via hexavalent uranium. As β-UO_3 consists of purely U(VI) whereas U_3O_8 consists of a mixture

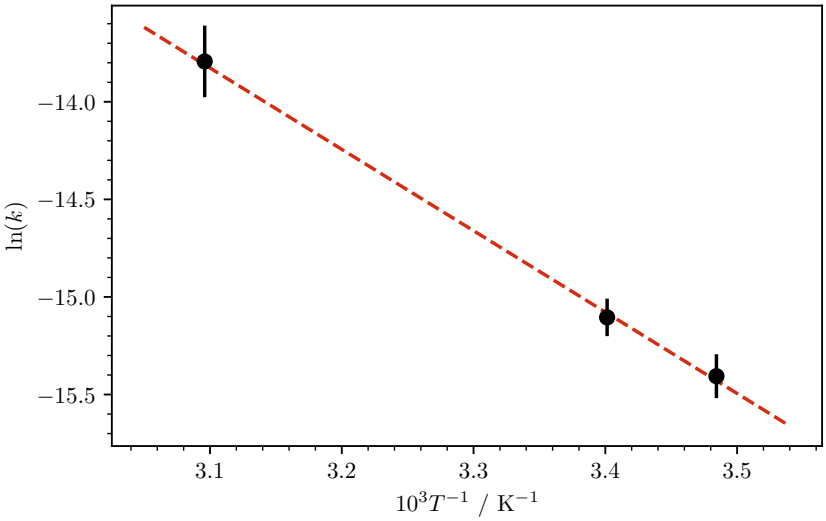

Figure 4.33: Temperature dependence of the uranium isotope exchange reaction between [DU]U_3O_8(s) and [LEU]UO_2^{2+}(aq).

of U(V) and U(VI), the exchange between aqueous uranium and U_3O_8 requires reduction of the uranium.

A decrease of the solution pH to 3.95 leads to a decrease of the exchange rate. The lower reaction rate at decreased pH is likely related to the speciation of uranium in the solution (Figure 2.4). When assuming a pure aqueous solution, at a pH of 4, the main species is the linear uranyl ion, UO_2^{2+}. Upon an increase of the pH, the formation of a complex mixture of uranyl hydroxides tends to form and at a pH of 7, UO_2OH^+ is the main constituent of the aqueous solution. As the μ-Raman measurements indicated that the particles contain a thin surface layer consisting of uranyl hydroxide, continues precipitation and dissolution of the uranyl hydroxide is the most likely reaction pathway leading to the exchange of uranium between the solid and liquid phase.

$$\underset{\text{liquid}}{UO_{2-x}(OH)_x(aq)} \underset{\text{precipitation}}{\overset{\text{dissolution}}{\rightleftharpoons}} \underset{\text{surface}}{UO_2(OH)_2(s)}$$

As the measured isotope exchange reaction proceeds to the calculated equilibrium ratio, all uranium within the particle is involved in the exchange reaction. However, as the uranyl hydroxide surface layer is expected to have a thickness of only a few nanometer, the exchange of uranium between the uranyl hydroxide surface layer and the triuranium octoxide phase is expected to occur in parallel, increasing the thickness and therefore volume of the reactive

surface layer.

$$\underset{\text{surface}}{UO_2(OH)_2(s)} \underset{\text{reduction}}{\overset{\text{oxidation}}{\rightleftharpoons}} \underset{\text{solid}}{U_3O_8(s)}$$

As the particles were found to contain nano- and micropores, the total volume of a reactive surface layer with a thickness of a few hundred nanometer is likely to be similar to the entire surface of the microparticle. The overall exchange reaction is therefore expected to proceed via two distinct steps, with the precipitation/dissolution of uranyl hydroxide between the solution and the uranyl hydroxide surface layer and the oxidation/reduction of U(VI) and U(V) between the uranyl hydroxide surface layer and the triuranium octoxide phase (Figure 4.34).

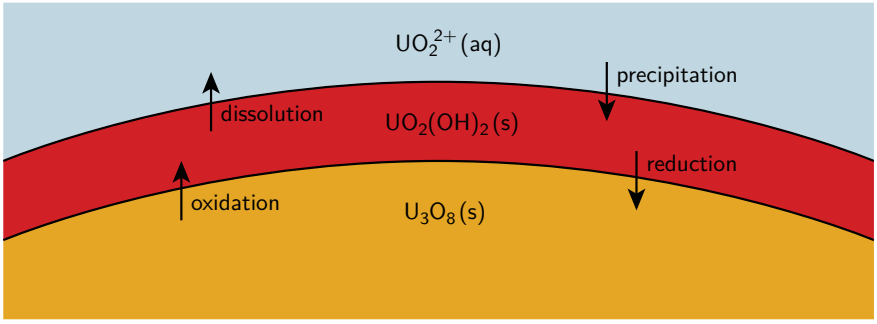

Figure 4.34: Schematic overview of the exchange of uranium between a solid U_3O_8 phase and an aqueous uranium phase in an equilibrated system.

Exchange in Alcoholic Systems. The dissolution studies of microparticles in ethanol and 2-propanol (section 4.3.1) show no significant reactions in these media. To investigate whether isotopic exchange occurs, U_3O_8 millimeter-sized particles were stored in uranium saturated ethanol and 2-propanol. The saturated solutions were, similar to the saturated aqueous solution, prepared by contacting β-UO_3 with the solvents for 104 days. During the experiments, a decrease of the uranium concentration in 2-propanol was observed, which is likely caused by the reduction of the dissolved uranium to the tetravalent oxidation state followed by the precipitation of uranium dioxide, as previously described by Nakashima [98],

$$CH_3CHOCH_3 + UO_2^{2+} \rightleftharpoons CH_3COCH_3 + UO_2\downarrow + 2\,H^+$$

Upon addition of the solid U_3O_8, the equilibrium was disturbed and a dissolution of the solid phase was observed at both 14 °C and 21 °C. At 50 °C, however, further precipitation was observed. These unequilibrated systems do not allow for the investigation of the uranium exchange between both phases.

In ethanol, no precipitation of uranium was observed and the uranium concentration remained constant during the experiments (188 days). At none of the investigated temperatures of 14 °C, 21 °C and 50 °C any significant change of the isotope ratio was measured in both

the solid and liquid phase. From these results can be concluded that in ethanol, no surface exchange reaction occurs, as is the case in aqueous solutions. Any exchange which might occur would proceed via diffusion, which typically have very low reaction rates and are only of interest for geological timescales.

Exchange between Microparticles. Although the obtained results indicate that isotopic exchange between U_3O_8 and uranium dissolved in ethanol proceeds mostly by diffusion, the high surface area and relative volume close to the surface of the microparticles produced in this work might lead to an increased reaction rate for microparticles. Therefore, microparticles were produced from uranyl nitrate solutions, consisting of depleted and low-enriched uranium. Silicon wafers containing the particles were stored in ethanol. Each vial contained one wafer containing depleted uranium microparticles, a second wafer containing low-enriched uranium microparticles and a third, blank wafer. Twelve vials were prepared and stored for various times. After storage, the three wafers were extracted separately and placed in nitric acid to dissolve all particles. The solutions containing the dissolved particles were analyzed by Q-ICP-MS (Figure 4.35).

Figure 4.36 shows the measured isotopic composition of the wafers containing the initially DU and LEU microparticles. In time, no significant change of the isotopic composition of both the DU and LEU microparticles was measured. The performed investigations do, however, differ slightly from the experiments using the millimeter-sized particles, as during the millimeter-sized particles experiments the exchange between uranium in a solid and liquid phase was investigated whereas in the microparticle experiments the exchange between two particle populations, presumably via the liquid phase, was investigated (i.e. DU particle $\rightleftharpoons$ solution $\rightleftharpoons$ LEU particle). The absence of such isotope exchange is, however, a strong indication that the produced particles remain stable while stored in ethanol suspensions and that such suspensions can be used to produce mixtures of particles consisting of particles with different isotopic compositions.

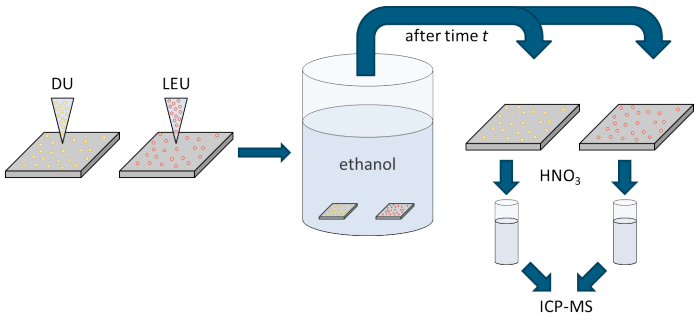

Figure 4.35: Schematic overview of the isotope exchange investigations between DU and LEU microparticles. Reprinted from Middendorp et al. [160].

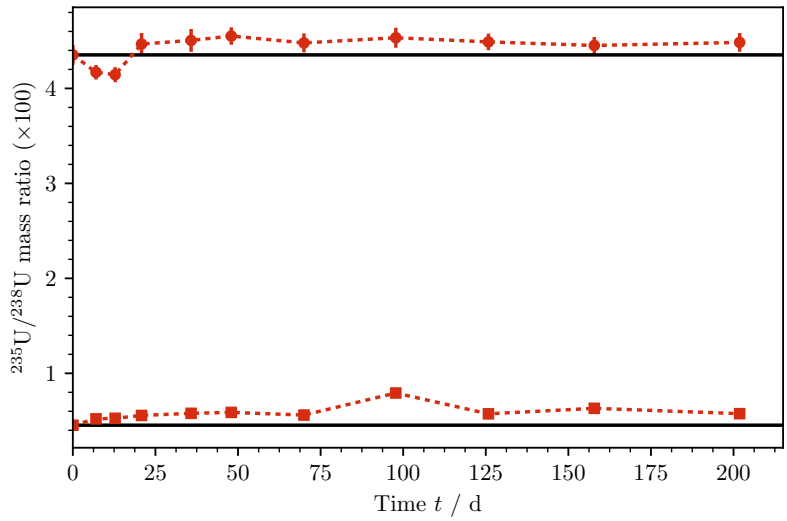

Figure 4.36: Isotopic composition of DU and LEU microparticles stored in a single vial filled with ethanol.

5 Application as Particle Reference Material

5.1 Requirements on Particle Reference Materials

5.1.1 Nuclear Safeguards

Nuclear safeguards have been implemented to verify the commitment of member states to the Treaty on Non-proliferation of Nuclear Weapons, as described in chapter 1. Among the various measures implemented to detect undeclared activities, the particle analysis has proven to be a valuable tool [4]. Over the recent years, progress has been made within the nuclear safeguards particle analysis, both to increase the accuracy of measurements and to increase the detection probability of non-conforming particles.

The improved measurement accuracy enables the analysis of the minor isotopes, instead of only the major isotopes. The minor isotopes (e.g. ^{234}U and ^{236}U) provide detailed information regarding the discovered material and the history of the material, for example, the ^{234}U/^{235}U and ^{236}U/^{238}U ratios provide information regarding the used source material (Figure 5.1).

The very low content of the minor isotopes and the small deviation of the different values requires a very high measurement accuracy to differentiate between different types of particles. Recent advances, mostly the introduction of large geometry (LG) SIMS, have opened the possibility to measure the minor isotope ratios within single microparticles with high accuracy. In optimal cases, the combined measurement uncertainty has improved down to 1 %, relative,

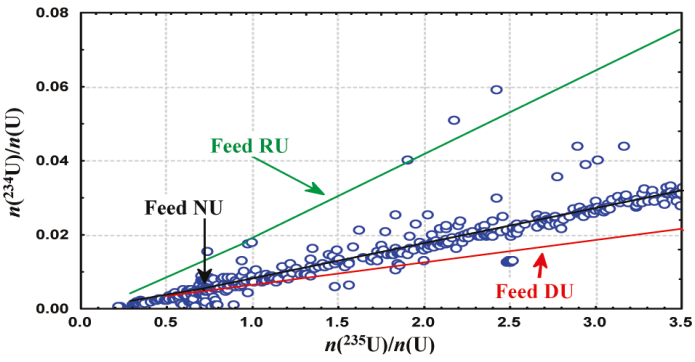

Figure 5.1: ^{234}U/^{235}U isotope ratio measured in microparticles originating from depleted uranium (DU), natural uranium (NU) and reprocessed uranium (RU) source materials. Reprinted with permission from Kraiem et al. [10] (see page 129).

and is currently limited by the dependence of the isotope fractionation correction on the particle size [161], as shown in Figure 5.2. Such analyses are normally performed using the micro-probe (MP) analysis mode, which allows for the analysis of only a select number of particles.

The LG-SIMS also allows the rapid analysis of all particles present on the sample, which, in turn, increases the detection probability of non-conforming particles. Although the measurement accuracy of such rapid screening measurements is lower than the micro-probe analysis of single particles, the LG-SIMS automated particle measurement (APM) could even provide information regarding the minor isotope ratios of a very large number of particles, which could be of importance towards the detection of non-conforming particles. The detection of particles based on the minor isotope ratio does, however, require deep understanding of the analytical measurement procedure and knowledge on the capability of the LG-SIMS APM to discriminate different particles [162].

Due to the increased accuracy of single particle analysis and the increased capability to detect non-conforming particles during screening, there is a need for dedicated materials which can be used to optimize and verify the method (Figure 5.3). On the one hand, particles with a wide spread of particle size, i.e. polydisperse particles, would be required to reflect real-world samples and can be used for selectivity investigations. On the other hand, monodisperse particles with a well-defined geometry and especially number of atoms would be required for more accurate calibrations and mass bias corrections, eventually leading to the decrease of the measurement uncertainty. Both these classes would need to consist of a single isotopic composition free of cross-contaminations, to prevent incorrect conclusions due to, for example, the simultaneous measurement of two different particles. Particles consisting of a polydisperse particle size distribution and a single isotopic composition were produced in the framework of

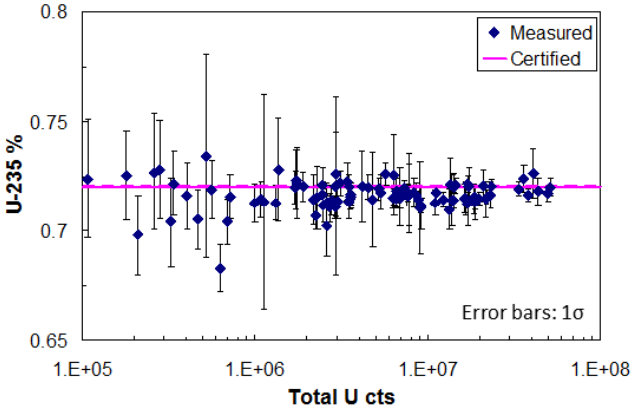

Figure 5.2: Measured $^{235}U/^{238}U$ isotope ratio of a powdered CRM by LG-SIMS. Reprinted from Sangély et al. [161].

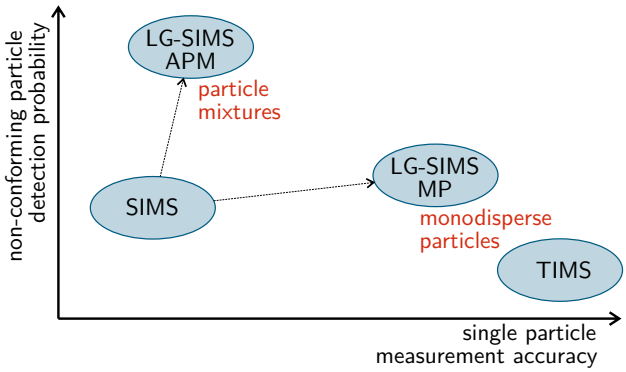

Figure 5.3: Needs of quality control particles for nuclear safeguards.

the NUSIMEP-6 [23] and NUSIMEP-7 [24] interlaboratory comparison. Monodisperse particles with a known isotopic composition are, however, not commonly available.

Other than particles consisting of a single isotopic composition, mixtures of particles with different isotopic compositions would be needed to improve the detection capability of non-conforming particles. To improve the instrument settings and quantify the detection probability for different types of particles, mixtures of monodisperse particles would be needed, whereas for method validation mixtures of polydisperse particles would be of relevance. A mixture of polydisperse particles was produced and distributed as part of the NUSIMEP-7 interlaboratory comparison whereas mixtures of monodisperse particles are not readily available. Apart from the synthetic samples, real-life reflecting samples would be required to further investigate the selectivity of the method. Such samples would need to consist of cotton swipes, which are typically used for sample collection, containing a mixture of well-defined particles and dust, masking the particles. To date, no such samples are available.

5.1.2 Property Values and Homogeneity

The particles produced in this work represent ideal test objects due to the high degree of homogeneity between all particles with respect to a number of properties, such as the size, morphology, chemical composition and structure. Therefore, the suitability to use the produced particles as standards for microanalytical applications was investigated, especially for usage as certified reference materials for nuclear safeguards, with the uranium isotopic composition and the uranium content of individual particles as property values. A certified reference material, in accordance to ISO 17034:2016, does not only need well characterized property values, but also a given uncertainty, including contribution due to instability and inhomogeneity of the property values. Therefore, possible sources of inhomogeneity and instability need to be identified during

the production stage already.

The uranium isotopic composition can be assumed to be highly stable and homogeneous for all produced particles on physical grounds. For the uranium content, however, there are a number of sources introducing inhomogeneity between particles and samples. Between individual particles, some inhomogeneity due to particles containing double the amount of uranium, particle agglomerates and broken particles is likely. With optimal production parameters, the fraction of such particles could be kept minimal (section 4.1), although some inhomogeneity could not be excluded. The inhomogeneity between particles due to drifts or changes in the uranium content ($w(\mathrm{U})_\mathrm{f}$) or density (ρ_f) of the liquid feed, the oscillating frequency (f) and the liquid feed rate (Q_V) are highly unlikely. Between multiple substrates, inhomogeneity of the uranium content could occur due to slight drifts of the liquid feed rate, which has been verified in section 5.2.2. The main source of inhomogeneity is, however, expected to occur between various production runs. With the present system, the number of samples which can be produced within a single production run is limited by the liquid feed solution reservoir, and allows for the production of roughly 60 samples. To refill the reservoir, the liquid jet needs to be interrupted. A change of the liquid feed flow rate between various jets is considered to be likely which, in turn, leads to a between-run inhomogeneity. A schematic overview of the described types of inhomogeneities are given in Figure 5.4.

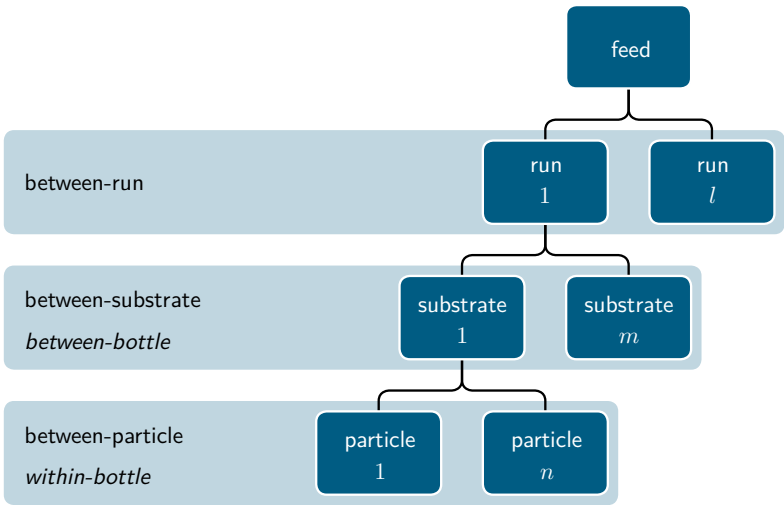

Figure 5.4: Overview of typical particle production series to produce m samples, each containing n particles with a constant isotopic composition and uranium content, requiring l production runs, where $n \approx 20\,000$ and $m \leq 50$.

5.2 Characterization of Property Values

5.2.1 Uranium Isotopic Composition

The uranium isotopic composition is intended to be one of the certified property values. The isotopic composition of the particles is expected to be similar to the composition of the liquid feed solution, which is typically produced by dilution of a certified reference material. Although the conservation of the isotopic composition of microparticles produced by a spray-pyrolysis was previously confirmed for a similar process [73, 74, 77], a number of batches produced within this project were analyzed to verify the obtained isotopic composition.

The first batch analyzed consisted of particles produced from a depleted uranium (DU) certified reference material. The particles were analyzed by LG-SIMS (IAEA/SAL) and a good agreement between the expected and measured isotopic composition was found (see Knott [109]), from which was concluded that no significant cross-contamination occurred during preparation of the liquid feed solution.

A second set of samples was produced from a low-enriched uranium (LEU) UF_6 certified reference material, which was first hydrolyzed and dissolved in concentrated nitric acid (JRC-Geel (formerly JRC-IRMM)) and subsequently dried and redissolved in dilute nitric acid to obtain a solution with a $n(NO_3)/n(U)$ ratio around 10. The produced particles were analyzed by LG-SIMS (IAEA/SAL and JRC-Karlsruhe (formerly JRC-ITU)). The results showed good agreement of the isotopic composition of the investigated particles with the initial CRM, indicating no cross-contaminations during the preparation of the liquid feed solution occurred. However,

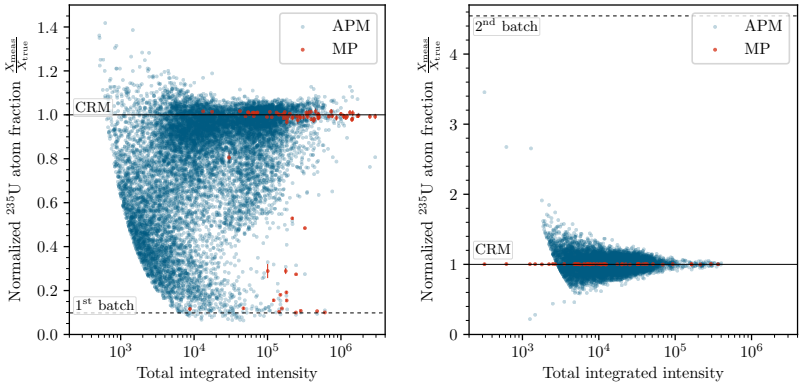

(a) Second batch **(b)** Third batch

Figure 5.5: LG-SIMS analysis (IAEA/SAL) of (a) LEU particles after production of DU particles and (b) NU particles after thorough cleaning of the system. The shown ^{235}U isotope amount fractions have been normalized to the certified value of the used CRM. APM: Automated particle measurement; MP: Micro-probe analysis.

a large number of particles consisting of depleted uranium were found (Figure 5.5a). Such particles are likely to be remnants of previous production batches.

To minimize such memory effects, the system was thoroughly cleaned and a number of critical parts were replaced. Afterwards, a third set of particles was prepared from a certified reference material with an isotopic composition different from all previous productions. The CRM, consisting of U_3O_8, was dissolved in concentrated nitric acid, followed by drying and dissolution in dilute nitric acid. The produced particles were analyzed by LG-SIMS (IAEA/SAL), where the analysis results did not show any traces of particles other than expected particles (Figure 5.5b), confirming that particles could be produced free from any cross-contaminations and memory effects.

5.2.2 Uranium Content

The second intended property value is the uranium content, i.e. the total number of atoms contained within a single particle. Analysis of the uranium content of single particles is complicated by the lack of established procedures and comparable standards. The uranium content of microparticles was previously quantified by ID-TIMS by Kraiem et al. [77] and Ranebo et al. [76], who reported a uranium content with a relative uncertainty around $3\,\%$. Within this work, no measurements have yet been undertaken to measure the uranium content. However, the production of microparticles by the spray-pyrolysis of an aerosol, generated using a vibrating orifice aerosol generator does allow the calculation of the uranium content within a single droplet, and therefore single particle, as described in section 3.1.

For the calculation of the uranium content, the density (ρ_s) and uranium content ($w(\mathrm{U})$) of the liquid feed solution, the oscillating frequency (f) and the liquid feed flow rate (Q_V) are required (equation 3.4). Of these parameters, the frequency was verified using an oscilloscope, the uranium content of the liquid feed solution is typically measured by ICP-MS and the solution density is determined by gravimetric weighing of volumetrically transferred aliquots. The liquid feed flow rate is, however, set using a syringe pump for which the volume flow rate has been given by the operation manual [163] as function of the pump speed.

In order to verify the liquid flow rate, a liquid jet was started and collected in a vial placed directly below the orifice. Although the flow rate could be estimated by gravimetric determination of the collected aliquot ($m(\mathsf{collected})$) and the collection time (t),

$$Q_\mathsf{V} = \frac{m(\mathsf{collected})}{\rho_\mathsf{s} \cdot t}, \tag{5.1}$$

possible evaporation of the solvent during collection might lead to a negative bias of the volume flow rate. Therefore, the collected aliquot was diluted gravimetrically, after which the uranium content of the diluted sample was measured by ICP-MS ($w(\mathrm{U})_\mathsf{meas}$). Based on the dilution factor F, the total amount of uranium collected in time t could be calculated, from which the

uranium flow rate ($Q(\mathrm{U})$) could be calculated,

$$Q(\mathrm{U}) = \frac{w(\mathrm{U})_{\mathrm{meas}} \cdot F}{t}. \tag{5.2}$$

The volume flow rate Q_{V} can be obtained by dividing the uranium flow rate with the uranium content of the liquid feed solution ($w(\mathrm{U})$) and the solution density ρ_{s},

$$Q_{\mathrm{V}} = \frac{Q(\mathrm{U})}{\rho_{\mathrm{s}} \cdot w(\mathrm{U})}. \tag{5.3}$$

Comparison of the calculated volume flow rate based on the gravimetric determination and the ICP-MS measurement shows a negative bias for the gravimetric determination (Figure 5.6), which is presumably caused by the evaporation of the solvent during collection.

The volume flow rate was determined for three separate runs, were for each run a different solution and syringe were used. In total, 20 samples were collected, with collection times ranging from 1.4 to 60 minutes. Figure 5.7 shows the determined volume flow rate as function of the collection time. The results show a good stability of the volume flow rate, both as function of the collection time, between different collections and between different runs. The results therefore indicate that both the between-substrate and between-run inhomogeneity (Figure 5.4) due to drifts of the volume flow rate are unlikely to occur. The mean volume flow rate of 2.59(12) µl s^{-1} does, however, differ significantly from the volume flow rate given

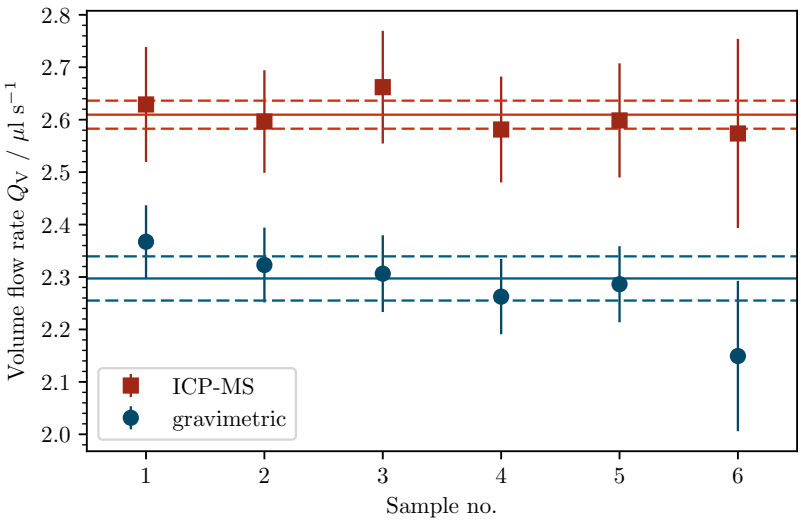

Figure 5.6: Volume flow rate determined by gravimetric analysis and ICP-MS quantification.

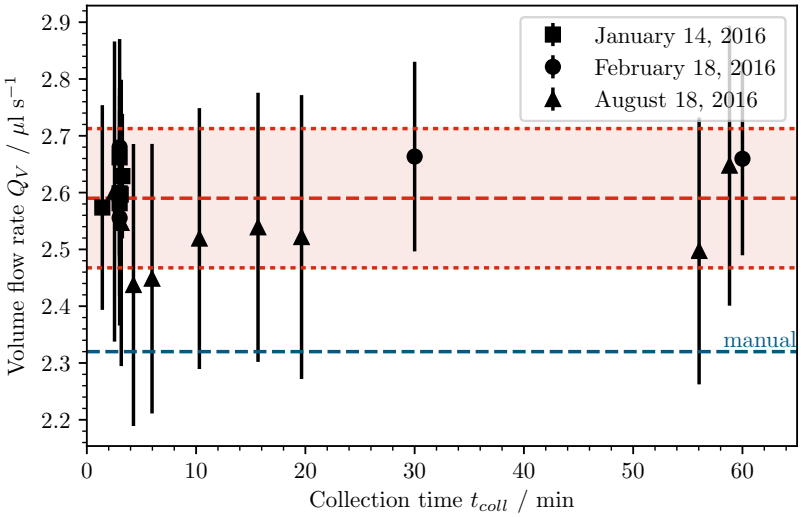

Figure 5.7: Determined volume flow rates for three independent analysis sequences with varying collection times.

in the operation manual [163] and shows the importance of the flow rate determination.

The volume flow rate remains constant as long as the pump drive speed and syringe diameter remain constant, which allows the usage of the volume flow rate without further validation. However, combining equation 5.2, equation 5.3 and equation 3.4 results in equation 5.4, which can be used to calculate the total amount of uranium present in a single droplet based only on the measured uranium flow rate and the oscillating frequency.

$$m(\mathrm{U})_\mathrm{d} = \frac{Q(\mathrm{U})}{f} \tag{5.4}$$

As the main contribution to the combined uncertainty of the uranium content using equation 3.4 originates from the solution density (ρ_s) and the volume flow rate (Q_V), the quantification of the uranium content using equation 5.4 results in a strongly reduced combined uncertainty. Therefore, the usage of the uranium flow rate results in a more accurate estimation of the uranium content of a single microparticle, although the uranium flow rate needs to be determined for each production.

As an example, the uranium content of particles produced prior to one of the flow rate determinations was calculated. The particles were produced from a uranyl nitrate solution with a uranium content of 77.1(42) µg g^{-1}, a density of 936(32) kg m^{-3} and an oscillating frequency of 69.10 kHz. By using equation 3.4, a uranium content of 2.70(21) pg was calculated, which corresponds to a relative uncertainty ($k = 1$) of 4.0 %. By using the determined uranium flow

rate of 189.2(20) µg s^{-1} and equation 5.4, a uranium content of 2.738(62) pg was calculated, which corresponds to a combined uncertainty of 0.53 % ($k = 1$). The various mean values were calculated using the DerSimonian-Laird method [164–166], which uses the Graybill-Deal estimator [167] and adds an excess variance to correct for unknown effects. Even though, the uncertainty calculations have not been validated and might underestimate the calculated combined uncertainty.

5.3 Particle Suspensions

One method to eliminate any possible between-run inhomogeneity is to transfer the produced particles into a suspension, as the previous studies (section 4.3) have shown the particles to be stable in such suspensions for hundreds of days. Once transferred into such suspensions, both the between-run and between-substrate homogeneity are expected to be combined into a slightly increased between-particle inhomogeneity. Although the stability of the particles was demonstrated for up to 202 days, the intended shelf-life of the particles is much longer due to which a transfer into a more stable state would be preferential. Therefore, the produced particles suspensions are dried onto solid substrates, such as glass-like carbon disks, before certification.

The drying of colloidal droplets onto solid substrates commonly leads, however, to the formation of rings containing the solid material due to the Marangoni effect. Deegan et al. [168] investigated this effect and concluded that the formation of such deposition rings is due to the mass transfer of the solution towards the contact line, i.e. the solution/substrate/gas interface. For droplets free of solids, the evaporation of the solution leads to a continuous movement of the contact line. However, the movement of the contact line is hindered by solid objects deposited onto the substrate. Due to mass conservation, a mass transfer of the solution towards the contact line occurs, which causes the increase of colloid concentration near the contact line.

In the case of particle suspensions, particles also undergo settling due to the gravitational force. The velocity at which particles are settled V_s in a solution with density ρ_s and viscosity μ_s is calculated using equation 5.5, in which ρ_p and d_p are the particle density and diameter, respectively, and g is the gravitational constant.

$$V_\mathrm{s} = g\frac{2}{9}\frac{\rho_\mathrm{p} - \rho_\mathrm{s}}{\mu_\mathrm{s}}\left(\frac{d_\mathrm{p}}{2}\right)^2 \tag{5.5}$$

Once the particles are in close vicinity of the substrate, van der Waals forces between the particle and substrate [169] prevents the particle from being detached due to the solutions mass flow.

The combination of the different forces acting on the particles during drying of suspensions could affect the deposition pattern of the particles. Upon addition of the suspension onto

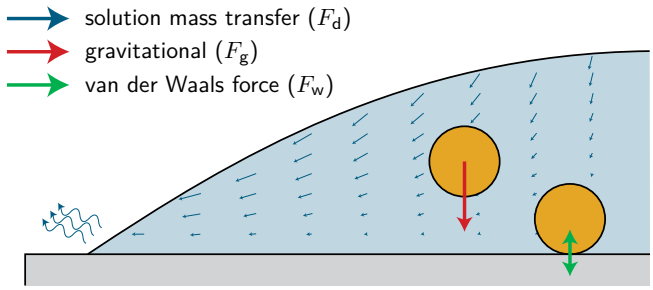

Figure 5.8: Circulation pattern in droplets contacted with a solid substrate due to the evaporation of the solvent.

the substrate, the particles can be assumed to be homogeneously distributed throughout the suspension. Due to the gravitational forces (F_g), the particles start moving towards the substrate. Upon evaporation of the solution, the solution mass flow (F_d) does, however, cause the particles to move towards the contact line. The force of the mass flow depends on the evaporation rate ($R_{evaporation}$) of the solution which, in turn, depends on the temperature applied ($F_d \propto R_{evaporation} \propto T$); with higher temperatures the solution mass flow is stronger than at low temperatures. Therefore, the number of particles deposited at the contact line and eventually the formation of deposition rings is expected to be more pronounced at higher drying temperatures.

Once in close proximity to the substrate, the particles are bound to the substrate due to van der Waals forces. However, if a high treatment temperature is applied, the solution mass flow might be stronger than the van der Waals forces, causing the detachment of the particles, which are then transferred towards the contact line. A schematic overview of the different forces is shown in Figure 5.8, where the solution mass flow force F_d is expected to increase with increasing drying temperature.

Based on the described theories, a low drying temperature would be important to achieve homogeneous distributions of the particles over the substrates. To demonstrate the possibility to obtain homogeneous distributions, 400 µl of a particle suspensions in ethanol was added drop-wise to a glass-like carbon disks, which was placed onto a heating plate set to 50 °C. Although the actual temperature at the surface of the substrate is unknown, drying occurred within a few minutes and a highly homogeneous particle distribution was obtained, as is shown in Figure 5.9b. Figure 5.9a also shows the particle distribution of the same particles collected directly onto a glass-like carbon disk using the single-stage inertial impactor. The highly inhomogeneous distribution obtained expresses the advantage of particle suspensions compared to direct collection.

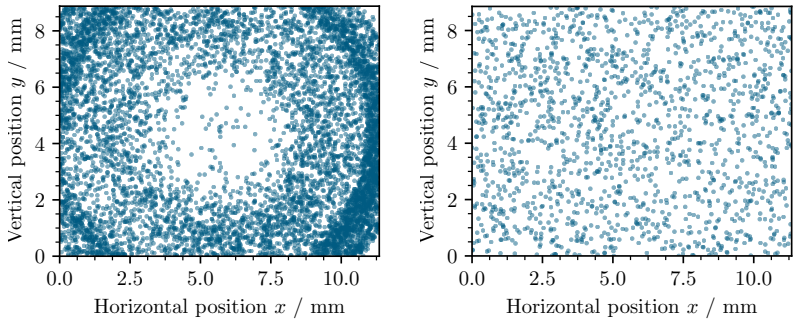

(a) Direct collection **(b)** Suspension

Figure 5.9: Distribution of particles onto a glass-like carbon disk obtained by (a) direct collection and by (b) drying of an ethanol suspension. Reprinted from Middendorp et al. [160].

5.3.1 Mixed Particle Samples

The particle suspensions also offer additional advantages towards the production of quality control standards for microanalytical applications, such as the possibility to produce particle mixtures. The production of particle mixtures can be achieved by mixing suspensions containing different types of particles, where all types of particles could be mixed as long as the particles do not interact with the used medium (ethanol).

To demonstrate the possibility to produce such particle mixtures, both uranium and cerium particles were produced which were subsequently transferred into suspensions. The produced suspensions were mixed in two different volumetric ratios to produce particle mixtures. Aliquots of the mixed suspensions were dried onto silicon wafers and subsequently analyzed by SEM/EDX. To discriminate between uranium and cerium particles, the total measured intensity of uranium (3.0 keV to 3.5 keV) and cerium (4.5 keV to 6.0 keV) in the EDX spectra was integrated and particles were classified as uranium or cerium particle based on the measured intensities; only a single mixed uranium/cerium was found. The total number of uranium and cerium particles were counted for each produced sample and are shown in Table VI and spatially distributed in Figure 5.10.

In the first sample, in which the uranium and cerium suspensions were mixed in equal volume ratios, an excess of cerium particles was found, showing that the cerium particle suspensions contains roughly six times as many particles as the uranium particle suspension. The second sample prepared, to which four times the volume of cerium suspension was added, also shows a four-fold increase of the cerium to uranium particle ratio. Although the particle concentration in these suspensions was not determined before mixing, these results show that the production of particles mixtures in specific ratios is possible. However, further investigations towards the

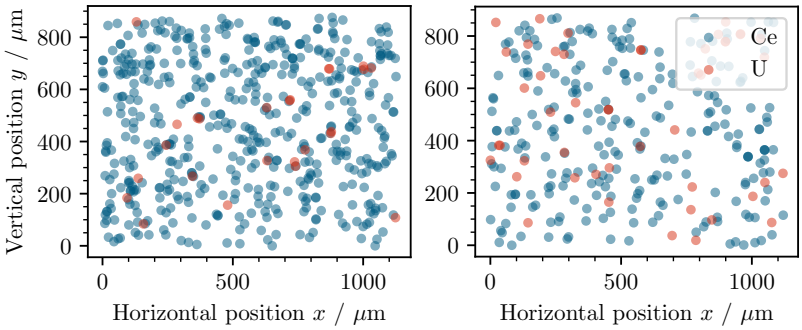

Figure 5.10: Cerium (blue) and uranium (red) particles deposited onto a substrate from two different (1:4 and 1:1) mixed uranium/cerium particle suspension.

quantification of the particle concentration, for example using dynamic light scattering (DLS), would be required.

5.3.2 Real-life Samples

The demonstrated application of particle suspensions has focused on the distribution of aliquots onto solid substrate suitable for direct analysis. The particle suspensions do, however, also allow to prepare different types of samples, which can be used to verify a wider range of the analytical procedure. As an example, a mixed uranium and cerium particle suspension was added drop-wise to a small piece of cotton swipe, which was gently heated to evaporate the solvent. The drying of the suspensions onto such swipes requires less stringent conditions as no homogeneous deposition is possible due to the inhomogeneous substrate.

The prepared swipe sample was mounted onto a aluminum holder which was investigated by SEM/EDX in low vacuum mode. The SEM/EDX analysis was complicated by the highly irregular surface of the fibers and the degradation of the fibers under the electron beam. Even though, particles could be discerned (Figure 5.11) and EDX analysis showed a homogeneous mixture of both cerium and uranium particles, with a cerium to uranium particle ratio similar to the ratios obtained for solid flat substrates (Table VI). These results show that the produced particle suspensions can also be used to prepare swipe samples impregnated with particles

Table VI: Uranium and cerium particles counted in mixed particle suspensions

Sample (U:Ce)	N(U)	N(Ce)	N(Ce)/N(U)
Si wafer (1:1)	42	256	6.1
Si wafer (1:4)	23	506	22
Swipe (1:1)	122	666	5.5

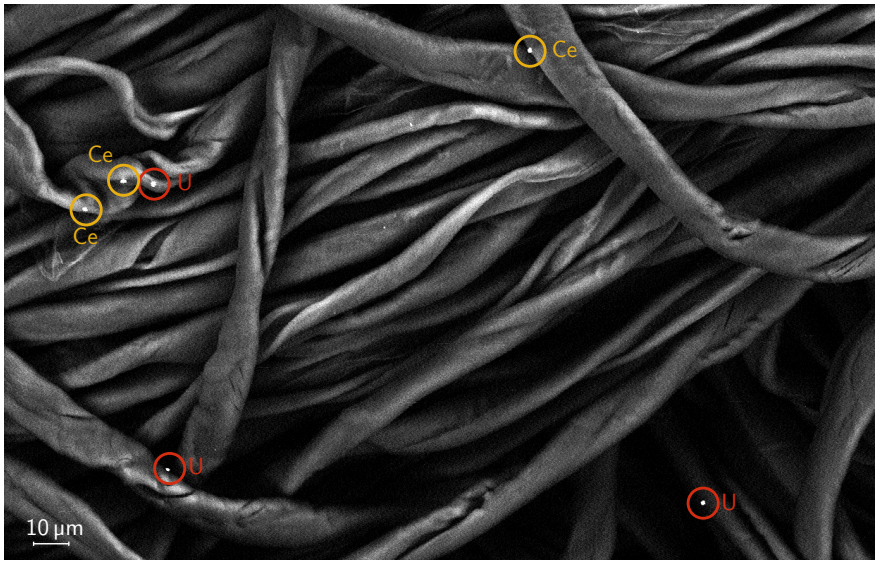

Figure 5.11: Collected SEM/BSED micrograph of uranium and cerium particles deposited onto a piece of cotton swipe. Adapted from Middendorp et al. [160].

which, in turn, could be used to validate the particle transfer from collected swipe samples onto the measurement substrates.

5.4 Standards for Nuclear Forensics

Other than the uranium isotopic composition and content, the produced particles exhibit a number of constant, well-defined properties, which could be of interest towards other fields employing microanalytical characterization techniques. One such property was demonstrated within the μ-Raman studies performed within this work, were previous characterization using μ-XRD and μ-XANES allowed the particles to be used as standards to confirm previous findings. Another property which could be of interest for other microanalytical application is the inclusion of other elements, often described as impurities, within the particles. Within this work, particles were produced consisting of a homogeneous mixture of uranium and cerium(IV). Cerium(IV) is often used as surrogate for tetravalent actinoids, such as thorium(IV) and plutonium(IV), due to the comparable oxidation state and radius. As the produced particles consisted of a highly homogeneous mixture of uranium and cerium, it can be assumed that the production of uranium and thorium or uranium and plutonium will also yield highly homogeneous particles. Also, the inclusion of rare-earth elements within uranium materials is of interest for nuclear forensics, as the ratio of rare-earth elements within a uranium material can be used to determine the origin of the material [170–173]. Although only a single rare-earth element was included

within this work, the chemical similarity of all rare-earth elements would make the production of uranium particles containing specific mixtures of multiple rare-earth elements likely to be possible.

Another method employed in nuclear forensics and also in a more generic forensics is the isotopic analysis of oxygen. Due to atmospheric conditions, the $^{16}O/^{18}O$ ratio is known to differ world-wide and is therefore used for geolocalization of unknown samples [174]. A select number of studies have been performed on various uranium oxides [175–180], although typically bulk amount of material were investigated which were not characterized beforehand. The oxygen isotope ratio of the uranium oxides is, however, influenced by various processes within the nuclear fuel cycle, as shown schematically in Figure 5.12. Although these processes will reduce the information value obtained from analyzing the $^{16}O/^{18}O$ ratio in the material found in various steps of the fuel cycle, it could also act as a valuable tool to locate a number of processing facilities.

The nuclear fuel cycle is typically described starting with the mining of the ore. Although a number of processes exists to extract the ore and the uranium from the ore, the obtained product is commonly classified as yellow cake, which is a general term and might include a large variety of compounds, all of which contain oxygen which is likely to consists of the isotopic composition traceable to the origin of the ore. The localization of the mining stage can, however, also be performed by measurement of the rare-earth elemental ratios.

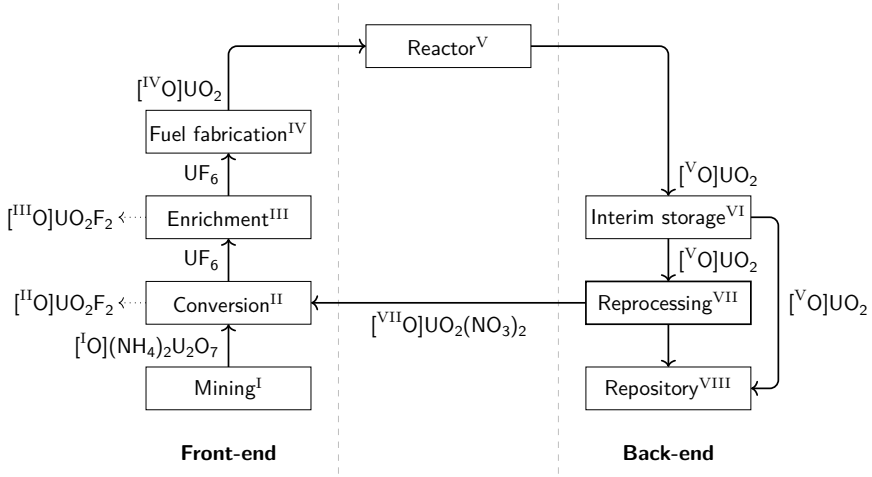

Figure 5.12: Oxygen isotope ratio of the various products in the nuclear fuel cycle with the relationship to the geographical location of the processing facilities.

During the next stage, the yellow cake is further purified and finally converted into uranium hexafluoride, e.g.

$$\begin{aligned} UO_2 + 4\,HF &\longrightarrow UF_4 + 2\,H_2O \\ UF_4 + F_2 &\longrightarrow UF_6 \end{aligned}$$

During the conversion of the UO_2 to UF_4 all original oxygen is removed, eliminating all information regarding the mining. However, during all handling processes, small microparticles are expected to be released. Upon contact of a released UF_6 microparticle with moisture in the ambient air, the UF_6 is rapidly hydrolyzed, resulting in the formation of a UO_2F_2 microparticles with an oxygen isotope ratio similar to the conversion facility:

$$UF_6 + H_2O \longrightarrow UO_2F_2 + 2\,HF$$

The produced UF_6 is transported to an enrichment facility, where the uranium is enriched. Although no chemical conversion occurs, released and hydrolyzed UO_2F_2 microparticles could be identified to stem from either the conversion or enrichment facility based on other particle properties, such as the enrichment.

During the next stage of the fuel cycle, the enriched UF_6 is hydrolyzed with water to form UO_2F_2 which is subsequently thermally decomposed to form UO_2. The obtained UO_2 is then pressed into pellets which are used as nuclear fuels. The produced fuel elements therefore provide information regarding the fuel manufacturing facility.

During the irradiation with thermal neutrons within a nuclear reactor, the oxygen undergoes various nuclear reactions, both producing and consuming various isotopes of oxygen. Due to the complex and inhomogeneous distribution of neutrons within the reactor core, essentially all information contained in the oxygen isotopic composition is eliminated and, in the case of an open fuel cycle, does not provide any further information. In a closed fuel cycle, however, the irradiated fuel is dissolved in a large volume dilute nitric acid.

$$UO_2 + 2\,HNO_3 \rightleftharpoons UO_2^{2+} + 2\,NO_3^- + 2\,H^+$$

Especially due to the high temperature of the solution, exchange of oxygen between the uranyl ion and nitrate and between the uranyl ion and water is likely to occur [145, 148, 181–183], which can be described in a general form as:

$$\begin{aligned} [^x\mathrm{O}]UO_2^{2+} + 2\,[^y\mathrm{O}]NO_3^- &\rightleftharpoons [^y\mathrm{O}]UO_2^{2+} + 2\,[^x\mathrm{O}]NO_3^- \\ [^x\mathrm{O}]UO_2^{2+} + 2\,[^y\mathrm{O}]H_2O &\rightleftharpoons [^y\mathrm{O}]UO_2^{2+} + 2\,[^x\mathrm{O}]H_2O \end{aligned}$$

where $^x\mathrm{O}$ is the oxygen isotope ratio of the spent fuel whereas $^y\mathrm{O}$ is the oxygen isotope ratio of the solvent, i.e. representative for the reprocessing facility. Due to the large excess of

^{y}O compared to ^{x}O, the obtained uranyl nitrate is likely to contain oxygen with an isotopic composition traceable to the enrichment facility.

The oxygen isotope ratio of the particles produced within this work could stem from three sources; the original uranyl nitrate, the water and ethanol used for dilution and the air in which the particles are treated. If the production of particles would be performed in an inert atmosphere, no ethanol would be added and either uranyl nitrate is dissolved in isotopically spiked water or an oxygen-free uranium compound is converted with isotopically labeled nitric acid, the oxygen isotope ratio would be adjustable and such particles could be used to evaluate the possibility to accurately analyze the oxygen isotope ratio.

Although the oxygen isotope ratio of the produced particles in this work is unknown, the developed process could be used to produce particles with a known isotope ratio. Therefore, a liquid feed solution with a known isotope ratio would be required. Although such materials are not available in the form of (certified) reference materials, solutions could be made either by chemically reaction oxygen-free uranium compounds with water with a known isotopic composition (e.g. hydrolysis of UF_6) or by isotope exchange between dried uranyl nitrate with isotopically labeled water. Although the latter method would not produce solutions with a known composition, a separate analysis of the ratio within the solution would provide an informative value. To prevent further cross-contaminations, the liquid feed solution should not be diluted with ethanol and particles should be produced in an oxygen-free atmosphere.

A number of samples were produced from a uranyl nitrate solution spiked with ^{18}O. The particles were prepared in a nitrogen atmosphere. SEM investigations of the obtained particles (Figure 5.13a) shows a slightly lower degree of sphericity compared to regular particles, which is likely caused by the slower evaporation rate due to the absence of ethanol. Also, μ-Raman spectroscopic measurements were performed on the collected microparticles (Figure 5.13b). The collected spectra of five particles show two distinct types of particles. For two particles,

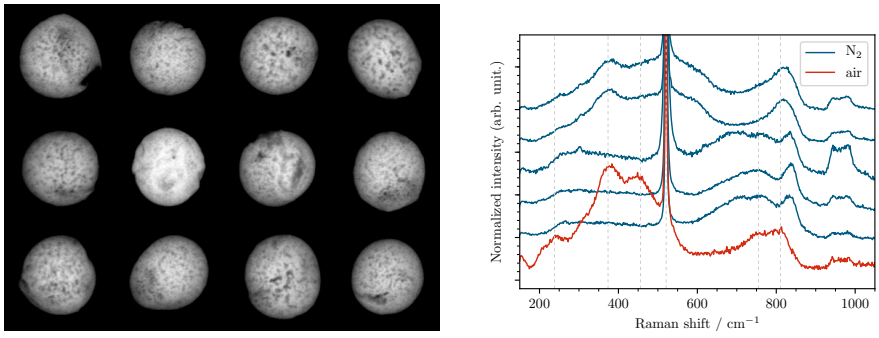

(a) SEM micrographs **(b)** μ-Raman spectra

Figure 5.13: SEM/BSED micrographs (a) and μ-Raman spectra (b) of microparticles produced from ethanol-free feed solutions in a nitrogen atmosphere.

spectra comparable to particles treated in an air atmosphere were obtained whereas three particles with slightly different spectra were obtained. μ-XRD measurements would be required to confirm the structure of particles produced in a nitrogen atmosphere.

First particles were deposited on silicon wafers, which were analyzed by ToF-SIMS. The formation of clusters of silicon during ablation does, however, hinder the measurement of the $[^{x}O^{y}U]$ complexes, e.g. $[^{30}Si_2{}^{28}Si_7]$ interferes with $[^{18}O^{238}U]$. Deposition of produced particles on other substrates free of oxygen should overcome such problems, such as the deposition of particles on gold.

6 Conclusion and Outlook

6.1 Conclusion

Within this study, the production of spherical, micrometer-sized uranium oxide particles was investigated with the aim to produce quality control materials for nuclear safeguards. Particles were produced by spray-pyrolysis of a monodisperse aerosol generated using a vibrating orifice aerosol generator. The first part of this work focused on the characterization of the particle formation process, leading to an optimized particle production process, which is capable of producing particles with a monodisperse particle size distribution. In the second part, the obtained particles were further investigated using microanalytical techniques to determine the crystal structure of the obtained particles, which is of importance to assess the stability of the produced particles. The stability of the obtained particles was investigated in liquid media, as the transfer of produced particles into particle suspensions could be used to improve the homogeneity. Finally, the suitability of the obtained particles for usage as quality control material and certified reference material was investigated.

Process Characterization. The first part of this project focused on the particle formation process leading to the formation of solid particles. Monodisperse aerosols were generated using a vibrating orifice aerosol generator from uranyl chloride, uranyl acetate and uranyl nitrate precursor solutions. The aerosols were treated at different temperatures, up to 600 °C, and the obtained particles were investigated by combined SEM/EDX studies to investigate the particle formation process.

Although particles produced from uranyl chloride precursor solutions showed highly irregular shapes and are not suitable as candidate reference materials, the transformation from uranyl chloride droplet into solid uranyl chloride particles and finally into uranium oxide particles could be followed by SEM/EDX studies. The particle formation process was shown to commence with instantaneous precipitation of the uranyl chloride upon reaching the saturation limit, forming porous uranyl chloride precursor particles. The thermal decomposition of the precursor particles is proceeded by melting of the uranyl chloride, which leads to a densification of the particle surface and hinders the evacuation of the released gaseous decomposition products, which, in turn, leads to the formation of large voids within the particles.

The formation of solid particles from uranyl acetate containing aerosols was found to proceed different from uranyl chloride and resulted in highly spherical and monodisperse microparticles

with homogeneously distributed nanopores. The transformation of droplets into uranyl acetate particles was found to proceed via progressive precipitation with diffusion. The chemical decomposition of the uranyl acetate into the uranium oxide phase could only be observed by a slight densification of the particles, although the absence of large and heterogeneously distributed pores indicate that no melting occurs prior to decomposition.

Similar studies using uranyl nitrate also resulted into spherical microparticles, although the precipitation appears to proceed instantaneously, resulting in the formation of porous precursor particles. Similar to particles produced from uranyl chloride, melting prior to chemical decomposition is likely to occur resulting in the formation of a dense shell around a more porous core. The anion to cation ratio of the precursor solution was found to be a critical factor influencing the final particle morphology; a high ratio leads to the formation of a large volume of nitrous gasses and eventually leads to the fracturing or inflation of the particles. Under controlled circumstances, monodisperse particles could be obtained with a relative density around previously reported densities for microparticles. Moreover, based on the systematic analysis of the particle formation process at different thermal treatment temperatures, particles could be produced in a consistent and reproducible manner. The detailed insights gained in this work provide the basis to establish the aerosol-based production as a method for producing a wide range of different uranium particle reference materials.Although particles were obtained from all investigated precursor compounds, uranyl acetate was found to be unsuitable to produce candidate CRM particles.

Structural Investigations. The decomposed microparticles produced from uranyl nitrate were investigated by μ-XRD, μ-XANES and μ-Raman spectroscopy to obtain information regarding the chemical composition. Both μ-XRD and μ-XANES showed that the particles consist of an orthorhombic triuranium octoxide phase, even at temperatures as low as 400 °C. The decomposition of uranyl nitrate typically leads to the formation of uranium trioxide which decomposes into triuranium octoxide at temperatures in excess of 580 °C. The low temperature of 400 °C in this work at which the triuranium octoxide phase was found shows the difference between milligram ("bulk") amounts of materials compared to individual microparticles (picogram amounts). μ-Raman measurements performed on the produced microparticles indicate the formation of a thin layer of uranyl hydroxide at the surface of the particles.

Particles produced from uranyl acetate were also investigated by μ-XRD, μ-XANES and μ-Raman spectroscopy, which also resulted in the orthorhombic triuranium octoxide phase with a thin uranyl hydroxide surface layer, similar to particles produced from uranyl nitrate. Particles from uranyl chloride were only investigated by μ-Raman spectroscopy, which showed similar results compared to particles produced using uranyl nitrate and uranyl acetate. The obtained results show that there is no difference in structural properties between particles produced from uranyl nitrate and uranyl acetate. As uranyl nitrate is more readily available and obtained compared to uranyl acetate, conversion of uranyl nitrate solutions to uranyl acetate does not

provide benefits towards the production of monodisperse microparticle reference materials.

Particles consisting of a mixture of uranium and cerium showed a phase transformation from an orthorhombic phase into a cubic phase with an increasing amount of cerium. The irreversible phase transformation was observed during irradiation with a laser, indicating that the cubic phase is thermodynamically more stable compared to the orthorhombic phase although it has a relatively high activation energy, which decreases with an increasing cerium content. It is worth noting that μ-XRD and μ-Raman are very powerful techniques, allowing measurements on individual particles and thereby provide valuable information regarding the homogeneity of the structural composition of numerous individual particles.

Solid-Liquid Interactions. The stability of microparticles produced from uranyl nitrate solutions was investigated in various liquid media. Of the different media investigated, ethanol was found most suitable for storage and handling of particles. Extended dissolution studies showed no visual signs of dissolution after 432 days whereas quantitative measurements of the supernatant solution showed no significant dissolution of the particles after 228 days.

The exchange of uranium isotopes between milligram amounts of solid triuranium octoxide and uranium saturated water and ethanol was investigated. In water, significant exchange was observed following first-order kinetics and an activation energy of $34.7(29)\,\mathrm{kJ\,mol^{-1}}$ was determined. Based on further investigations, the exchange of uranium between both phases is assumed to proceed via the formation of a uranyl hydroxide phase, which was found to be formed on the surface of the particles by μ-Raman spectroscopy.

Similar studies in ethanol did not show exchange between solid triuranium octoxide and uranium dissolved in ethanol. Also, isotope exchange studies between depleted and low-enriched uranium microparticles in ethanol showed no signs of between-particle isotope exchange for up to 202 days.

The obtained results demonstrate that particles produced from uranyl nitrate are suitable to be stored in ethanol for up to a few hundred of days without undergoing significant alteration, which make the processing of particles via a suspension a suitable step with regard to the particle stability.

Application as Particle Reference Material. Based on the previous results, triuranium octoxide microparticles with a monodisperse particle size distribution could be prepared. The uranium isotopic composition of individual microparticles was found to be in agreement with the uranium isotopic composition of the initially used certified reference material and, after thorough cleaning, no cross-contaminations and/or memory-effects were found. The uranium content of single microparticles can be calculated using the operation settings of the vibrating orifice aerosol generator. A method was developed to measure the uranium flow rate, from which the uranium content could be estimated with a relative uncertainty around 3 %.

Microparticle suspensions were shown to increase the between-particle homogeneity and open new possibilities towards advanced samples for quality control purposes, such as particle mixtures or the deposition of microparticles onto cotton swipes. As the stability studies showed that the produced particles remain stable in suspensions for several hundreds of days, processing of particle via suspensions has been shown to be a valuable tool for further handling, especially since the handling typically takes a few hours.

The results obtained within this project led to a detailed understanding of the particle production process and spherical microparticles consisting of triuranium octoxide with a known uranium isotopic composition and uranium mass could be prepared. The successfulness of the established process was demonstrated by the production of particles from a tailor-made (JRC-Geel (formerly JRC-IRMM)) uranyl nitrate solution. A large amount of particles were collected onto quartz disks during two consecutive days, after which the particles were transferred into a 100 ml ethanol suspension. The suspension was distributed over 110 glass-like carbon disks, which are being certified in accordance to the ISO 17034:2016 with respect to the uranium isotopic composition and the uranium content, and are planned to be released as a certified reference material (IRMM-2329P). Additionally, the produced samples are planned to be used during the NUSIMEP-9 round-robin exercise.

6.2 Outlook

The microparticles produced within this work represent ideal test objects for microanalytical applications and are currently being characterized towards certification as certified reference material. The established method does, however, allow the production of particle standards for microanalytical applications other than safeguards.

First studies were performed to produce microparticles with defined oxygen isotope ratios. Although measurements of the produced particles were unsuccessful, further studies and measurements of such particles could provide a valueable tool for nuclear forensics to determine the location of various material processing stages of intercepted material [175–178]. Another method used for geolocalization is the measurement of the rare-earth elemental distribution in uranium samples [173, 184, 185]. As particles consisting of a highly homogeneous mixture of uranium and cerium were produced within this work, extensions of the particle production including all rare-earth elements with specified amounts and distributions could act as a valuable tool for nuclear forensics. Due to the comparable chemical behavior of the rare-earth elements, production of such particles is deemed feasible with minimal further investment.

Particles consisting of mixture of uranium and rare-earth elements are also of interest towards the scientific understanding of the uranium-lanthanoid system at low quantities. As shown in this work, a phase transformation of an orthorhombic phase into a cubic phase was observed. μ-XANES measurements to determine the oxidation state of the cerium within such particles could provide information whether the phase transformation is accompanied by the reduction of the tetravalent cerium into trivalent cerium. Particles consisting of uranium and either tetravalent or trivalent elements, for example thorium and lanthanum, respectively, could be prepared for comparison with systems in which no oxidation/reduction occurs.

Such studies would eventually lead to a deeper understanding of the particle production process and would allow the production of particles consisting of a homogeneous mixture of uranium and plutonium, which is of high interest for particle reference materials in nuclear safeguards. Also, the chemical behavior of such particles is of interest towards the safety case of nuclear waste repositories, as the transport of radionuclides by colloids/particles was previously observed to be significant during various studies [186, 187].

One remaining question regarding the produced particles within this work is the internal morphology of microparticles produced using uranyl acetate. Although FIB/SEM studies show a relative dense particles, the determined density suggest that the particles consists of numerous nanopores, which can only barely be distinguished by FIB/SEM. TEM measurements of slices extracted from the particles could provide conclusive evidence on the presence of such nanopores.

With respect to the stability of particles in suspensions, further dissolution studies including studies of the internal morphology of the microparticles is of interest. To better understand the uranium isotope exchange studies, atom probe tomography (APT) measurements of partially

exchanged material extracted from the surface of the solid phase could provide detailed insight into the isotopic distribution within the solid phase. Such distribution measurements would provide a mean of gaining insight into fundamental solid-liquid interactions on the nanometer-scale, which would be interesting in wide range of material. Transmission electron microscopy (TEM) studies could provide information regarding the formation of the uranyl hydroxide layer and the thickness of such a layer. A combined APT/TEM study would provide detailed insight into the exchange mechanism occurring at the surface of the produced micrometer-sized particles.

List of Publications

Peer-Reviewed Publications

- R. Middendorp, M. Dürr, and D. Bosbach. The stability of uranium microspheres for future application as reference standard in analytical measurements. *Procedia Chemistry*, 21:285–292 (**2016**) doi:10.1016/j.proche.2016.10.040
- R. Middendorp, M. Dürr, A. Knott, F. Pointurier, D. Ferreira Sanchez, V. Samson, and D. Grolimund. Characterization of the Aerosol-Based Synthesis of Uranium Particles as a Potential Reference Material for Microanalytical Methods. *Analytical Chemistry*, 89(8):4721–4728 (**2017**) doi:10.1021/acs.analchem.7b00631
- R. Middendorp, M. Dürr, I. Niemeyer, and D. Bosbach. Micro Particle Suspensions for Preparation of Reference Materials for Particle Analysis Methods in Safeguards. *ESARDA Bulletin*, 54:23-30 (**2017**)
- S. Neumeier, R. Middendorp, A. Knott, M. Dürr, M. Klinkenberg, F. Pointurier, D. Ferreira Sanchez, V. Samson, D. Grolimund, I. Niemeyer and D. Bosbach. Microparticle production as reference materials for particle analysis methods in safeguards. *MRS Advances*, 1-8 (**2018**) doi:10.1557/adv.2018.166
- R. Middendorp, M. Dürr, M. Klinkenberg and D. Bosbach. Uranium Microparticle Suspensions for the Production of Reference Materials for Micro-Analytical Methods. *Journal of Radioanalytical and Nuclear Chemistry* (**in preparation**)

Conferences Proceedings

- M. Dürr, A. Knott, R. Middendorp, I. Niemeyer, S. Küppers, M. Zoriy, M. Froning, and D. Bosbach. Activities at Forschungszentrum Jülich in Safeguards Analytical Techniques and Measurements. *Symposium on International Safeguards: Linking Strategy, Implementation and People* (**2014**)
- C. Schreinemachers, R. Middendorp, A. Bukaeomskiy, G. Modolo, M. Brykala, M. Rogowski, A. Deptula, V. Cuba, T. Pavelkova, F. Sebesta, and J. John. Conversion of actinides into oxide pre-cursors for innovative fuel fabrication. *TopFuel 2015 Conference Proceedings, European Nuclear Society* (**2015**)
- R. Middendorp, A. Knott, and M. Dürr. Preparation of Uranium Micro-Particles as Reference Material for Nuclear Safeguards. *ESARDA* 37^{th} *Annual Meeting Proceedings*, 66:488–497 (**2015**)
- A. Knott, R. Middendorp, E. Chinea-Cano, L. Sangely, M. Dürr, S. Vogt, and D. Bosbach. Uranium Microparticle Production: Support of IAEA's Analytical Capabilities. *ESARDA* 39^{th} *annual meeting symposium proceedings* (**2017**)

Posters

- R. Middendorp, A. Knott, M. Dürr, I. Niemeyer, and D. Bosbach. Preparation of Microparticle Reference Materials for Nuclear Safeguards Particle Analysis. 8^{th} *European Summer School on Separation Chemistry and Conditioning as well as Supramolecular, Intermolecular, Interaggregate Interactions* (**2014**)
- R. Middendorp, A. Knott, and M. Dürr. Uniform Micro-Particles as Reference Material for Mass-Spectrometry. *Advanced Techniques in Actinide Spectroscopy* (**2014**)
- R. Middendorp, M. Dürr, and D. Bosbach. Production and Characterization of Uranium Oxide Microparticle Reference Materials for Nuclear Safeguards Applications. *GDCh Wissenschaftsforum* (**2015**)
- R. Middendorp, M. Dürr, and D. Bosbach. The Stability of Uranium Oxide Microspheres for Future Application as Reference Standard in Analytical Measurements. 5^{th} *International ATALANTE Conference on Nuclear Chemistry for Sustainable Fuel Cycles* (**2016**)

Bibliography

[1] International Atomic Energy Agency. Treaty on the non-proliferation of nuclear weapons, 22 April 1970.

[2] United Nations Office for Disarmament Affairs. Disarmament Treaties Database: Treaty on the Non-Proliferation of Nuclear Weapons (NPT). `http://disarmament.un.org/treaties/t/npt`. Accessed: August 20, 2017.

[3] M. Sturm. Destructive analysis: Effective analytical support to nuclear safeguards and non-proliferation. *ESARDA Bulletin*, 45:56–65, 2010.

[4] S. Boulyga, S. Konegger-Kappel, S. Richter, and L. Sangely. Mass spectrometric analysis for nuclear safeguards. *Journal of Analytical Atomic Spectrometry*, 30:1469–1489, 2015. doi:10.1039/C4JA00491D.

[5] International Atomic Energy Agency. Model Protocol Additional to the Agreement(s) between State(s) and the Inernational Atomic Energy Agency for the Application of Safeguards, September 1997.

[6] D. Donohue. Strengthening IAEA safeguards through environmental sampling and analysis. *Journal of Alloys and Compounds*, 271–273:11–18, 1998. doi:10.1016/S0925-8388(98)00015-2.

[7] D. L. Donohue. Peer reviewed: Strengthened nuclear safeguards. *Analytical Chemistry*, 74(1):28 A–35 A, 2002. doi:10.1021/ac021909y.

[8] C. Lee, K. Iguchi, J. Inagawa, D. Suzuki, F. Esaka, M. Magara, S. Sakurai, K. Watanabe, and S. Usuda. Development in fission track-thermal ionization mass spectrometry for particle analysis of safeguards environmental samples. *Journal of Radioanalytical and Nuclear Chemistry*, 272(2):299–302, 2007. doi:10.1007/s10967-007-0519-0.

[9] F. Esaka, D. Suzuki, and M. Magara. Identifying Uranium Particles Using Fission Tracks and Microsampling Individual Particles for Analysis Using Thermal Ionization Mass Spectrometry. *Analytical Chemistry*, 87(5):3107–3113, 2015. doi:10.1021/acs.analchem.5b00236.

[10] M. Kraiem, S. Richter, H. Kuehn, E. A. Stefaniak, G. Kerckhove, J. Truyens, and Y. Aregbe. Investigation of Uranium Isotopic Signatures in Real-Life Particles from a

Nuclear Facility by Thermal Ionization Mass Spectrometry. *Analytical Chemistry*, 83(8): 3011–3016, 2011. doi:10.1021/ac103153k.

[11] Implementation of the NPT Safeguards Agreement in the Islamic Republic of Iran. GOV/2006/38, International Atomic Energy Agency, 8 June 2006.

[12] Implementation of the NPT Safeguards Agreement in the Islamic Republic of Iran. GOV/2006/53, International Atomic Energy Agency, 31 August 2006.

[13] International Atomic Energy Agency. Communication dated 24 July 2015 received from China, France, Germany, the Russian Federation, the United Kingdom, the United States of America (the E3/EU+3) and the islamic Republic of Iran concerning the text of the Joint Comprehensive Plan of Action (JCPOA), 14 July 2015.

[14] Implementation of the NPT Safeguards Agreement and relevant provisions of Security Council resolutions in the Islamic Republic of Iran. GOV/2015/65, International Atomic Energy Agency, 18 November 2015.

[15] DIN EN ISO/IEC 17025:2005 General requirements for the competence of testing and calibration laboratories, 2005.

[16] ISO 17043:2010 Conformity assessment - general requirements for proficiency testing, 2010.

[17] BIPM, IEC, IFCC, ILAC, ISO, IUPAC, IUPAP, and OIML. *International vocabulary of metrology – Basic and general concepts and associated terms*, volume 3. 2012.

[18] ISO 17034:2016 General requirements for the competence of reference material producers, 2016.

[19] ISO Guide 35:2006 Reference materials - General and statistical principles for certification, 2006.

[20] BIPM, IEC, IFCC, ISO, IUPAC, and IUPAP. *Guide to the expression of uncertainty in measurement*, volume 3. 2008.

[21] R. Kips, A. Leenaers, G. Tamborini, M. Betti, S. Van den Berghe, R. Wellum, and P. Taylor. Characterization of Uranium Particles Produced by Hydrolysis of UF_6 Using SEM and SIMS. *Microscopy and Microanalysis*, 13:156–164, 2007. doi:10.1017/S1431927607070341.

[22] R. Kips, M. Kristo, J. Crowhurst, and I. Hutcheon. Characterization of Uranium Oxyfluoride Particles for Nuclear Safeguards. LLNL-PROC-488375, Lawrence Livermore National Laboratory, 16 June 2011.

[23] Y. Aregbe, J. Truyens, R. Kips, S. Richter, E. Stefaniak, H. Kühn, and M. Kraiem. *NUSIMEP-6: Uranium isotope amount ratios in uranium particles*. EUR 23702 EN-2008. Publications Office of the European Union, 2008.

[24] J. Truyens, E. Stefaniak, S. Mialle, and Y. Aregbe. *NUSIMEP-7: Uranium isotope amount ratios in uranium particles*. EUR 25179 EN-2011. Publications Office of the European Union, 2011.

[25] Y. Aregbe, T. Prohaska, Z. Stefanka, E. Szeles, A. Hubert, and S. Boulyga. Report on the Workshop on Direct Analysis of Solid Samples Using Laser Ablation-Inductively Coupled Plasma-Mass Spctrometry (LA-ICP-MS). *ESARDA Bulletin*, 46:136–145, 2011.

[26] K. G. W. Inn, C. M. Johnson, W. Oldham, S. Jerome, L. Tandon, T. Schaaff, R. Jones, D. Mackney, P. MacKill, B. Palmer, D. Smith, S. LaMont, and J. Griggs. The urgent requirement for new radioanalytical certified reference materials for nuclear safeguards, forensics, and consequence management. *Journal of Radioanalytical and Nuclear Chemistry*, 296(1):5–22, 2013. doi:10.1007/s10967-012-1972-y.

[27] K. G. W. Inn, S. LaMont, S. Jerome, R. Essex, C. M. Johnson, J. Morrison, C. Frechou, T. Branger, and H. Dion. Roadmap for radioanalytical reference and performance evaluation materials for current and emerging issues. *Journal of Radioanalytical and Nuclear Chemistry*, 307(3):2529–2538, 2016. doi:10.1007/s10967-016-4694-8.

[28] C. R. Hammond. CRC Handbook of Chemistry and Physics. In W. M. Haynes, editor, *The Elements*, chapter 4, page 42. CRC Press/Taylor and Francis, 95 edition, 2014.

[29] W. M. Haynes. CRC Handbook of Chemistry and Physics. In W. M. Haynes, editor, *Atomic Masses and Abundances*, chapter 1, pages 13–16. CRC Press/Taylor and Francis, 95 edition, 2014.

[30] P. D. Wilson, editor. *The Nuclear Fuel Cycle*. Oxford Science Publications, 1996.

[31] International Atomic Energy Agency. Glossary U-V. `https://www.iaea.org/ns/tutorials/regcontrol/intro/glossaryu_v.htm`, June 2017. Accessed: August 20, 2017.

[32] H. G. Wood. Effects of Separation Processes on Minor Uranium Isotopes in Enrichment Cascades. *Science & Global Security*, 16(1-2):26–36, 2008. doi:10.1080/08929880802361796.

[33] I. Grenthe, I. Buck, E. Drozdynski, J. Fujino, T. Albrecht-Schmitt, and S. Wolf, editors. *Uranium*, chapter 5, pages 253–698. The Chemistry of the Actinide and Transactinide Elements. Springer, 3 edition, 2006.

[34] H. R. Hoekstra and S. Siegel. The uranium-oxygen system: U_3O_8-UO_3. *Journal of Inorganic and Nuclear Chemistry*, 18(0):154–165, 1961. doi:10.1016/0022-1902(61)80383-7.

[35] V. J. Wheeler, R. M. Dell, and E. Wait. Uranium trioxide and the UO_3 hydrates. *Journal of Inorganic and Nuclear Chemistry*, 26:1829–1845, 1964. doi:10.1016/0022-1902(64)80007-5.

[36] L. Sweet, T. Blake, J. Henager, CharlesH., S. Hu, T. Johnson, D. Meier, S. Peper, and J. Schwantes. Investigation of the polymorphs and hydrolysis of uranium trioxide. *Journal of Radioanalytical and Nuclear Chemistry*, 296(1):105–110, 2013. doi:10.1007/s10967-012-2063-9.

[37] K. O. Kvashnina, S. M. Butorin, P. Martin, and P. Glatzel. Chemical State of Complex Uranium Oxides. *Physical Review Letters*, 111:253002, 2013. doi:10.1103/PhysRevLett.111.253002.

[38] K. Sanyal, A. Khooha, G. Das, M. K. Tiwari, and N. L. Misra. Direct Determination of Oxidation States of Uranium in Mixed-Valent Uranium Oxides Using Total Reflection X-ray Fluorescence X-ray Absorption Near-Edge Spectroscopy. *Analytical Chemistry*, 89 (1):871–876, 2017. doi:10.1021/acs.analchem.6b03945.

[39] B. Loopstra. On the crystal structure of α-U_3O_8. *Journal of Inorganic and Nuclear Chemistry*, 39(9):1713 – 1714, 1977. doi:10.1016/0022-1902(77)80137-1.

[40] G. Rousseau, L. Desgranges, F. Charlot, N. Millot, J. Nièpce, M. Pijolat, F. Valdivieso, G. Baldinozzi, and J. Bérar. A detailed study of UO_2 to U_3O_8 oxidation phases and the associated rate-limiting steps. *Journal of Nuclear Materials*, 355(1–3):10–20, 2006. doi:10.1016/j.jnucmat.2006.03.015.

[41] O. Roth and M. Jonsson. Oxidation of UO_2(s) in aqueous solution. *Central European Journal of Chemistry*, 6(1):1–14, 2008. doi:10.2478/s11532-007-0067-z.

[42] M. Amme. Contrary effects of the water radiolysis product H_2O_2 upon the dissolution of nuclear fuel in natural ground water and deionized water. *Radiochimica Acta*, 90(7): 399–406, 2002. doi:10.1524/ract.2002.90.7_2002.399.

[43] B. Hanson, B. McNamara, E. Buck, J. Friese, E. Jenson, K. Krupka, and B. Arey. Corrosion of commercial spent nuclear fuel. 1. Formation of studtite and metastudtite. *Radiochimica Acta*, 93(3):159–168, 2005. doi:10.1524/ract.93.3.159.61613.

[44] R. Vochten, E. De Gravel, and H. Lauwers. Transformation of synthetic U_3O_8 into different uranium oxide hydrates. *Mineralogy and Petrology*, 41(2):247–255, 1990. doi:10.1007/BF01168498.

[45] A. L. Tamasi, K. S. Boland, K. Czerwinski, J. K. Ellis, S. A. Kozimor, R. L. Martin, A. L. Pugmire, D. Reilly, B. L. Scott, A. D. Sutton, G. L. Wagner, J. R. Walensky, and M. P. Wilkerson. Oxidation and Hydration of U_3O_8 Materials Following Controlled Exposure to Temperature and Humidity. *Analytical Chemistry*, 87(8):4210–4217, 2015. doi:10.1021/ac504105t.

[46] W. L. Marshall, J. S. Gill, and C. H. Secoy. The Uranyl Nitrate-Water System Above 60 °C. *Journal of the American Chemical Society*, 73(4):1867–1869, 1951. doi:10.1021/ja01148a532.

[47] J. K. Dawson, E. Wait, K. Alcock, and D. R. Chilton. Some aspects of the system uranium trioxide-water. *Journal of the Chemical Society*, pages 3531–3540, 1956. doi:10.1039/JR9560003531.

[48] D. Vaughan, C. Schwartz, C. Melton, and J. Bridge. Thermal decomposition of uranyl nitrate hexahydrate. BMI-1110, Battelle Memorial Institute, Columbus, OH, 1956.

[49] W. Lodding and L. Ojamaa. Dehydration and thermal decomposition of uranyl nitrates in the presence of steam. *Journal of Inorganic and Nuclear Chemistry*, 27(6):1261–1268, 1965. doi:10.1016/0022-1902(65)80088-4.

[50] W. H. Smith. Thermal dehydration of uranyl nitrate hydrates. *Journal of Inorganic and Nuclear Chemistry*, 30(7):1761–1768, 1968. doi:10.1016/0022-1902(68)80351-3.

[51] R. Kozlova, V. Matyukha, and N. Dedov. Mechanism and Kinetics of Thermal Decomposition of Uranyl Nitrate Hexahydrate under the Nonisothermal Conditions. *Radiochemistry*, 49(2):130–134, 2007. doi:10.1134/S1066362207020063.

[52] K. Iwamoto. Thermal decomposition of uranyl nitrate hexahydrate in the presence of graphite. *Journal of Nuclear Science and Technology*, 1(4):113–119, 1964. doi:10.1080/18811248.1964.9732092.

[53] S. Dash, M. Kamruddin, S. Bera, P. Ajikumar, A. Tyagi, S. Narasimhan, and B. Raj. Temperature programmed decomposition of uranyl nitrate hexahydrate. *Journal of Nuclear Materials*, 264(3):271–282, 1999. doi:10.1016/S0022-3115(98)00495-4.

[54] R. S. Ondrejcin. Thermal Denitration of Uranyl Nitrate Hexahydrate. *Journal of Chemical & Engineering Data*, 11(1):130–133, 1966. doi:10.1021/je60028a040.

[55] P. Clough, D. Dollimore, and P. Grundy. The thermal decomposition of uranyl acetate. *Journal of Inorganic and Nuclear Chemistry*, 31(2):361–370, 1969. doi:10.1016/0022-1902(69)80479-3.

[56] I. Yanachkova and M. Staevsky. Thermal decomposition of uranyl acetate. *Journal of Materials Science*, 8(4):606–610, 1973. doi:10.1007/BF00550467.

[57] D. Dollimore and P. Clough. A study of the thermal decomposition of uranyl acetate using infra-red spectroscopic techniques. *Thermochimica Acta*, 85(0):43–46, 1985. doi:10.1016/0040-6031(85)85525-8.

[58] G. Çılgı, H. Cetişli, and R. Donat. Thermal and kinetic analysis of uranium salts. *Journal of Thermal Analysis and Calorimetry*, 110(1):127–135, 2012. doi:10.1007/s10973-011-2145-x.

[59] A. V. Dubrovin, K. M. Dunayeva, V. I. Spitzyn, V. V. Alexandrov, V. V. Boldyrev, and V. G. Morozov. On the thermal decomposition mechanism of uranyl and uranium(IV) acetates. *Thermochimica Acta*, 27(1–3):299–306, 1978. doi:10.1016/0040-6031(78)85045-X.

[60] T. Sato, S. Shiota, S. Ikoma, and F. Ozawa. Thermal decomposition of uranyl chloride hydrate. *Journal of Applied Chemistry and Biotechnology*, 27(1):275–280, 1977. doi:10.1002/jctb.5020270141.

[61] N. Reuge, B. Caussat, N. Joffin, J. Dexpert-ghys, M. Verelst, and H. Dexpert. Modeling of spray pyrolysis - why are the synthesized Y_2O_3 microparticles hollow? *AIChE Journal*, 54(2):394–405, 2008. doi:10.1002/aic.11375.

[62] S. Jain, D. J. Skamser, and T. T. Kodas. Morphology of single-component particles produced by spray pyrolysis. *Aerosol Science and Technology*, 27(5):575–590, 1997. doi:10.1080/02786829708965498.

[63] G. L. Messing, S.-C. Zhang, and G. V. Jayanthi. Ceramic powder synthesis by spray pyrolysis. *Journal of the American Ceramic Society*, 76(11):2707–2726, 1993. doi:10.1111/j.1151-2916.1993.tb04007.x.

[64] J. Tushingham. The preparation of a low-enriched uranium particle standard for environmental analysis. SRDP-R259, AEA Technology, 1998.

[65] W. H. Walton and W. C. Prewett. The production of sprays and mists of uniform drop size by means of spinning disc type sprayers. *Proceedings of the Physical Society. Section B*, 62(6):341, 1949. doi:10.1088/0370-1301/62/6/301.

[66] J. B. Harstad, M. E. Filler, W. T. Hushen, and H. M. Decker. Homogeneous bacterial aerosols produced with a spinning-disc generator. *Applied Microbiology*, 20(1):94–97, 1970.

[67] F. Claverie, A. Hubert, S. Berail, A. Donard, F. Pointurier, and C. Pécheyran. Improving Precision and Accuracy of Isotope Ratios from Short Transient Laser Ablation-Multicollector-Inductively Coupled Plasma Mass Spectrometry Signals: Application to

Micrometer-Size Uranium Particles. *Analytical Chemistry*, 88(8):4375–4382, 2016. doi:10.1021/acs.analchem.5b04802.

[68] T. Shinonaga, D. Donohue, H. Aigner, S. Bürger, D. Klose, T. Kärkelä, R. Zilliacus, A. Auvinen, O. Marie, and F. Pointurier. Production and Characterization of Plutonium Dioxide Particles as a Quality Control Material for Safeguards Purposes. *Analytical Chemistry*, 84(6):2638–2646, 2012. doi:10.1021/ac202502z.

[69] Atomizer Aerosol Generator Model 3079A. 1930031 rev. D, TSI Incorporated, 2015.

[70] Seed particle Generation by the Model 9302 Atomizer. 9302-001-A4, TSI Incorporated, 2015.

[71] G. R. Waterbury, R. M. Douglass, and C. F. Metz. Thermogravimetric behavior of plutonium metal, nitrate, sulfate, and oxalate. *Analytical Chemistry*, 33(8):1018–1023, 1961. doi:10.1021/ac60176a047.

[72] W. M. Haynes. CRC Handbook of Chemistry and Physics. In W. M. Haynes, editor, *Physical Constants of Inorganic Compounds*, chapter 4, pages 43–101. CRC Press/Taylor and Francis, 94 edition, 2013.

[73] Y. Ranebo, N. Niagolova, N. Erdmann, M. Eriksson, G. Tamborini, and M. Betti. Production and Characterization of Monodisperse Plutonium, Uranium, and Mixed Uranium-Plutonium Particles for Nuclear Safeguard Applications. *Analytical Chemistry*, 82(10): 4055–4062, 2010. doi:10.1021/ac9029295.

[74] N. Erdmann, M. Betti, O. Stetzer, G. Tamborini, J. Kratz, N. Trautmann, and J. van Geel. Production of monodisperse uranium oxide particles and their characterization by scanning electron microscopy and secondary ion mass spectrometry. *Spectrochimica Acta Part B*, 55(10):1565–1575, 2000. doi:10.1016/S0584-8547(00)00262-7.

[75] B. O. Stetzer. *Spaltspuranalyse von Uranoxidpartikeln*. PhD thesis, Universität Mainz, 2001.

[76] Y. Ranebo, P. M. L. Hedberg, M. J. Whitehouse, K. Ingeneri, and S. Littmann. Improved isotopic SIMS measurements of uranium particles for nuclear safeguard purposes. *Journal of Analytical Atomic Spectrometry*, 24:277–287, 2009. doi:10.1039/B810474C.

[77] M. Kraiem, S. Richter, N. Erdmann, H. Kuehn, M. Hedberg, and Y. Aregbe. Characterizing uranium oxide reference particles for isotopic abundances and uranium mass by single particle isotope dilution mass spectrometry. *Analytica Chimica Acta*, 748(0): 37–44, 2012. doi:10.1016/j.aca.2012.08.030.

[78] Y. Ranebo. *Physical Characterization of Actinide Particles*. PhD thesis, Lund University, 2009.

[79] K. Raptis, C. Ingelbrecht, R. Wellum, A. Alonso, W. D. Bolle, and R. Perrin. The preparation of uranium-doped glass reference materials for environmental measurements. *Nuclear Instruments and Methods in Physics Research Section A: Accelerators, Spectrometers, Detectors and Associated Equipment*, 480(1):40–43, 2002. doi:10.1016/S0168-9002(01)02045-9.

[80] S. Kappel, S. F. Boulyga, and T. Prohaska. Direct uranium isotope ratio analysis of single micrometer-sized glass particles. *Journal of Environmental Radioactivity*, 113: 8–15, 2012. doi:10.1016/j.jenvrad.2012.03.017.

[81] J. J. Stoffels, W. C. Cannon, and D. M. Robertson. A particulate isotopic standard of plutonium in an aluminosilicate matrix. *Journal of the American Society for Mass Spectrometry*, 2(1):81–84, 1991. doi:10.1016/1044-0305(91)80064-E.

[82] J. Stoffel, J. Briant, and D. Simons. A particulate isotopic standard of uranium and plutonium in an aluminosilicate matrix. *Journal of the American Society for Mass Spectrometry*, 5(9):852–858, 1994. doi:10.1016/1044-0305(94)87008-X.

[83] Y. Park, M. Lee, H. Pyo, H. Kim, S. Sohn, K. Jee, and W. Kim. The preparation of uranium-adsorbed silica particles as a reference material for the fission track analysis. *Nuclear Instruments and Methods in Physics Research Section A: Accelerators, Spectrometers, Detectors and Associated Equipment*, 545(1–2):493 – 502, 2005. doi:10.1016/j.nima.2005.01.312.

[84] E. A. Stefaniak, L. Darchuk, D. Sapundjiev, R. Kips, Y. Aregbe, and R. V. Grieken. New insight into UO_2F_2 particulate structure by micro-Raman spectroscopy. *Journal of Molecular Structure*, 1040(0):206–212, 2013. doi:10.1016/j.molstruc.2013.02.012.

[85] E. A. Stefaniak, F. Pointurier, O. Marie, J. Truyens, and Y. Aregbe. In-SEM Raman microspectroscopy coupled with EDX - a case study of uranium reference particles. *Analyst*, 139:668–675, 2014. doi:10.1039/C3AN01872E.

[86] R. Kips, A. Pidduck, M. Houlton, A. Leenaers, J. Mace, O. Marie, F. Pointurier, E. Stefaniak, P. Taylor, S. V. den Berghe, P. V. Espen, R. V. Grieken, and R. Wellum. Determination of fluorine in uranium oxyfluoride particles as an indicator of particle age. *Spectrochimica Acta Part B*, 64(3):199–207, 2009. doi:10.1016/j.sab.2008.12.001.

[87] C.-G. Lee, D. Suzuki, F. Esaka, M. Magara, and K. Song. Ultra-trace analysis of plutonium by thermal ionization mass spectrometry with a continuous heating technique without chemical separation. *Talanta*, 141:92–96, 2015. doi:https://doi.org/10.1016/j.talanta.2015.03.060.

[88] W. Bronger. Röntgenographische Untersuchungen nach der Pulvermethode - Eine Einführung, 1999.

[89] W. Borchardt-Ott. *Kristallographie*. Springer DE, 2009.

[90] M. Newville. *Fundamentals of XAFS*. University of Chicago, 2004.

[91] M. A. Denecke. Actinide speciation using X-ray absorption fine structure spectroscopy. *Coordination Chemistry Reviews*, 250(7–8):730–754, 2006. doi:10.1016/j.ccr.2005.09.004.

[92] L. Rayleigh. On the Capillary Phenomena of Jets. *Proceedings of the Royal Society of London*, 29(196-199):71–97, 1879. doi:10.1098/rspl.1879.0015.

[93] D. B. Harmon. Drop sizes from low speed jets. *Journal of the Franklin Institute*, 259 (6):519–522, 1955. doi:10.1016/0016-0032(55)90098-3.

[94] N. R. Lindblad and J. M. Schneider. Production of uniform-sized liquid droplets. *Journal of Scientific Instruments*, 42(8):635, 1965. doi:10.1088/0950-7671/42/8/338.

[95] J. M. Schneider and C. D. Hendricks. Source of uniform sized liquid droplets. *Review of Scientific Instruments*, 35(10):1349–1350, 1964. doi:10.1063/1.1718742.

[96] F. Esaka, K. Watanabe, H. Fukuyama, T. Onodera, K. T. Esaka, M. Magara, S. Sakurai, and S. Usuda. Efficient Isotope Ratio Analysis of Uranium Particles in Swipe Samples by Total-Reflection X-ray Fluorescence Spectrometry and Secondary Ion Mass Spectrometry. *Journal of Nuclear Science and Technology*, 41(11):1027–1032, 2004. doi:10.1080/18811248.2004.9726327.

[97] Vibrating Orifice Aerosol Generator Model 3450. 1930086 rev. B, TSI Incorporated, 2012.

[98] S. Nakashima. Kinetics and thermodynamics of U reduction by natural and simple organic matter. *Organic Geochemistry*, 19(4):421–430, 1992. doi:10.1016/0146-6380(92)90009-M.

[99] J. Schindelin, I. Arganda-Carreras, E. Frise, V. Kaynig, M. Longair, T. Pietzsch, S. Preibisch, C. Rueden, S. Saalfeld, B. Schmid, et al. Fiji: an open-source platform for biological-image analysis. *Nature methods*, 9(7):676–682, 2012. doi:10.1038/nmeth.2019.

[100] J. Schindelin, C. T. Rueden, M. C. Hiner, and K. W. Eliceiri. The ImageJ ecosystem: an open platform for biomedical image analysis. *Molecular reproduction and development*, 82(7-8):518–529, 2015. doi:10.1002/mrd.22489.

[101] A. Jillavenkatesa, S. J. Dapkunas, and H. L. Lin-sien. NIST recommended practice guide special publication 960-1 Particle size characterization. 2001.

[102] V. A. Hackley and C. F. Ferraris. NIST Recommended Practice Guide 960-3 Use of Nomenclature in Dispersion Science and Technology. 2001.

[103] International Centre for Diffraction Data. PDF-2 (148 379 entries). Database, 2002.

[104] A. Knott and M. Dürr. Production of monodisperse uranium particles for nuclear safeguards applications. *ESARDA Bulletin*, 49:40–45, 2013.

[105] N. Reuge, J. Dexpert-Ghys, M. Verelst, and B. Caussat. Y_2O_3:Eu micronic particles synthesised by spray pyrolysis: Global modelling and optimisation of the evaporation stage. *Chemical Engineering and Processing: Process Intensification*, 47(4):731–743, 2008. doi:10.1016/j.cep.2006.12.007.

[106] C. Chen, T. Tseng, S. Tsai, C. Lin, and H. Lin. Effect of precursor characteristics on zirconia and ceria particle morphology in spray pyrolysis. *Ceramics International*, 34(2): 409–416, 2008. doi:10.1016/j.ceramint.2006.10.013.

[107] K. Zhong, G. Peabody, H. Glicksman, and S. Ehrman. Particle generation by cosolvent spray pyrolysis: Effects of ethanol and ethylene glycol. *Journal of Materials Research*, 27(19):2540–2550, 2012. doi:10.1557/jmr.2012.248.

[108] R. Middendorp, M. Dürr, A. Knott, F. Pointurier, D. Ferreira Sanchez, V. Samson, and D. Grolimund. Characterization of the Aerosol-Based Synthesis of Uranium Particles as a Potential Reference Material for Microanalytical Methods. *Analytical Chemistry*, 89 (8):4721–4728, 2017. doi:10.1021/acs.analchem.7b00631.

[109] A. Knott. *Production and Characterization of Monodisperse Uranium Particles for Nuclear Safeguards Applications*. PhD thesis, Forschungszentrum Jülich GmbH, 2016.

[110] P. Haas. *Use of UO_3 to load Cation Exchange Resin for Microsphere Preparation*. HTGR fuel development. ORNL, Oak Ridge, 1972.

[111] P. Haas. *Loading of Uranium on Caboxylic Acid Cation-Exchange Resins using Solvent Extraction of Nitrate*. HTGR fuel development. ORNL, Oak Ridge, 1975.

[112] C. Schreinemachers. Preparation and characterization of U / Nd microspheres synthesized by internal gelation. Master's thesis, FH Aachen University of Applied Sciences, campus Jülich, 2013.

[113] R. Middendorp. Preparation and characterization of U/Nd oxide microspheres synthesized by the weak-acid resin process. Master's thesis, FH Aachen University of Applied Sciences, campus Jülich, October 2013.

[114] R. Middendorp, M. Dürr, and D. Bosbach. The stability of uranium microspheres for future application as reference standard in analytical measurements. *Procedia Chemistry*, 21:285–292, 2016. doi:10.1016/j.proche.2016.10.040.

[115] F. Huber, D. Schild, T. Vitova, J. Rothe, R. Kirsch, and T. Schäfer. U(VI) removal kinetics in presence of synthetic magnetite nanoparticles. *Geochimica et Cosmochimica Acta*, 96:154–173, 2012. doi:10.1016/j.gca.2012.07.019.

[116] I. Pidchenko, K. O. Kvashnina, T. Yokosawa, N. Finck, S. Bahl, D. Schild, R. Polly, E. Bohnert, A. Rossberg, J. Göttlicher, K. Dardenne, J. Rothe, T. Schäfer, H. Geckeis, and T. Vitova. Uranium Redox Transformations after U(VI) Coprecipitation with Magnetite Nanoparticles. *Environmental Science & Technology*, 51(4):2217–2225, 2017. doi:10.1021/acs.est.6b04035.

[117] K. Uchinokura, T. Sekine, and E. Matsuura. Raman scattering by silicon. *Solid State Communications*, 11(1):47–49, 1972. doi:10.1016/0038-1098(72)91127-1.

[118] G. C. Allen, I. S. Butler, and N. A. Tuan. Characterisation of uranium oxides by micro-Raman spectroscopy. *Journal of Nuclear Materials*, 144(1):17–19, 1987. doi:10.1016/0022-3115(87)90274-1.

[119] I. S. Butler, G. C. Allen, and N. A. Tuan. Micro-Raman Spectrum of Triuranium Octoxide, U_3O_8. *Applied Spectroscopy*, 42(5):901–902, 1988. doi:10.1366/0003702884428888.

[120] M. L. Palacios and S. H. Taylor. Characterization of Uranium Oxides Using in Situ Micro-Raman Spectroscopy. *Applied Spectroscopy*, 54(9):1372–1378, 2000. doi:10.1366/0003702001951057.

[121] E. A. Stefaniak, A. Alsecz, I. E. Sajó, A. Worobiec, Z. Máthé, S. Török, and R. V. Grieken. Recognition of uranium oxides in soil particulate matter by means of μ-Raman spectrometry. *Journal of Nuclear Materials*, 381(3):278–283, 2008. doi:10.1016/j.jnucmat.2008.08.036.

[122] F. Pointurier and O. Marie. Identification of the chemical forms of uranium compounds in micrometer-size particles by means of micro-Raman spectrometry and scanning electron microscope. *Spectrochimica Acta Part B*, 65(9–10):797–804, 2010. doi:10.1016/j.sab.2010.06.008.

[123] M. Lipp, Z. Jenei, J. P. Klepeis, and W. Evans. Raman Investigation of The Uranium Compounds U_3O_8, UF_4, UH_3 and UO_3 under Pressure at Room Temperature. , Lawrence Livermore National Laboratory (LLNL), Livermore, CA, 2011.

[124] M. B. Shundalaua, P. Zajogina, I. Komiaka, . Sokolskya, and D. Umreikob. A DFT modeling of the uranium trioxide vibration spectra characteristics. *Journal of Spectroscopy and Dynamics*, 2:19, 2012.

[125] D. Ho, D. Manara, V. Z., A. Berlizov, T. Fanghänel, and K. Mayer. Applicability of Raman spectroscopy as a tool in nuclear forensics for analysis of uranium ore concentrates. *Radiochimica Acta*, 101(12):779–784, 2013. doi:10.1524/ract.2013.2110.

[126] F. Pointurier and O. Marie. Use of micro-Raman spectrometry coupled with scanning electron microscopy to determine the chemical form of uranium compounds in micrometer-size particles. *Journal of Raman Spectroscopy*, 44(12):1753–1759, 2013. doi:10.1002/jrs.4392.

[127] D. M. L. Ho, A. E. Jones, J. Y. Goulermas, P. Turner, Z. Varga, L. Fongaro, T. Fanghänel, and K. Mayer. Raman spectroscopy of uranium compounds and the use of multivariate analysis for visualization and classification. *Forensic Science International*, 251:61–68, 2015. doi:10.1016/j.forsciint.2015.03.002.

[128] D. H. M. Lin. *Study on the applicability of structural and morphological parameters of selected uranium compounds for nuclear forensic purposes*. PhD thesis, Ruperto-Carola University of Heidelberg, 2015.

[129] T. M. Alam, Z. Liao, M. Nyman, and J. Yates. Insight into Hydrogen Bonding of Uranyl Hydroxide Layers and Capsules by Use of ^{1}H Magic-Angle Spinning NMR Spectroscopy. *The Journal of Physical Chemistry C*, 120(19):10675–10685, 2016. doi:10.1021/acs.jpcc.6b02692.

[130] G. Giorgio, B. Mentzen, M. Breysse, and B. Claudel. Polymorphisme de l'acetate d'uranyle anhydre - II. *Journal of Inorganic and Nuclear Chemistry*, 32(5):1517–1524, 1970. doi:10.1016/0022-1902(70)80640-6.

[131] D. Manara and B. Renker. Raman spectra of stoichiometric and hyperstoichiometric uranium dioxide. *Journal of Nuclear Materials*, 321(2–3):233 – 237, 2003. doi:10.1016/S0022-3115(03)00248-4.

[132] V. G. Keramidas and W. B. White. Raman spectra of oxides with the fluorite structure. *The Journal of Chemical Physics*, 59(3):1561–1562, 1973. doi:10.1063/1.1680227.

[133] W. H. Weber, K. C. Hass, and J. R. McBride. Raman study of CeO_2: Second-order scattering, lattice dynamics, and particle-size effects. *Physical Review B*, 48:178–185, 1993. doi:10.1103/PhysRevB.48.178.

[134] D. Wheeler and I. Khan. A Raman spectroscopy study of cerium oxide in a cerium - 5 wt % lanthanum alloy. *Vibrational Spectroscopy*, 70:200–206, 2014. doi:10.1016/j.vibspec.2013.12.006.

[135] P. K. Narayanaswamy. Influence of temperature on the Raman spectra of crystals. *Proceedings of the Indian Academy of Sciences - Section A*, 26(6):511, 1947. doi:10.1007/BF03170909.

[136] G. Lucazeau. Effect of pressure and temperature on raman spectra of solids: anharmonicity. *Journal of Raman Spectroscopy*, 34(7-8):478–496, 2003. doi:10.1002/jrs.1027.

[137] I. Calizo, A. A. Balandin, W. Bao, F. Miao, and C. N. Lau. Temperature Dependence of the Raman Spectra of Graphene and Graphene Multilayers. *Nano Letters*, 7(9): 2645–2649, 2007. doi:10.1021/nl071033g.

[138] X. Huang, Y. Gao, T. Yang, W. Ren, H.-M. Cheng, and T. Lai. Quantitative Analysis of Temperature Dependence of Raman shift of monolayer WS_2. *Scientific Reports*, 6: 32236, 2016. doi:10.1038/srep32236.

[139] J. B. Nelson and D. P. Riley. An experimental investigation of extrapolation methods in the derivation of accurate unit-cell dimensions of crystals. *Proceedings of the Physical Society*, 57(3):160, 1945. doi:10.1088/0959-5309/57/3/302.

[140] L. Desgranges, G. Baldinozzi, G. Rousseau, J.-C. Nièpce, and G. Calvarin. Neutron Diffraction Study of the in-Situ Oxidation of UO_2. *Inorganic Chemistry*, 48(16):7585–7592, 2009. doi:10.1021/ic9000889.

[141] R. Chiba, H. Taguchi, T. Komatsu, H. Orui, K. Nozawa, and H. Arai. High temperature properties of $Ce_{1-x}Pr_xO_{2-\delta}$ as an active layer material for SOFC cathodes. *Solid State Ionics*, 197(1):42–48, 2011. doi:10.1016/j.ssi.2011.03.022.

[142] L. Vegard. Die konstitution der mischkristalle und die raumfüllung der atome. *Zeitschrift für Physik*, 5(1):17–26, 1921. doi:10.1007/BF01349680.

[143] G. Williamson and W. Hall. X-ray line broadening from filed aluminium and wolfram. *Acta Metallurgica*, 1(1):22–31, 1953.

[144] W. Ruedorff and G. Valet. Über das Ceruranblau und Mischkristalle im System CeO_2-UO_2-U_3O_8. *Zeitschrift für anorganische und allgemeine Chemie*, 271(5-6):257–272, 1953. doi:10.1002/zaac.19532710504.

[145] G. A. Mills. Oxygen exchange between water and inorganic oxy-anions. *Journal of the American Chemical Society*, 62(10):2833–2838, 1940. doi:10.1021/ja01867a058.

[146] D. R. Cole and S. Chakraborty. Rates and Mechanisms of Isotopic Exchange. *Reviews in Mineralogy and Geochemistry*, 43(1):83–223, 2001. doi:10.2138/gsrmg.43.1.83.

[147] R. M. Handler, B. L. Beard, C. M. Johnson, and M. M. Scherer. Atom Exchange between Aqueous Fe(II) and Goethite: An Fe Isotope Tracer Study. *Environmental Science & Technology*, 43(4):1102–1107, 2009. doi:10.1021/es802402m.

[148] S. Tsushima. "yl"-Oxygen Exchange in Uranyl(VI) Ion: A Mechanism Involving $(UO_2)^2(\mu{-}OH)_2^{2+}$ via U–Oyl–U Bridge Formation. *Inorganic Chemistry*, 51(3):1434–1439, 2012. doi:10.1021/ic201679e.

[149] G. S. Nolan and I. N. Bindeman. Experimental investigation of rates and mechanisms of isotope exchange (O, H) between volcanic ash and isotopically-labeled water. *Geochimica et Cosmochimica Acta*, 111:5–27, 2013. doi:10.1016/j.gca.2013.01.020.

[150] F. J. Johnston, D. A. Hutchison, and J. J. Katz. Oxygen exchange between uranium oxides and water. *Journal of Inorganic and Nuclear Chemistry*, 7(4):392–396, 1958. doi:10.1016/0022-1902(58)80248-1.

[151] R. Eykens, P. Maier-Komor, J. V. Gestel, and J. Pauwels. New aspects of thin polyimide foils. *Nuclear Instruments and Methods in Physics Research Section A: Accelerators, Spectrometers, Detectors and Associated Equipment*, 362(1):175–177, 1995. doi:10.1016/0168-9002(95)00238-3.

[152] G. Sibbens, K. Luyckx, A. Stolarz, M. Jaskóla, A. Korman, A. Moens, R. Eykens, D. Sapundjiev, and Y. Aregbe. Quality of polyimide foils for nuclear applications in relation to a new preparation procedure. *Nuclear Instruments and Methods in Physics Research Section A: Accelerators, Spectrometers, Detectors and Associated Equipment*, 655(1):47–52, 2011. doi:10.1016/j.nima.2011.06.018.

[153] C. Graf, D. L. J. Vossen, A. Imhof, and A. v. Blaaderen. A general method to coat colloidal particles with silica. *Langmuir*, 19(17):6693–6700, 2003. doi:10.1021/la0347859.

[154] S. Awad and R. Nagarajan. Chapter 6 - ultrasonic cleaning. In R. Kohli and K. L. Mittal, editors, *Developments in Surface Contamination and Cleaning*, pages 225–280. William Andrew Publishing, Oxford, 2010. ISBN 978-1-4377-7830-4.

[155] H. McKay. Kinetics of exchange reactions. *Nature*, 142:997–998, 1938. doi:10.1038/142997b0.

[156] R. B. Duffield and M. Calvin. The Stability of Chelate Compounds. III. Exchange Reactions of Copper Chelate Compounds. *Journal of the American Chemical Society*, 68(4):557–561, 1946. doi:10.1021/ja01208a007.

[157] T. H. Norris. The the kinetics of isotopic exchange reactions. *The Journal of Physical and Colloid Chemistry*, 54(6):777–783, 1950. doi:10.1021/j150480a005.

[158] S. R. Logan. The kinetics of isotopic exchange reactions. *Journal of Chemical Education*, 67(5):371, 1990. doi:10.1021/ed067p371.

[159] C. Schreinemachers, A. Bukaemskiy, M. Klinkenberg, S. Neumeier, G. Modolo, and D. Bosbach. Characterization of uranium neodymium oxide microspheres synthesized by internal gelation. *Progress in Nuclear Energy*, 72:17–21, 2014. doi:10.1016/j.pnucene.2013.07.016.

[160] R. Middendorp, M. Dürr, I. Niemeyer, and D. Bosbach. Micro Particle Suspensions for Preparation of Reference Materials for Particle Analysis Methods in Safeguards. *ESARDA Bulletin*, 54:23–30, 2017.

[161] L. Sangély, J. Poths, H. Siegmund, T. Tanpraphan, O. Bildstein, M. Aleshin, and A. Schwanhäusser. Implementation of Large-Geometry SIMS for Safeguards: 4 years later. In *ESARDA 37^{th} Annual Meeting Proceedings*, 66, pages 873–883. European Commission, May 2015.

[162] P. M. L. Hedberg, P. Peres, J. B. Cliff, F. Rabemananjara, S. Littmann, H. Thiele, C. Vincent, and N. Albert. Improved particle location and isotopic screening measurements of sub-micron sized particles by Secondary Ion Mass Spectrometry. *Journal of Analytical Atomic Spectrometry*, 26:406–413, 2011. doi:10.1039/C0JA00181C.

[163] *Model 3450 Vibrating orifice Aerosol Generator, Operation and Service Manual*. TSI Incorporated, m edition, April 2009.

[164] R. DerSimonian and N. Laird. Meta-analysis in clinical trials. *Controlled Clinical Trials*, 7(3):177–188, 1986. doi:10.1016/0197-2456(86)90046-2.

[165] M. Cox, P. Harris, and S. Ellison. Use of an excess-variance approach for the estimation of a key comparison reference value, associated standard uncertainty and degrees of equivalence for CCQM key comparison data. CCQM/11-18, National Physical Laboratory and LGC Ltd, 2011.

[166] BIPM. CCQM Guidance note: Estimation of a consensus KCRV and associated Degrees of Equivalence. , BIPM, 2013.

[167] F. Graybill and R. Deal. Combining unbiased estimators. *Biometrics*, 15(4):543–550, 1959. doi:10.2307/2527652.

[168] R. D. Deegan, O. Bakajin, T. F. Dupont, G. Huber, S. R. Nagel, and T. A. Witten. Contact line deposits in an evaporating drop. *Physical Review E*, 62(1):756, 2000. doi:10.1103/PhysRevE.62.756.

[169] J. N. Israelachvili. Chapter 13 - Van der Waals Forces between Particles and Surfaces. In J. N. Israelachvili, editor, *Intermolecular and Surface Forces*, pages 253 – 289. Academic Press, San Diego, third edition, 2011. ISBN 978-0-12-375182-9.

[170] D. E. Crean, C. L. Corkhill, T. Nicholls, R. Tappero, J. M. Collins, and N. C. Hyatt. Expanding the nuclear forensic toolkit: chemical profiling of uranium ore concentrate particles by synchrotron x-ray microanalysis. *RSC Advances*, 5:87908–87918, 2015. doi:10.1039/C5RA14963K.

[171] K. Mayer, M. Wallenius, and Z. Varga. Interviewing a Silent (Radioactive) Witness through Nuclear Forensic Analysis. *Analytical Chemistry*, 87(23):11605–11610, 2015. doi:10.1021/acs.analchem.5b01623.

[172] E. Keegan, M. J. Kristo, K. Toole, R. Kips, and E. Young. Nuclear Forensics: Scientific Analysis Supporting Law Enforcement and Nuclear Security Investigations. *Analytical Chemistry*, 88(3):1496–1505, 2016. doi:10.1021/acs.analchem.5b02915.

[173] Z. Varga, J. Krajko, M. Penkin, M. Novak, Z. Eke, M. Wallenius, and K. Mayer. Identification of uranium signatures relevant for nuclear safeguards and forensics. *Journal of Radioanalytical and Nuclear Chemistry*, pages 1–16, 2017. doi:10.1007/s10967-017-5247-5.

[174] J. R. Ehleringer, G. J. Bowen, L. A. Chesson, A. G. West, D. W. Podlesak, and T. E. Cerling. Hydrogen and oxygen isotope ratios in human hair are related to geography. *Proceedings of the National Academy of Science of the United States of America*, 105 (8):2788–2793, 2008. doi:10.1073/pnas.0712228105.

[175] L. Pajo, K. Mayer, and L. Koch. Investigation of the oxygen isotopic composition in oxidic uranium compounds as a new property in nuclear forensic science. *Fresenius' Journal of Analytical Chemistry*, 371(3):348–352, 2001. doi:10.1007/s002160100983.

[176] L. Pajo, G. Tamborini, G. Rasmussen, K. Mayer, and L. Koch. A novel isotope analysis of oxygen in uranium oxides: comparison of secondary ion mass spectrometry, glow discharge mass spectrometry and thermal ionization mass spectrometry. *Spectrochim. Acta, part B*, 56(5):541–549, 2001. doi:10.1016/S0584-8547(01)00219-1.

[177] G. Tamborini, D. Phinney, and M. Bildstein, O. andBetti. Oxygen Isotopic Measurements by Secondary Ion Mass Spectrometry in Uranium Oxide Microparticles: A Nuclear Forensics Diagnostic. *Analytical Chemistry*, 74(23):6098–6101, 2002. doi:10.1021/ac0259515.

[178] J. Plaue. *Forensic Signatures of Chemical Process History in Uranium Oxides*. PhD thesis, University of Nevada, January, 1 2013.

[179] J. Cliff, J. Denman, L. Martin, M. Kilburn, and T. Tanpraphan. Novel mass spectrometric techniques for the rapid characterization and fingerprinting of nuclear fuel materials. In *State of the Art Environmental Sample Analysis*, 2014.

[180] M. Dierick, E. Pili, N. Assayag, and P. Agrinier. Enhanced Oxygen Isotope Determination in Uranium Oxides using BrF_5 Fluorination. *Geostandards and Geoanalytical Research*, 2016. doi:10.1111/ggr.12160.

[181] Z. Szabó and I. Grenthe. Reactivity of the "y"-Bond in Uranyl(VI) Complexes. 1. Rates and Mechanisms for the Exchange between the trans-dioxo Oxygen Atoms in

$(UO_2)_2(OH)_2^{2+}$ and Mononuclear $UO_2(OH)n^{2-n}$ Complexes with Solvent Water. *Inorganic Chemistry*, 46(22):9372–9378, 2007. doi:10.1021/ic700817y.

[182] R. J. Baker. New Reactivity of the Uranyl(VI) Ion. *Chemistry – A European Journal*, 18(51):16258–16271, 2012. doi:10.1002/chem.201203085.

[183] M. Kaneko and S. R. Poulson. The rate of oxygen isotope exchange between nitrate and water. *Geochimica et Cosmochimica Acta*, 118:148–156, 2013. doi:10.1016/j.gca.2013.05.010.

[184] A. Donard, A.-C. Pottin, F. Pointurier, and C. Pecheyran. Determination of relative rare earth element distributions in very small quantities of uranium ore concentrates using femtosecond UV laser ablation - SF-ICP-MS coupling. *Journal of Analytical Atomic Spectrometry*, 30:2420–2428, 2015. doi:10.1039/C5JA00309A.

[185] M. Peńkin, S. Boulyga, and D. Fischer. Application of uranium impurity data for material characterization in nuclear safeguards. *Journal of Radioanalytical and Nuclear Chemistry*, pages 1–5, 2015. doi:10.1007/s10967-015-4380-2.

[186] A. Kersting, D. Efurd, D. Finnegan, D. Rokop, D. Smith, and J. Thompson. Migration of plutonium in ground water at the Nevada Test Site. *Nature*, 397:56–59, 1999. doi:10.1038/16231.

[187] A. P. Novikov, S. N. Kalmykov, S. Utsunomiya, R. C. Ewing, F. Horreard, A. Merkulov, S. B. Clark, V. V. Tkachev, and B. F. Myasoedov. Colloid Transport of Plutonium in the Far-Field of the Mayak Production Association, Russia. *Science*, 314(5799):638–641, 2006. doi:10.1126/science.1131307.

List of Figures

Figure 2.9: Adapted with permission from S. Jain, D. J. Skamser, and T. T. Kodas. Morphology of single-component particles produced by spray pyrolysis. *Aerosol Science and Technology*, 27(5):575–590, 1997. doi:10.1080/02786829708965498. Copyright © 1997 Taylor & Francis

Figure 2.10: Reprinted with permission from T. Shinonaga, D. Donohue, H. Aigner, S. Bürger, D. Klose, T. Kärkelä, R. Zilliacus, A. Auvinen, O. Marie, and F. Pointurier. Production and Characterization of Plutonium Dioxide Particles as a Quality Control Material for Safeguards Purposes. *Analytical Chemistry*, 84(6):2638–2646, 2012. doi:10.1021/ac202502z. Copyright © 2012 American Chemical Society.

Figure 2.11: Reprinted with permission from Y. Ranebo, N. Niagolova, N. Erdmann, M. Eriksson, G. Tamborini, and M. Betti. Production and Characterization of Monodisperse Plutonium, Uranium, and Mixed Uranium-Plutonium Particles for Nuclear Safeguard Applications. *Analytical Chemistry*, 82(10):4055–4062, 2010. doi:10.1021/ac9029295. Copyright © 2010 American Chemical Society.

Figure 2.12a: Reprinted with permission from Y. Ranebo, P. M. L. Hedberg, M. J. Whitehouse, K. Ingeneri, and S. Littmann. Improved isotopic SIMS measurements of uranium particles for nuclear safeguard purposes. *Journal of Analytical Atomic Spectrometry*, 24: 277–287, 2009. doi:10.1039/B810474C

Figure 2.12b/c: Reprinted from M. Kraiem, S. Richter, N. Erdmann, H. Kuehn, M. Hedberg, and Y. Aregbe. Characterizing uranium oxide reference particles for isotopic abundances and uranium mass by single particle isotope dilution mass spectrometry. *Analytica Chimica Acta*, 748(0):37–44, 2012. doi:10.1016/j.aca.2012.08.030 with permission from Elsevier.

Figure 2.13: Reprinted from K. Raptis, C. Ingelbrecht, R. Wellum, A. Alonso, W. D. Bolle, and R. Perrin. The preparation of uranium-doped glass reference materials for environmental measurements. *Nuclear Instruments and Methods in Physics Research Section A: Accelerators, Spectrometers, Detectors and Associated Equipment*, 480(1):40–43, 2002. doi:10.1016/S0168-9002(01)02045-9 with permission from Elsevier.

Figure 2.14: Reprinted from Y. Park, M. Lee, H. Pyo, H. Kim, S. Sohn, K. Jee, and W. Kim. The preparation of uranium-adsorbed silica particles as a reference material for the fission track analysis. *Nuclear Instruments and Methods in Physics Research Section A: Accelerators, Spectrometers, Detectors and Associated Equipment*, 545(1–2):493 – 502, 2005. doi:10.1016/j.nima.2005.01.312 with permission from Elsevier.

Figure 2.15: Reprinted with permission from R. Kips, A. Leenaers, G. Tamborini, M. Betti, S. Van den Berghe, R. Wellum, and P. Taylor. Characterization of Uranium Particles Produced by Hydrolysis of UF_6 Using SEM and SIMS. *Microscopy and Microanalysis*, 13:156–164, 2007. doi:10.1017/S1431927607070341. Copyright © 2007 Microscopy Society of America

Figure 4.19a, & 4.22: Reprinted/adapted with permission from R. Middendorp, M. Dürr, A. Knott, F. Pointurier, D. Ferreira Sanchez, V. Samson, and D. Grolimund. Characterization of the Aerosol-Based Synthesis of Uranium Particles as a Potential Reference Material for Microanalytical Methods. *Analytical Chemistry*, 89(8):4721–4728, 2017. doi:10.1021/acs.analchem.7b00631. Copyright © 2017 American Chemical Society.

Figure 4.19a, 4.27, & 4.28: Reprinted/adopted from R. Middendorp, M. Dürr, and D. Bosbach. The stability of uranium microspheres for future application as reference standard in analytical measurements. *Procedia Chemistry*, 21:285–292, 2016. doi:10.1016/j.proche.2016.10.040. Copyright © Elsevier B.V., used under the CC BY-NC-ND 4.0 Licence (`https://creativecommons.org/licenses/by-nc-nd/4.0/`)

Figure 5.1: Reprinted with permission from M. Kraiem, S. Richter, H. Kuehn, E. A. Stefaniak, G. Kerckhove, J. Truyens, and Y. Aregbe. Investigation of Uranium Isotopic Signatures in Real-Life Particles from a Nuclear Facility by Thermal Ionization Mass Spectrometry. *Analytical Chemistry*, 83(8):3011–3016, 2011. doi:10.1021/ac103153k. Copyright © 2011 American Chemical Society

List of Tables

Abbreviations

ADUN . . . . . acid deficient uranyl nitrate
APM . . . . . automated particle measurement
BET . . . . . Brunauer–Emmett–Teller
BSED . . . . . backscatter electron detector
CDF . . . . . cumulative distribution function
CEA . . . . . Commissariat à l'énergie atomique et aux énergies alternatives
CRM . . . . . certified reference material
DAM/DIF . . . . Direction des Applications Militaires/Île-de-France (CEA)
DLS . . . . . dynamic light scattering
DMF . . . . . dimetryl formamide
DU . . . . . depleted uranium
E-CDF . . . . . empirical cumulative distribution function
EDX . . . . . energy-dispersive X-ray spectroscopy
EXAFS . . . . . extended X-ray absorption fine structure
FIB . . . . . focussed ion beam
FT-TIMS . . . . fission track - thermal ionization mass spectrometry
FZJ . . . . . Forschungszentrum Jülich GmbH
GUM . . . . . Guide to the expression of uncertainty in measurement
HEPA . . . . . high efficiency particulate air
HEU . . . . . high-enriched uranium
HMTA . . . . . hexamethylenetetramine
IAEA . . . . . International Atomic Energy Agency
ICP-MS . . . . . inductively coupled plasma - mass spectrometry
IDMS . . . . . isotope dilution mass spectrometry
ID-TIMS . . . . . isotope dilution - thermal ionization mass spectroscopy
IEK-6 . . . . . Institute for Energy and Climate Research-6 (FZJ)
ISO . . . . . International Organization for Standardization
JCPOA . . . . . Joint Comprehensive Plan of Action
JRC . . . . . Joint Research Center
IRMM . . . . . Institute for Reference Materials and Methods
LA-ICP-MS . . . laser ablation - inductively coupled plasma - mass spectrometry

LEU . . . . . low enriched uranium
LG-SIMS . . . . . large geometry - secondary ion mass spectrometry
MFC . . . . . mass flow controller
MP . . . . . microprobe
NIST . . . . . National Institute of Standards and Technology
NPT . . . . . Treaty on the non-proliferation of nuclear weapons
NU . . . . . natural uranium
NUSIMEP . . . . Nuclear Signatures Interlaboratory Measurement Evaluation Programme
NWAL . . . . . Network of Analytical Laboratories
OPS . . . . . optical particle sizer
PSI . . . . . Paul-Scherrer Institute
PVP . . . . . polyvinylpyrrolidone
QC . . . . . quality control
Q-ICP-MS . . . . quadruple - inductively coupled plasma - mass spectrometry
RM . . . . . reference material
RU . . . . . reprocessed uranium
SAL . . . . . Seibersdorf Analytical Laboratory (IAEA)
SE . . . . . secondary electron
SEM . . . . . scanning electron microscope
SF-ICP-MS . . . sector field - inductively coupled plasma - mass spectrometry
SIMS . . . . . secondary ion mass spectrometry
SLS . . . . . Swiss Light Source (PSI)
TGA . . . . . thermogravimetric analysis
TIMS . . . . . thermal ionization mass spectrometry
ToF-SIMS . . . . time of flight - mass spectrometry
UA . . . . . uranyl acetate
UC . . . . . uranyl chloride
UN . . . . . uranyl nitrate
UOC . . . . . uranium ore concentrate
UV/VIS . . . . . ultraviolet/visible light spectroscopy
VIM . . . . . International Vocabulary of Metrology
VOAG . . . . . vibrating orifice aerosol generator
WDX . . . . . wavelength-dispersive X-ray spectroscopy
XANES . . . . . X-ray absorption near edge structure
XAS . . . . . X-ray absorption spectroscopy
XRD . . . . . X-ray diffraction
XRF . . . . . X-ray fluorescence
ZEA-3 . . . . . Central Institute of Engineering, Electronics and Analytics-3 (FZJ)

Appendices

Statistical Analysis

All uncertainties given in this work are expanded uncertainties ($U_c = k \cdot u_c$) which represent a confidence interval of 95.45 % ($k = 2$), assuming Gaussian distributions. Combined uncertainties (u_c) have been calculated by error propagation in accordance to the Guide to the expression of uncertainty in measurement [20] (GUM, ISO/IEC Guide 98-3:2008). Numerical results are reported with expanded uncertainties in parenthesis, where the number within the parentheses represents the uncertainty of the last two digits of the given result. Weighted means of multiple independent values with individual combined uncertainties are calculated using the DerSimonian-Laird method [164, 165].

Nitrate to Uranium Ratio

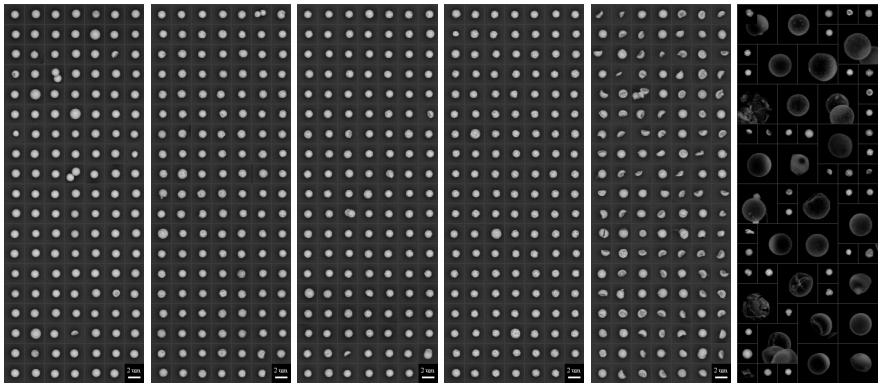

(a) $R = 1.3$ **(b)** $R = 2.0$ **(c)** $R = 5$ **(d)** $R = 10$ **(e)** $R = 20$ **(f)** $R = 85$

Figure 1: Collected SEM/BSED micrographs of particles produced from uranyl nitrate solutions with varying $n(\mathrm{NO_3})/n(\mathrm{U})$ ratios, treated at 500 °C.

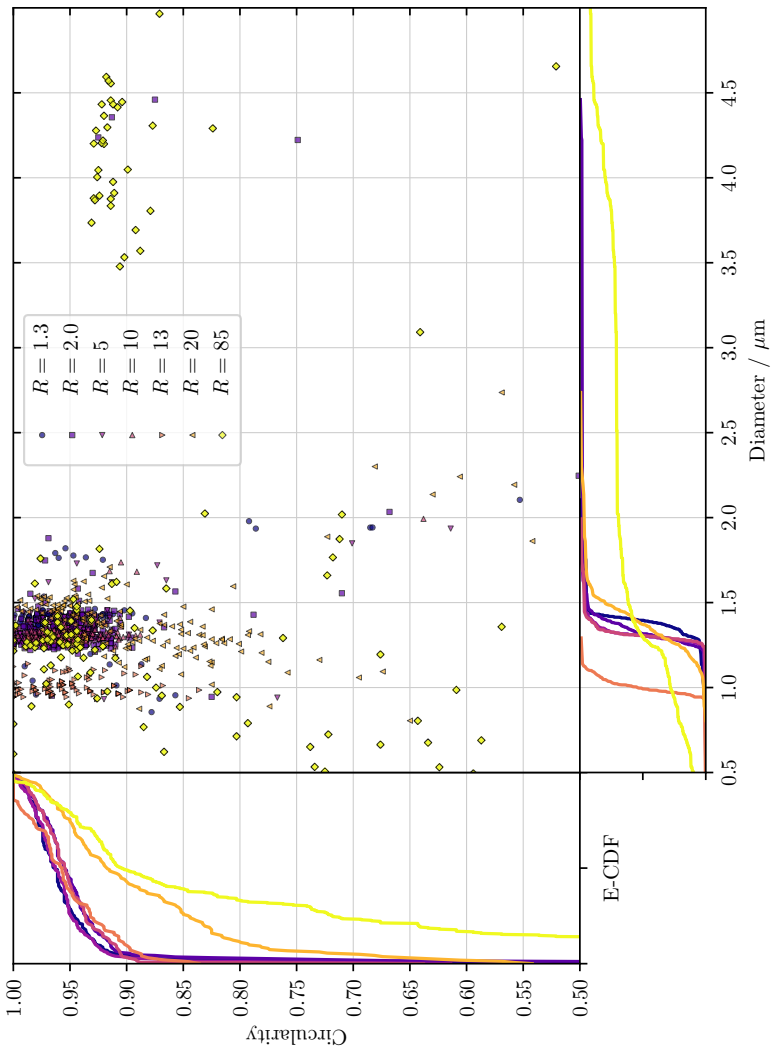

Figure 2: Empirical cumulative distribution function of the particle sphericity (4π[area]/[perimeter]^2) and particle diameter of particles produced from uranyl nitrate solutions with different NO_3/U ratios (R). The particles produced from solutions with $R = 13$ and $R = 85$ were produced during different production runs and a different uranium concentrations, due to which a direct comparison of the particle diameter is not possible.

μ-XRD Patterns

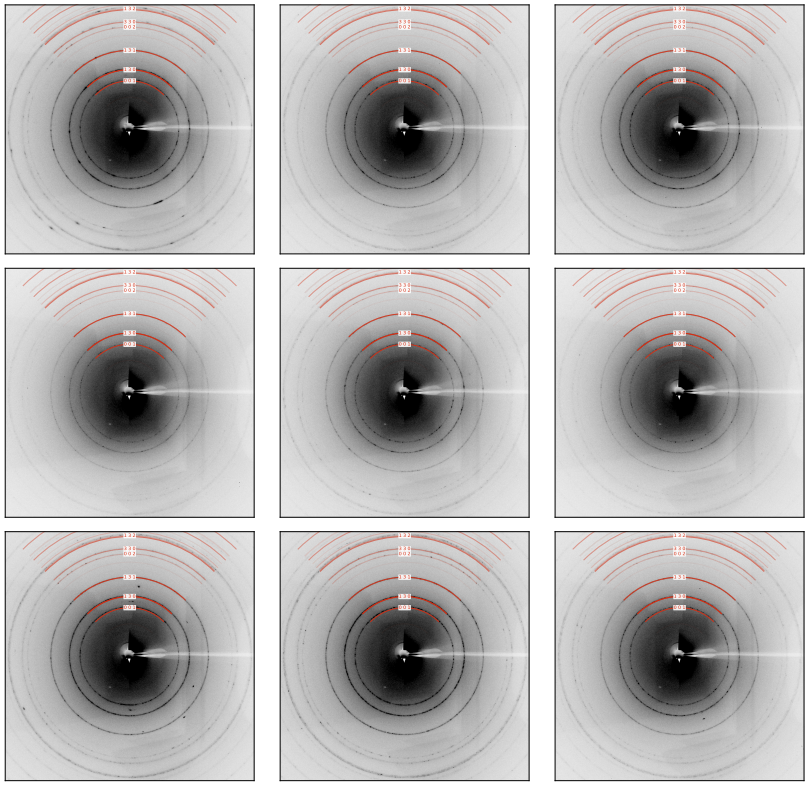

Figure 3: μ-XRD patterns of 9 measurements of particles produced using a uranyl nitrate feed solution and a thermal treatment of 400 °C. The red lines show the expected diffraction bands of orthorhombic U_3O_8.

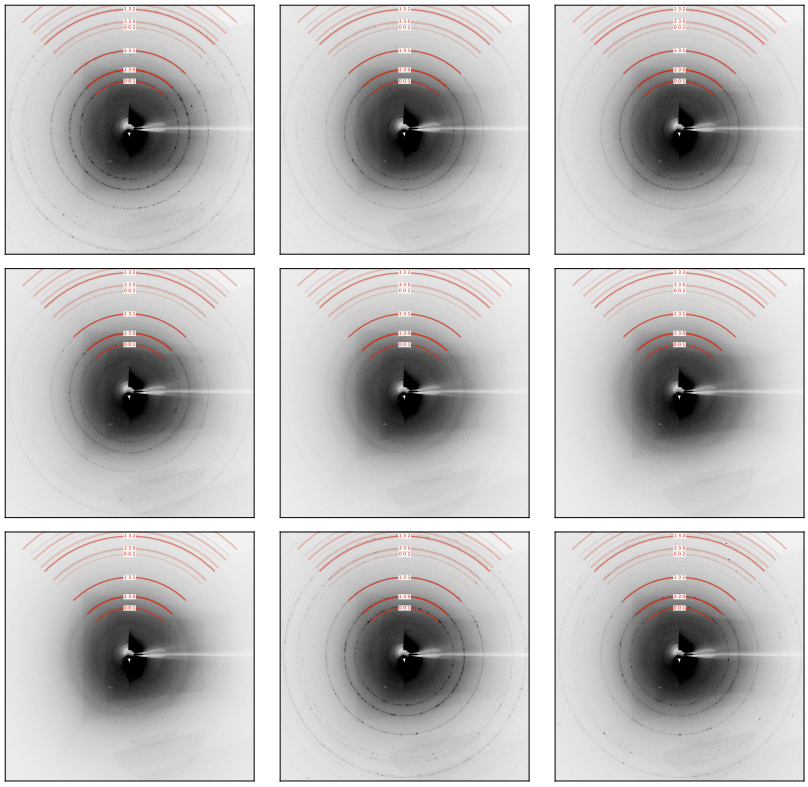

Figure 4: μ-XRD patterns of 9 measurements of particles produced using a uranyl nitrate feed solution and a thermal treatment of 500 °C. The red lines show the expected diffraction bands of orthorhombic U_3O_8.

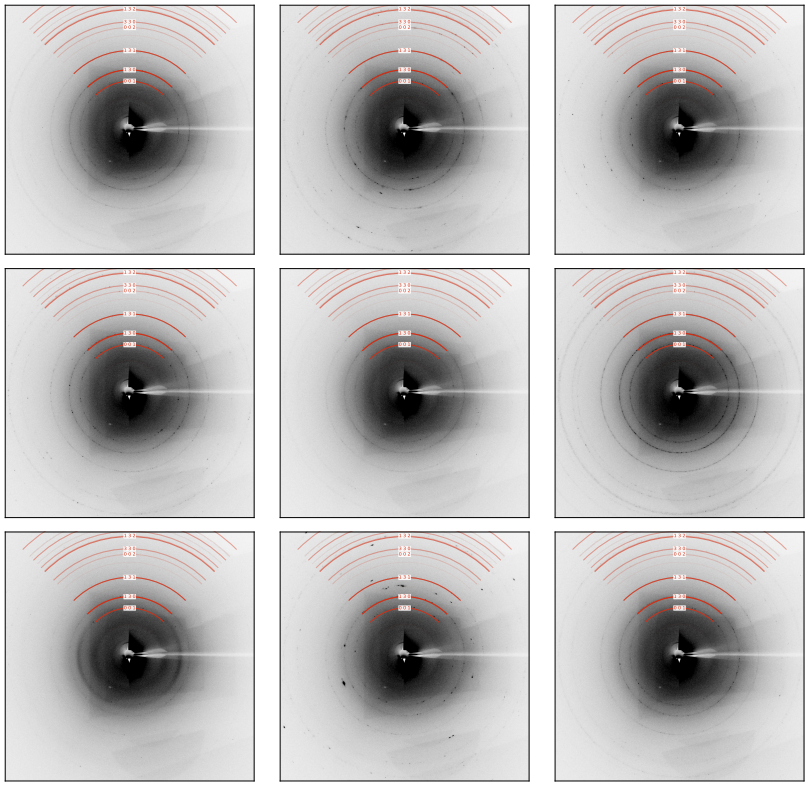

Figure 5: μ-XRD patterns of 9 measurements of particles produced using a uranyl nitrate feed solution and a thermal treatment of 600 °C. The red lines show the expected diffraction bands of orthorhombic U_3O_8.

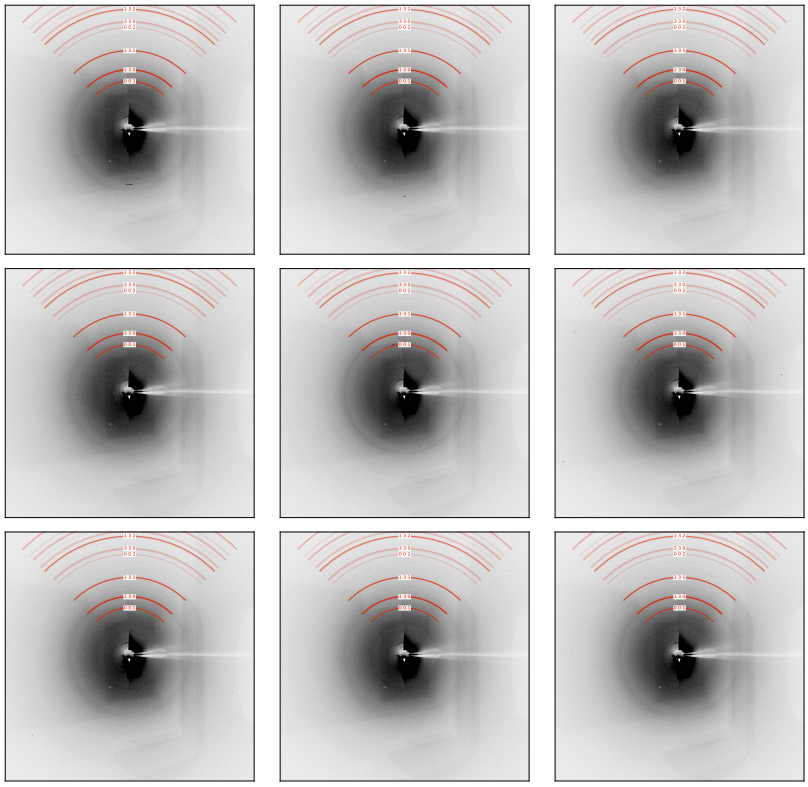

Figure 6: μ-XRD patterns of 9 measurements of particles produced using a uranyl acetate feed solution and a thermal treatment of 400 °C. The red lines show the expected diffraction bands of orthorhombic U_3O_8.

μ-XANES Spectra

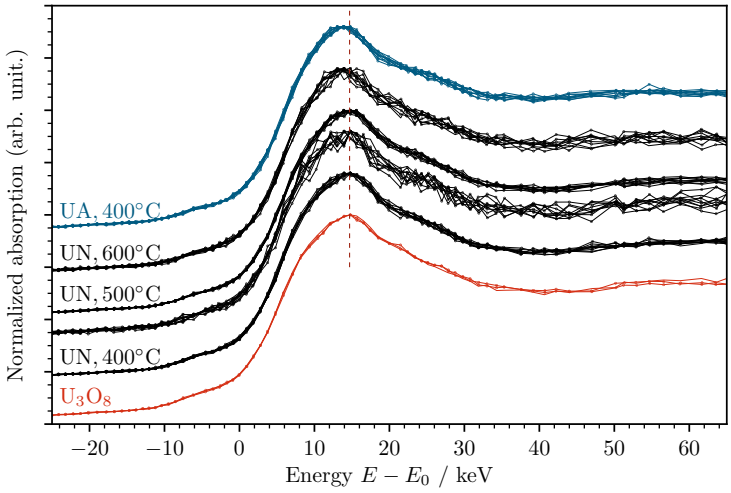

Figure 7: μ-XANES spectra of particles produced using a uranyl nitrate (UN) and uranyl acetate (UA) feed solutions and varying thermal treatment temperatures.

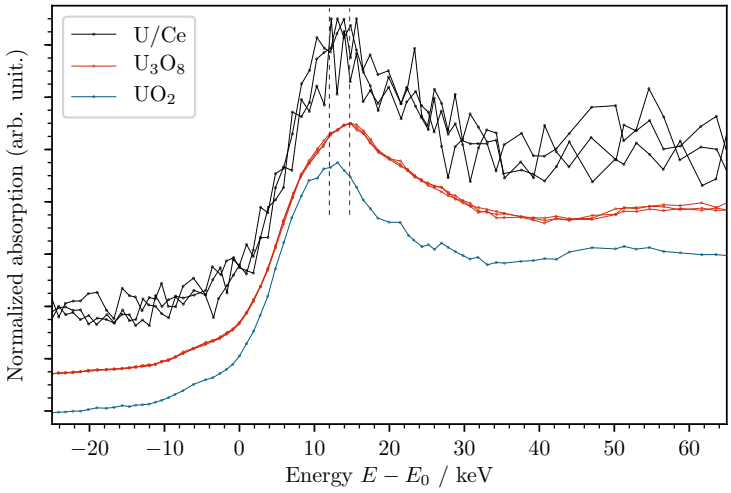

Figure 8: μ-XANES spectra of particles containing both uranium and cerium (ca. 0.50 g g^{-1} Ce) produced from nitrate solutions and a thermal treatment of 500 °C.

μ-Raman Spectra

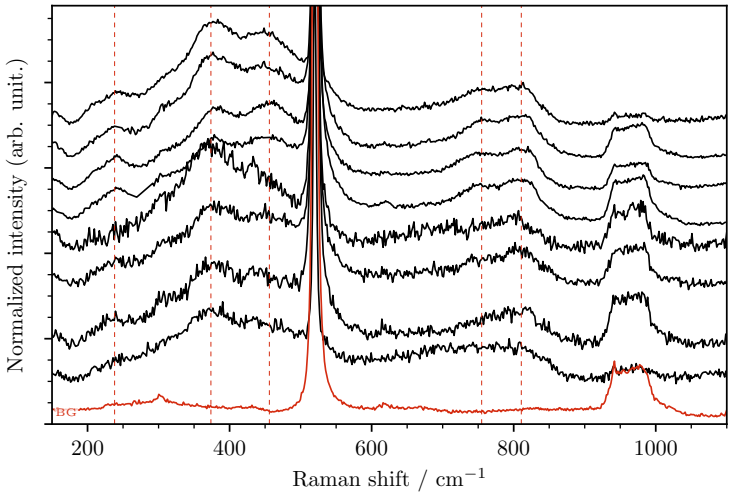

Figure 9: μ-Raman spectra of 8 particles produced using a uranyl nitrate feed solution and a thermal treatment of 500 °C.

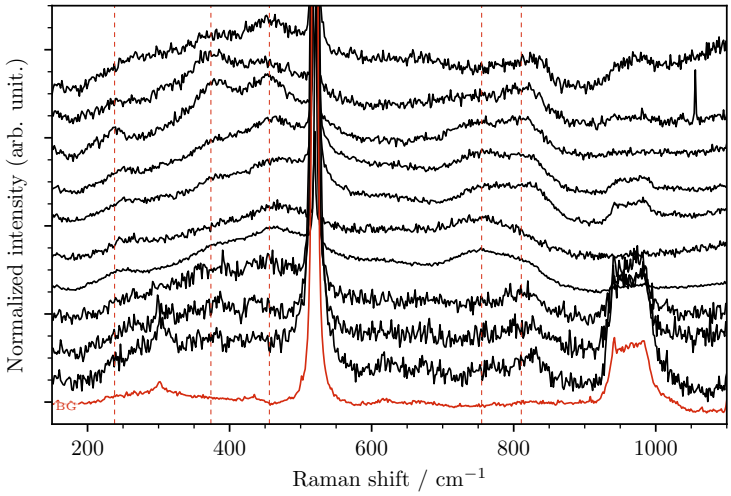

Figure 10: μ-Raman spectra of 10 particles produced using a uranyl acetate feed solution and a thermal treatment of 500 °C.

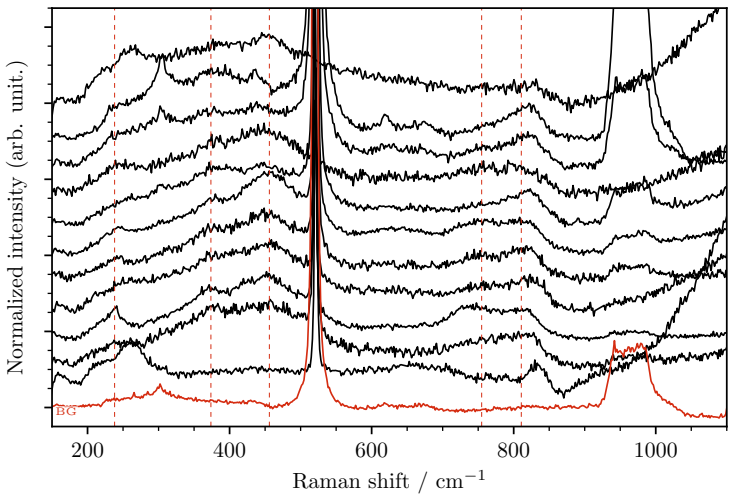

Figure 11: μ-Raman spectra of 11 particles produced using a uranyl chloride feed solution and a thermal treatment of 500 °C.

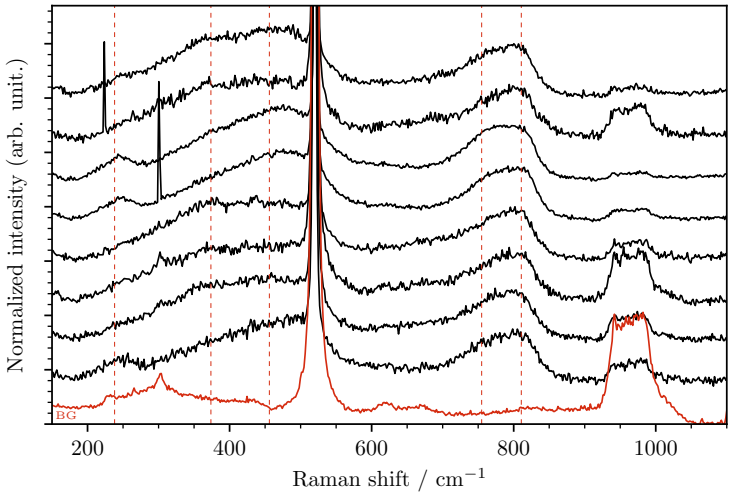

Figure 12: μ-Raman spectra of 8 particles containing both uranium and cerium with a cerium fraction of about 0.10 g g^{-1}.

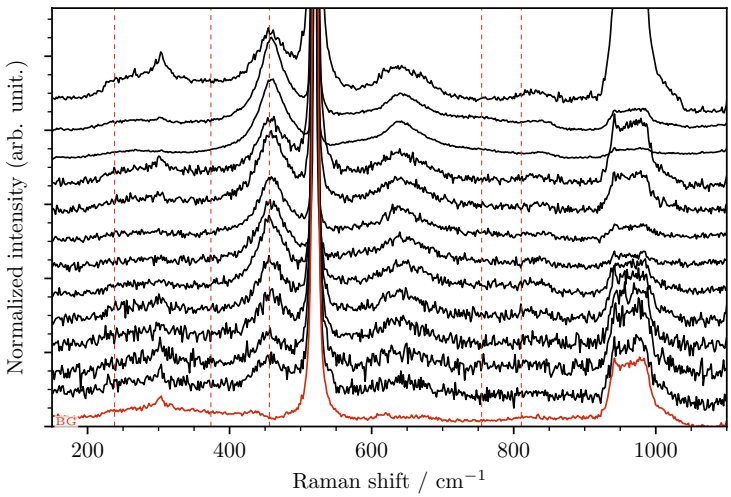

Figure 13: μ-Raman spectra of 12 particles containing both uranium and cerium with a cerium fraction of about 0.50 g g^{-1}.

Band / Volume 411
Charakterisierung und Optimierung der Grenzfläche Elektrolyt/Kathode in metallgestützten Festelektrolyt-Brennstoffzellen
D. Udomsilp (2018), XI, 176 pp
ISBN: 978-3-95806-304-4

Band / Volume 412
Formation of Secondary Organic Aerosol from Photo-Oxidation of Benzene: a Chamber Study
S. H. Schmitt (2018), III, 250 pp
ISBN: 978-3-95806-305-1

Band / Volume 413
Mechanismen der chrombasierten Degradation von metallgestützten Festoxid-Brennstoffzellen
A. Beez (2018), VIII, 144 pp
ISBN: 978-3-95806-306-8

Band / Volume 414
Entwicklung eines Werkzeugs zur Modellierung der Nettoerosion im Hauptraum der Brennkammer eines Tokamaks und Studium der Plasma-Wand-Wechselwirkung an DEMO1
M. Beckers (2018), XIX, 150 pp
ISBN: 978-3-95806-307-5

Band / Volume 415
Fehlstellendotierung von Eisenoxid- und Bismutsulfid-Nanopartikeln
J. P. Mock (2018), v, 187 pp
ISBN: 978-3-95806-309-9

Band / Volume 416
Nanocrystalline Silicon Oxide in Silicon Heterojunction Solar Cells
A. Richter (2018), 166 pp
ISBN: 978-3-95806-310-5

Band / Volume 417
Gas-to-Particle Partitioning of Major Oxidation Products from Monoterpenes and Real Plant Emissions
G. Gkatzelis (2018), xii, 128 pp
ISBN: 978-3-95806-314-3

Band / Volume 418
The Dynamics of Electrons in Linear Plasma Devices and its Impact on Plasma Surface Interaction
M. Hubeny (2018), 141 pp
ISBN: 978-3-95806-316-7

Band / Volume 419
Tomographic reconstruction of gravity wave parameters from satellite-borne airglow observations
R. Song (2018), 136 pp
ISBN: 978-3-95806-317-4

Band / Volume 420
Reduktion von Edelmetallen in der Wasserstoffelektrode bei der Polymerelektrolyt-Wasserelektrolyse
P. Paciok (2018), VII, 187 pp
ISBN: 978-3-95806-320-4

Band / Volume 421
Mechanismen des Hochtemperaturrisswachstums in einem ferritischen Stahl an Luft und in Wasserdampf
T. Fischer (2018), VIII, 216 pp
ISBN: 978-3-95806-326-6

Band / Volume 422
Selbstheilende plasmagespritzte $Mn_{1,0}Co_{1,9}Fe_{0,1}O_4$-Schutzschichten in Festoxidbrennstoffzellen
N. Grünwald (2018), viii, 137 pp
ISBN: 978-3-95806-327-3

Band / Volume 423
Sonochemical Synthesis of Silicon Hydride Polymers and Silicon Nanoparticles from Liquid Silanes
A. P. Cádiz Bedini (2018), viii, 129, XVIII pp
ISBN: 978-3-95806-329-7

Band / Volume 424
Synthesis and Stability Assessment of Uranium Microparticles: Providing Reference Materials for Nuclear Verification Purposes
R. Middendorp (2018), X, 145 pp
ISBN: 978-3-95806-330-3

Energie & Umwelt / Energy & Environment
Band / Volume 424
ISBN 978-3-95806-330-3

Mitglied der Helmholtz-Gemeinschaft

JÜLICH
Forschungszentrum